

1-1-2009

Finite element analysis of middle cervical spine

Noushin Bahramshahi
Ryerson University

Follow this and additional works at: <http://digitalcommons.ryerson.ca/dissertations>

 Part of the [Aerospace Engineering Commons](#)

Recommended Citation

Bahramshahi, Noushin, "Finite element analysis of middle cervical spine" (2009). *Theses and dissertations*. Paper 966.

This Thesis is brought to you for free and open access by Digital Commons @ Ryerson. It has been accepted for inclusion in Theses and dissertations by an authorized administrator of Digital Commons @ Ryerson. For more information, please contact bcameron@ryerson.ca.

FINITE ELEMENT ANALYSIS OF MIDDLE CERVICAL SPINE

By

Noushin Bahramshahi

B.Eng., Ryerson University, Toronto, 2007

A thesis

Presented to Ryerson University

in partial fulfillment of the
requirements for the degree of

Master Applied Science

in the Program of

Aerospace Engineering

Toronto, Ontario, Canada, 2009

© Noushin Bahramshahi 2009

Author's Declaration

I hereby declare that I am the sole author of this thesis or dissertation.

I authorize Ryerson University to lend this thesis or dissertation to other institutions or individuals for the purpose of scholarly research.

Abstract

FINITE ELEMENT ANALYSIS OF MIDDLE CERVICAL SPINE

Master of Applied Science 2009

Noushin Bahramshahi

Aerospace Engineering

School of Graduate Studies, Ryerson University

The spinal cord may be injured through various spinal column injury patterns. However, the relationship between column injury pattern and cord damage is not well understood. This investigation was conducted to develop a detailed, asymmetric three-dimensional finite element model of the C3-C5 cervical spine. The model was validated by comparing the simulation results obtained in this study with experimental published data.

Upon validation of the model, the spinal cord was included into the model the simulation were performed. The disc bulge in the model with spinal cord were measured and compared with the results of the model without spinal cord. The results showed that inclusion of the spinal cord reduced the amount of lateral disc bulged. The results of the analysis of the model with spinal cord showed that in compression, the anterior surface of spinal cord sees more displacement, stress and strain than posterior surface and vice verse for flexion/extension.

Acknowledgements

I would like to give my special thanks and extend my gratitude to Dr. Kamran Behdinan for his support and guidance. I am greatly indebted to Dr. Behdinan for allowing me to work on such incredible, interesting and at times very challenging project.

In addition, I like to thank Dr. Hamid Ghaemi for his support, help and insight. Without his support, this would not have been achieved.

Last but not least, I am extremely grateful to my father, Mr. Khodadad Bahramshahi for his support and encouragements at times that I had no strength left to go on. My father was a paragon of honesty in his life, and I will try to follow his footsteps to the best of my ability. I would like to dedicate this work to my mother's patience and in memory of my father. My success in achieving my goals is a direct result of your confidence in me. Thank you.

Table of Contents

Author's Declaration.....	i
Abstract.....	ii
Acknowledgements.....	iv
Chapter 1-INTRODUCTION	1
1.1 Motivation for Research	1
1.2 Research Objectivities	3
1.3 Organization of the Thesis by Chapter	4
Chapter 2-SPINAL ANATOMY	6
2.1 Introduction.....	6
2.2 Spinal Terms	6
2.3 Vertebral Column.....	9
2.3.1 Cervical Vertebrae Structure.....	12
2.3.2 Vertebrae Joints	16
2.4 Intervertebral Disc Structure.....	18
2.4.1 Biomechanics of the Intervertebral disc	21
2.5 Ligaments.....	22
2.6 Spinal Cord	28
Chapter 3-LITRETURE REVIEW	31
3.1 Introduction.....	31
3.2 Finite Element Models.....	31
3.2.1 Spine Segment FE Models.....	32
3.2.2 Full cervical spine Models.....	42
3.3 Experimental Studies	47

Chapter 4-MODEL DEVELOPMENT.....	52
4.1 Model Construction	52
4.1.1 Vertebrae Construction.....	53
4.1.2 Facet Joint Construction	59
4.2 Intervertebral Disc Construction.....	61
4.3 Ligament Construction.....	62
4.4 Spinal Cord Construction.....	63
4.5 Full Middle Cervical Model.....	64
Chapter 5-MATERIAL MODELING OF SOFT TISSUES.....	67
5.1 Introduction.....	67
5.2 Biphasic Theory	68
5.3 Poroelastic Theory	69
5.4 Material Property	71
Chapter 6-FE SIMULATION AND RESULTS	75
6.1 Introduction.....	75
6.2 FE Simulation Method.....	75
6.3 Simulation Results	80
Chapter 7-CONCLUSIONS.....	96
AppendixA.....	104
A.1 Biphasic Background Mathematical Formulation	104
A.2 Proelastic Background Mathematical formulation	110
AppendixB	112
References.....	125
Glossary of Acronyms	133

List of Tables

Table 2-1: Vertebral Dimensions and Bone Thickness	15
Table 2-2: Superior and inferior articular facet linear dimensions.....	18
Table 2-3: Composition of AF, NP and CEP.....	20
Table 2-4: Measured intervertebral disc heights.....	21
Table 2-5: Area (n=4) and length (n=4) of cervical spine ligaments.....	27
Table 2-6 : Diameters and area of the cervical cord.....	30
Table 4-1 : Measured dimensions of vertebral body and endplate.....	54
Table 4-2 : Measured heights of intervertebral discs.....	61
Table 4-3: Element breakdown summary of vertebrae.....	66
Table 4-4: Element breakdown summary of intervertebral disc.....	66
Table 4-5: Element breakdown summary of ligaments.....	66
Table 4-6: Element breakdown summary of spinal cord.....	66
Table 5-1: Material properties of Vertebrae and Intervertebral discs components.....	73
Table 5-2: Material properties of the ligaments.....	74
Table 5-3: Material properties of spinal cord.....	74
Table 6-1: List of defined contacts between the bodies.....	79
Table 6-2 : Median, Maximum and minimum values in millimeters of disc bulging data evaluated for anterior and posterior locations.....	89
Table 6-3 : Median, Maximum and minimum values in millimeters of disc bulging data evaluated for anterior and posterior locations.....	90
Table 6-4 : Maximum equivalent von mises stress.....	92
Table 6-5 : Anterior displacement, stress and % of strain in dural sheath, CSF and cord during compression, flexion and extension.....	93

Table 6-6: Posterior displacement, stress and % of strain in dural sheath, CSF and cord during compression, flexion and extension.	93
Table 7-1: Maximum C4-C5 disc stress, disc bulge and location.	102

List of Figures

Figure 2-1: Anatomical Planes and Directions (Adapted from the US National Cancer Institute).	8
Figure 2-2: Cervical Spine Movements (Adopted from Drake <i>et al.</i> , 2005).	9
Figure 2-3: The human spine with the cervical spine extending from C1 to C7, the thoracic spine from T1 to T12, the lumbar spine from L1 to L5, the sacrum and coccyx (Adapted from www.backpain-guide.com).	11
Figure 2-4: Regional vertebrae (Adopted from Drake <i>et al.</i> , 2005).	12
Figure 2-5: Sagittal section of a vertebra (Adapted from www.apparelyzed.com).	14
Figure 2-6: Regional vertebrae, A. Atlas (C1), B. Axis (C2) (Adopted from Drake <i>et al.</i> , 2005).	16
Figure 2-7: Vertebrae Joints (Adopted from Drake <i>et al.</i> , 2005).	17
Figure 2-8: Intervertebral disc (Adopted from White <i>et al.</i> , 1990 & www.chirogeek.com)	19
Figure 2-9: Motion segment loading scenarios. A. An uncompressed motion segment. B. Under axial compression. C. Under bending loads (Adopted from Guerin, 2005).	22
Figure 2-10: Liaments (Adopted form www. Spineuniverse.com).	23
Figure 2-11: LF & SSL and ISL ligaments (Adopted from Drake <i>et al.</i> , 2005).	26
Figure 2-12: The length defination used for the various ligaments (Adopted from Yoganandan <i>et al.</i> , 2000).	27
Figure 2-13 : Schematic diagram showing variations in spinal cord segments at different levels (Adopted from Afifi <i>et al.</i> , 2005).	28
Figure 2-14 : Schematic of spinal cord showing the meningeal coats (Adopted from www.academic.kellogg.cc.mi.us).	29
Figure 2-15:Measurements of the spinal cord. Anteroposterior diameter (A). Transverse diameter (B). Spinal cord area (C) (Adopted from Ishikawa <i>et al.</i> , 2003).	30
Figure 3-1: Finite element model of a C4 vertebra (Adopted from Bozic <i>et al.</i> , 1994). ..	33

Figure 3-2: Finite element model of IVD (Adopted from Belytschko <i>et al.</i> , 1974).....	34
Figure 3-3: The 3D nonlinear model of L2-L3 (Adopted from Shirazi-Adl <i>et al.</i> , 1984).	35
Figure 3-4: The 3D nonlinear model of L2-L3 (Adopted from Shirazi-Adl <i>et al.</i> , 1996).	36
Figure 3-5: 3-D finite element model of C4-C5-C6. A. Yoganandan <i>et al.</i> , 1996b and B. Kumaresan <i>et al.</i> , 1999.	38
Figure 3-6: 3D finite element of C5-C6 (Adopted from Clausen <i>et al.</i> , 1997).....	39
Figure 3-7: 3D finite element model of cervical spine, A. C3-C7 model of	40
Figure 3-8: C5-C6 model of cervical spine with spinal cord (Adopted from Scifert <i>et al.</i> , 2002).	41
Figure 3-9: A. Anterolateral view of the C4-C6 vertebrae, spinal cord and connecting ligaments. B. Anterolateral view of the spinal cord and dura matter (Adopted from Greaves <i>et al.</i> , 2008).	42
Figure 3-10: 3D full finite element model of cervical spine, A. C1-T1 model of Kleinberger, 1993 and B. C2-C7 model of Ng, Teo and Zhang, 2005.....	45
Figure 3-11: 3D finite element model of head-T1 (Adopted from Jost and Nurick, 2000).	45
Figure 3-12: 3D finite element of C0-C7 (Adopted from Palomar <i>et al.</i> , 2008).....	46
Figure 4-1 : A. Image conversion procedure for FE mesh and B. generated CAD data of C3-C6 vertebrae.	53
Figure 4-2 : A. Superior view of the C3 vertebra and B. Cross section view of the C3 vertebra showing the superior and inferior endplates.	56
Figure 4-3 : The construction of a typical deformable vertebra.	58
Figure 4-4 : A. The C3-C5 cortical bone and B. The C3-C5 cancellous bone.	59
Figure 4-5 : Construction of a Typical Facet Joint	60
Figure 4-6 : Superior view of the C3-C4 Intervertebral disc	62
Figure 4-7 : Ligaments in middle cervical spine.	63
Figure 4-8: A. Side view of C3-C5 vertebrae with the spinal cord. B. Superior view of the C2-C5 spinal cord.	64

Figure 4-9 : C3-C5 Finite element model.....	65
Figure 6-1: The position of ten non-collinear points on the C4 vertebra.....	76
Figure 6-2 : Contact body definition of middle cervical spine.	80
Figure 6-3 : Comparison of the force-displacement response between present and the Shea <i>et al.</i> (1991) results.....	82
Figure 6-4 : Y-Displacement counter plots of the C4 vertebra as a result of 600 N applied compressive load.....	83
Figure 6-5 : Comparison of the lateral C4-C5 anterior and posterior disc bulge between the present and Ng <i>et al.</i> (2001) results.	83
Figure 6-6 : Z-Displacement (lateral bulging) counter plots of C4-C5 intervertebral disc.	84
Figure 6-7 : Comparison of the C3-C4 moment-rotation relationship between current results and Wheeldon <i>et al.</i> (2006) results.....	85
Figure 6-8 : Comparison of the C4-C5 moment-rotation relationship between current results and Wheeldon <i>et al.</i> (2006) results.....	86
Figure 6-9 : Comparison of the C4-C5 moment-rotation relationship between current results and Wheeldon <i>et al.</i> (2008) results.....	86
Figure 6-10 : Predicted variation of the lateral disc bulge with axial compressive load for the finite element model with spinal cord.....	87
Figure 6-11 : Z-Displacement (lateral bulging) counter plots of C4-C5 intervertebral disc.	88
Figure 6-12 : Comparison of the C4-C5 disc bulge between model with and without spinal cord.....	89
Figure 6-13: Comparison of the C4-C5 disc bulge between model with and without spinal cord.	91
Figure 6-14: Dural sheath z displacement under axial compressive load.....	94
Figure 6-15 : Dural Sheath axial strain under axial compressive load.	94
Figure 6-16: Dural sheath equivalent von mises stress under axial compressive load. ..	95

Figure A-1: The kinematics relationship between the solid and fluid reference configurations and the current configuration (Adopted from Suh et al., 1991).....	106
Figure B-5: C4-C5 disc stress under compression with spinal cord.....	112
Figure B-6: C4 cortical stress under compression with spinal cord.	112
Figure B-7: C4 cancellous bone stress under compression with spinal cord.....	113
Figure B-12: C4-C5 disc z displacement under extension with spinal cord.....	113
Figure B-13: C4-C5 disc stress under extension with spinal cord.....	114
Figure B-14: C4 cortical bone stress under extension with spinal cord.	114
Figure B-15: C4 cancellous bone stress under extension with spinal cord.....	115
Figure B-20: C4-C5 disc z displacement under flexion with spinal cord.....	115
Figure B-21: C4-C5 disc stress under flexion with spinal cord.....	116
Figure B-22: C4 cortical bone stress under flexion with spinal cord.	116
Figure B-23: C4 Cancellous bone stress under flexion with spinal cord.....	117
Figure B-28: C4-C5 disc z displacement under right lateral with spinal cord.....	117
Figure B-29: C4-C5 disc stress under right lateral with spinal cord.....	118
Figure B-30: C4 cortical bone stress under right lateral with spinal cord.	118
Figure B-31: C4 cancellous bone stress under right lateral with spinal cord.	119
Figure B-36: C4-C5 disc z displacement under left lateral with spinal cord.....	119
Figure B-37: C4-C5 disc stress under left lateral with spinal cord.....	120
Figure B-38: C4 cortical bone stress under left lateral with spinal cord.	120
Figure B-39: C4 cancellous bone stress under left lateral with spinal cord.....	121
Figure B-40: CSF z displacement under compression.....	122
Figure B-41: CSF stress under compression.....	122
Figure B-42: CSF axial strain under compression.	123

Figure B-43: Cord z displacement under compression..... 123

Figure B-44: Cord stress under compression..... 124

Figure B-45: Cord axial strain under compression..... 124

Chapter 1

Introduction

1.1 Motivation for Research

The cervical spine is a complex mechanism from a mechanical and structural point of view. The vertebral column has two major functions, to stabilize the head and to protect the spinal cord. Therefore, cervical spinal injuries are a potential threat to the spinal cord and must be treated with respect and caution. The effects of spinal cord injuries are serious, ranging from death to quadriplegia, loss of sensory functions, and a range of deficits. The incidence of spinal cord injury, as recorded by the highest level of injury, occurs in the upper cervical (C1-C2) region in 11%, the middle and lower cervical (C3-C7) in 51%, Meyer *et al.* (1991).

Clinical evidence suggests that a relationship exists between column injury patterns and resulting damage to the cord, presenting as neurological deficits, Dall *et al.* (1972) and Greaves *et al.* (2008). This relationship may result from mechanical characteristics of column injury patterns causing certain spatial distributions and degrees of damage to spinal cord tissue. Despite these findings, mechanism-specific characteristics of spinal cord damage are not well understood Greaves *et al.* (2008). An understanding of physiologic cervical spinal cord deformation is important for defining an injury threshold of the cervical spinal cord. Studies have shown that damage to the spinal cord can occur regardless of significant damage to surrounding structures. There is no data correlating

the behavior of the human spinal cord during impact delivered to the head with the clinical symptoms *in vivo* studies and such investigations are not practical. Most experimental studies have been performed with many strict restrictions and thus the analytical methods can help to overcome these restraints.

Finite element analysis is the most popular analytical method for quantifying internal parameter values (i.e., stresses and strains) in the spinal column. Through the years, FE analysis has been used in many studies regarding clinical application of the cervical spine. The FE analysis helped in defining the roles of various anatomic elements (e.g., facets and discs) in supporting, physiologic and traumatic load applied to the cervical spine, Yoganadan *et al.* (1996a), Ng *et al.* (2001). One of the earliest works of finite element analysis in human spine was reported by Liu and Ray (1973). Since that time, the finite element method has played an increasingly important role in improving our understanding of the fundamental biomechanics of the cervical spine. However, there were few finite elements models that included the spinal cord model into their cervical spine model, Scifert *et al.* (2002) and Greaves *et al.* (2008). To understand the mechanics of spinal cord injury, one needs to quantify stresses and strains within the spinal cord in response to external loads applied to the bony spine which experimental studies cannot address this issue. Therefore, this study has modeled an anatomically accurate model of spinal cord and has included it into the C3-C5 motion segment. Furthermore, the displacements, stresses and strains of the spinal cord elements were computed.

Back pain has been described as one of the most common and significant musculoskeletal problems leading to substantial amounts of morbidity, disability, and economic loss. Disorders of the intervertebral disc have been some of the most widely supported and

intensely investigated mechanisms for back pain. Many patients with back pain present radiographic evidence of disc degeneration in the cervical spine, e.g., loss of disc height, loss of lordosis, and anterior, posterior or lateral subluxation. Furthermore, degenerative changes in cervical intervertebral discs, such as tears and fissures of the annulus fibrosus have been implicated as potential factors in many painful spinal conditions. Therefore, an understanding of the mechanical response of the intervertebral disc under various loading is necessary. The mechanical behavior of the motion segment has been the subject of frequent study, an overall understanding of the load-deformation characteristics of the intervertebral disc *in situ* does not bring with it the knowledge of the internal intervertebral disc mechanics. Therefore, studying the mechanical behaviors of the intervertebral disc will yield important information about progressive disc degeneration and pathology for the entire cervical spine.

1.2 Research Objectivities

In performing the finite element analysis of the cervical spine, it is necessary to model the actual geometry accurately enough to avoid the inaccuracy that may result due to simplified geometry, Ha (2006). However, among various cervical finite element models in the literature, the geometry of the vertebrae were modeled very simplistic or they were assumed to be symmetric to site a few, Hosey *et al.* (1982), Ng *et al.* (2001), Clausen *et al.* (1997), Maurel *et al.* (1997), Kumaresan *et al.* (1999 and 2001). Therefore, the first objective is to construct an anatomically accurate asymmetric three-dimensional finite element model of the complete middle cervical spine of a 25-30 year-old healthy male.

Most of the previous models considered bone and intervertebral disc (soft tissues) as a single phase (solid) material model. Therefore, the second objective is to develop a finite element model of middle cervical spine based on a linear, isotropic, two-phase material (solid and fluid) model for the vertebrae and discs.

Given the numerous applications of the cervical spine model, it is imperative to ensure that a numerical model has been validated for its intended use. Hence, the third objective was to validate and compare the present C3-C5 finite element model with experimental data and existing finite element models from literature under various reported loading conditions. Furthermore, to study the biomechanical response of the model under compression, flexion, extension and lateral bending conditions, and to predict the lateral disc bulge and maximum stress of C4-C5 intervertebral disc, cortical bone and cancellous bone as determined by FE simulation.

Little is known about the relationship between vertebral motion and spinal cord distortion. Therefore, the final objective of this study is to develop anatomically accurate model of spinal cord and to study its behavior and effects on vertebrae and discs under various loading conditions.

1.3 Organization of the Thesis by Chapter

This thesis is presented in a format that is comparable to the approach taken in developing the cervical spine model.

Chapter 2 focuses on the anatomy and physiology of the various tissues of the cervical spine. This background research is an essential phase of the development process, as accurate anatomy is one of the main pillars required for producing a biofidelic model.

A review of the FE modeling and experimental studies performed on the human cervical spine are summarized in Chapter 3.

Chapter 4 outlines the process used in the development of the new cervical spine model. Modeling techniques used in constructing the numerical model are first discussed. Various measures of cervical spine model geometry are presented as a verification tool, comparing the model anatomy with that described in Chapter 3.

Another pillar required for accurate modeling of biological systems is found in the extensive background research presented in Chapter 5, which delves into the complex mechanical properties of tissue. This research provides the fundamental detail of the mechanical response of the tissue, and provides insight into the requirements for the material models.

A summary and analysis of the results of the single segment models are presented in Chapter 6. The results are compared to various sources of experimental data to validate the model. A more detailed presentation of the counter plots are found in Appendix A.

Finally, Chapter 7 provides the overall discussions and conclusions for the model.

Chapter 2

Spinal Anatomy-Overview

2.1 Introduction

Anatomy is a branch of natural science dealing with the structural organization of living things, which is sometimes called as functional anatomy. It is a general term that includes human anatomy, animal anatomy (zootomy) and plant anatomy (phytotomy). Human anatomy usually deals with the observation, experimentation and prediction of morphological structures that makeup the human body. The human body is the entire physical and mental structure of a human organism, and consists of a head, neck, torso, two arms and two legs. In this study, the main focus has been in the neck region; therefore, a basic understanding of the spine's anatomy and its functions is extremely important. This chapter provides a straightforward overview of the spine's remarkable and complex anatomy. It begins by providing a big picture of the functions of the spine, its regions, and major curves. This is followed by detailed information on specific anatomic elements such as vertebral structures, intervertebral discs, the spinal cord, joints and ligaments.

2.2 Spinal Terms

To help further understand and describe the anatomy, spine specialists often refer to sections of the body in terms of anatomical planes (flat surfaces). They use three basic reference planes that are imaginary lines, vertical or horizontal and drawn through an

upright body. These planes are the frontal (coronal) plane, the transverse (axial) plane, and the sagittal (median) plane as shown in **Figure 2-1**. The **frontal** plane is an X-Y plane, perpendicular to the ground, which divides the body into dorsal and ventral (back and front, or posterior and anterior) portion. On the other hand, the **transverse** plane is an X-Z plane, parallel to the ground, which separates the body into cranial and caudal (head and tail, or superior and inferior) portions. The **sagittal** plane is an Y-Z plane, perpendicular to the ground, which passes through the midline and divides the body into left and right halves of equal proportion.

In addition to the anatomical planes, medical professionals often use various anatomical terms to describe direction and location within the human body (**Figure 2-1**). In standard anatomical position, top and bottom, and back and front correspond to the head and feet, and tail and nose, respectively in humans. The head end is referred to the **superior end**, while the feet are referred to the **inferior end**. Also anatomically, the nose is referred as the **anterior end**, while the tail is referred as **posterior end**. Furthermore, **medial** indicates that a structure is nearer to the median plane (midpoint) of the body, while **lateral** indicates that a structure is farther away from the median plane. **Superficial**, **intermediate** and **deep** are used in dissection to describe the position of one structure with respect to another

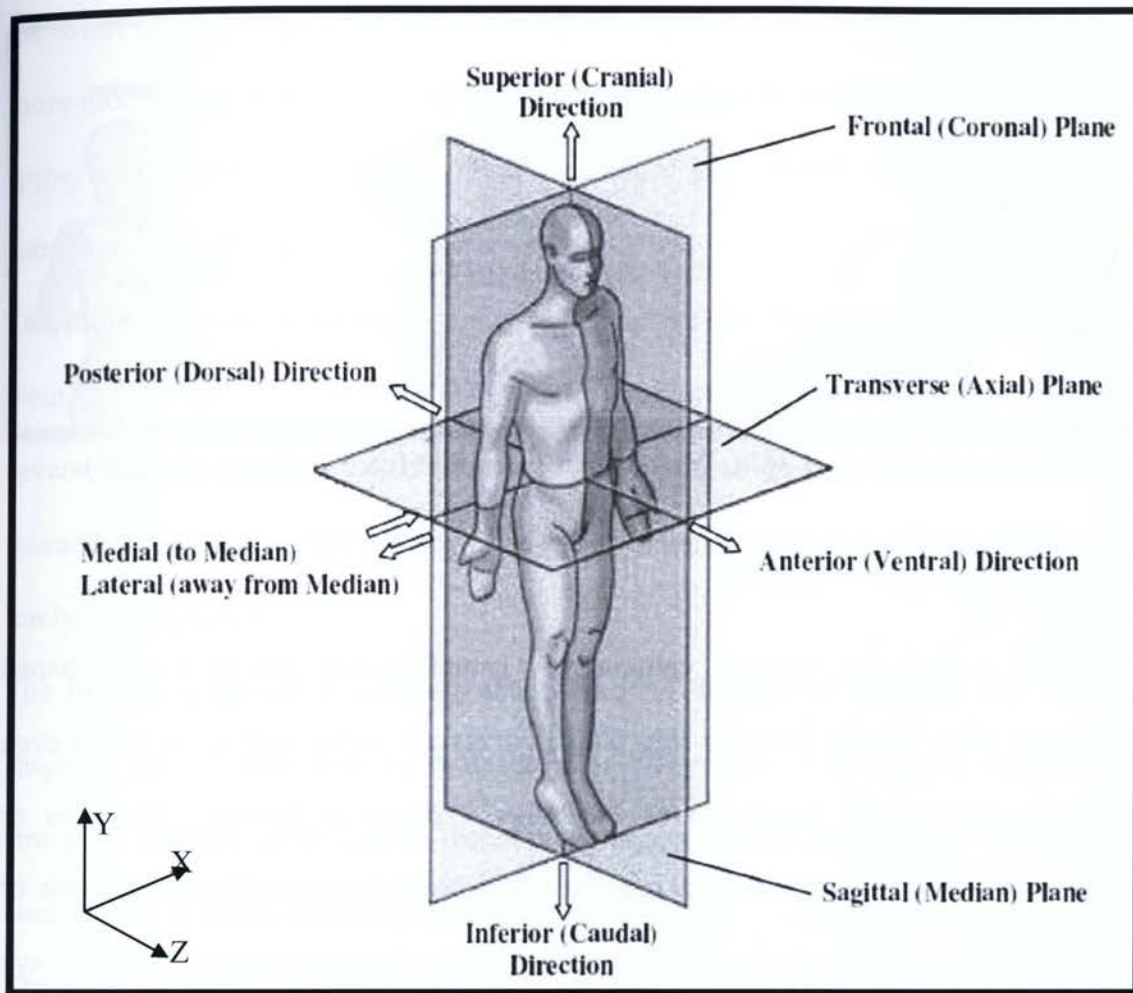


Figure 2-1: Anatomical Planes and Directions (Adapted from the US National Cancer Institute).

The anatomical terms for the movements of the cervical regions are flexion, extension, lateral flexion and rotation (**Figure 2-2**). **Flexion** (forward bending) is a bending movement in which the relative angle between two adjacent segments decreases. **Extension** (backward bending) is opposite of flexion. It is a straightening movement in which the relative angle between two adjacent segments increase. **Lateral flexion** (left and right) is a frontal-plane movement that rotates away from the midline. **Rotation** refers to the movement of one vertebra to another about its normal or abnormal coronal axis.

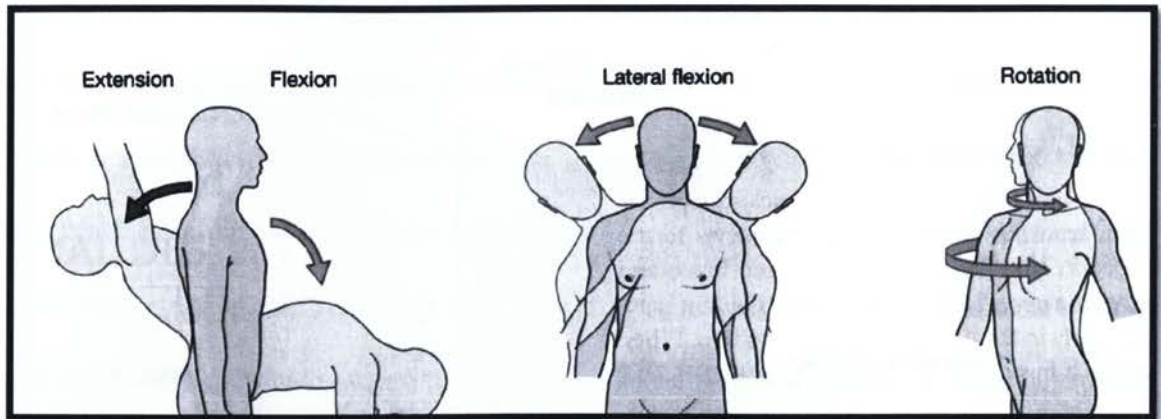


Figure 2-2: Cervical Spine Movements (Adopted from Drake *et al.*, 2005).

2.3 Vertebral Column

The spinal column (or vertebral column) has natural curves, giving it an s-shaped appearance when viewed from the side. These curves are normal and allow for an even distribution of weight. Spinal curves are either kyphotic or lordotic. **Kyphosis** or kyphotic curve is normally concave anteriorly and convex posteriorly and **lordosis** or lordotic curve is opposite of a kyphotic curve in the spine (convex anteriorly and concave posteriorly). In a normal spine there are four types of spinal curvatures important to balance, flexibility, and stress absorption and distribution.

The vertebral column extends from the skull to the pelvis and is made up of 33 individual bones termed vertebrae. 24 of these bones are known as vertebrae and can be categorized into 3 parts (cervical, thoracic, and lumbar) and the remaining bones are known as sacrum and coccyx. These regions can be seen in the diagram of the entire human spine (**Figure 2-3**).

The **cervical** spine comprises the first seven vertebrae and further divided into three parts; the upper cervical region (C1 and C2), the middle cervical region (C3 – C5) and

the lower cervical region (C6 - C7). The cervical spine supports the head, and it is much more mobile than other spinal regions. This study mainly focused on the middle cervical spine, which has a different anatomy than the rest of the vertebral column and is the most flexible part of cervical spine.

The **thoracic** spine comprises the middle 12 vertebrae and they gradually increase in size from T1 through T12. The large bump on the back of the lower part of the neck is the seventh cervical vertebra, called C7. It connects on top of T1. The lowest vertebra of the thoracic spine, T12, connects below the bottom of the rib cage to the first vertebra of the lumbar spine, called L1.

The **lumbar** spine has 5 vertebrae abbreviated L1 through L5 (largest). The size and shape of each lumbar vertebra is designed to carry most of the body's weight. Each structural element of a lumbar vertebra is bigger, wider and broader than similar components in the cervical and thoracic regions.

The **sacrum** is located behind the pelvis. Five bones, abbreviated S1 through S5, fused into a triangular shape, form the sacrum. The sacrum fits between the two hip bones connecting the spine to the pelvis. The last lumbar vertebra (L5) articulates (moves) with the sacrum. Immediately below the sacrum are five additional bones, fused together to form the **coccyx** (tailbone).

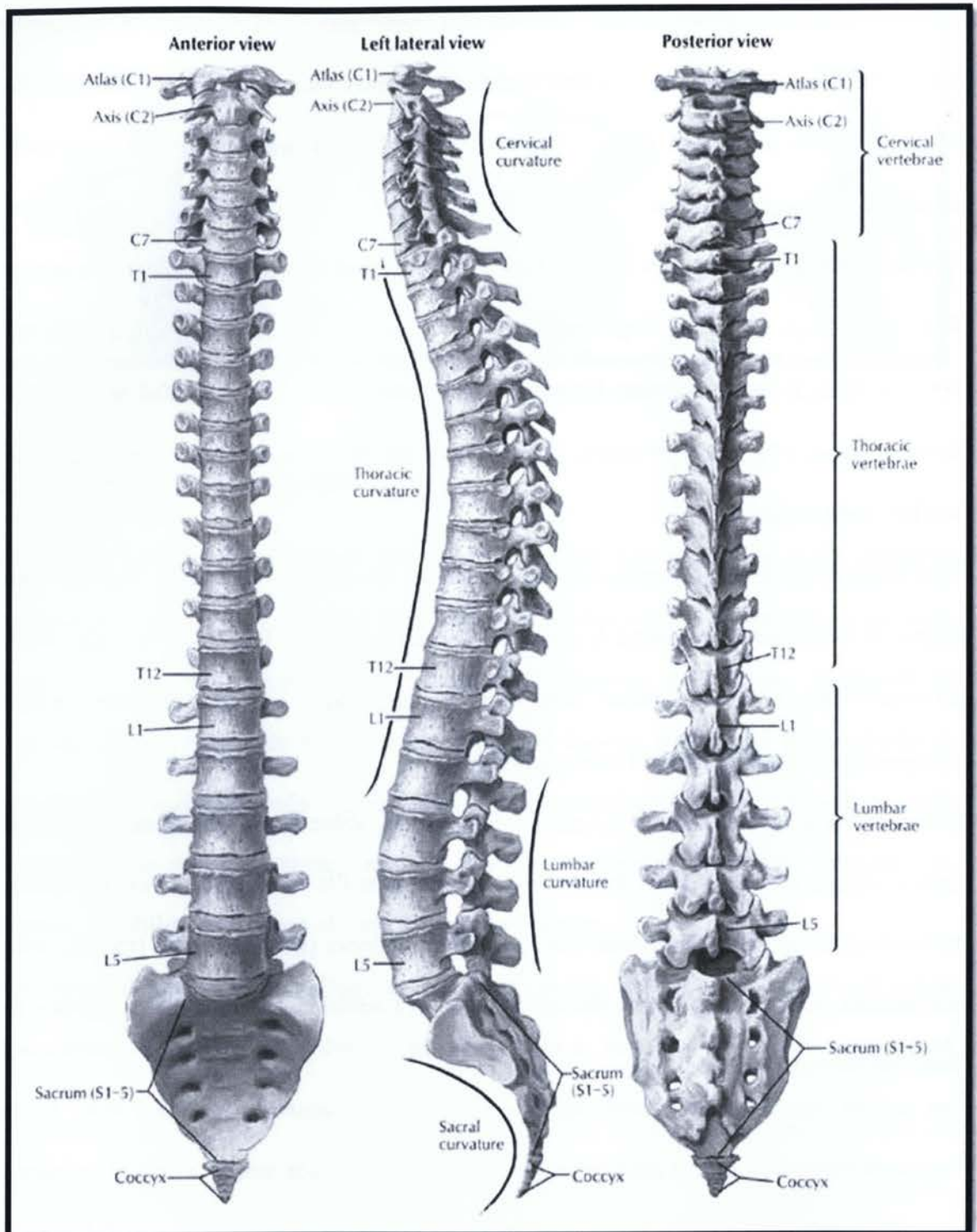


Figure 2-3: The human spine with the cervical spine extending from C1 to C7, the thoracic spine from T1 to T12, the lumbar spine from L1 to L5, the sacrum and coccyx (Adapted from www.backpain-guide.com).

2.3.1 Cervical Vertebrae Structure

A typical vertebra consists of two essential parts: an anterior (front) segment (vertebral body) and a posterior part (vertebral (neural) arch) which encloses the vertebral foramen (Figure 2-4).

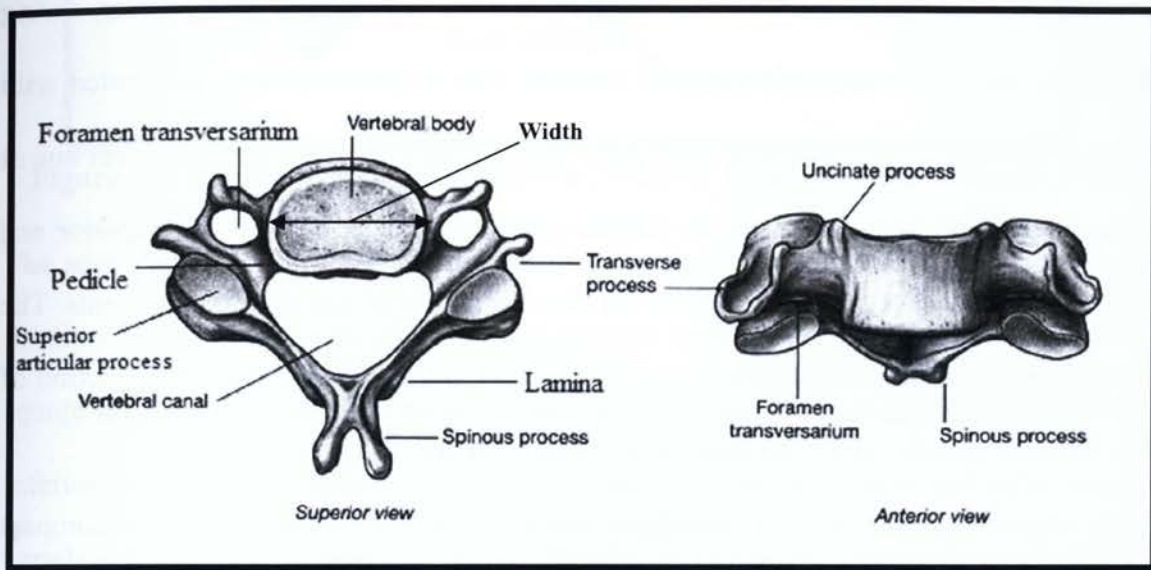


Figure 2-4: Regional vertebrae (Adopted from Drake *et al.*, 2005).

The **vertebral body** is anterior in position and is the major weight bearing component of the bone. It increases in size from cervical vertebra to lumbar vertebrae. Its upper and lower surfaces are flattened and rough, and give attachment to the intervertebral fibrocartilages, and each presents a rim around its circumference.

The **vertebral arch** consists of a pair of pedicles and a pair of laminae, and supports seven processes (four articular processes, two transverse processes and one spinous processes). The vertebral arch of the vertebrae is aligned to form the lateral and posterior walls of the vertebral canal, which extends from the first cervical vertebra to the last sacral vertebra. The **pedicles** are two short, thick processes, which project backward, one

on either side, from the upper part of the body, at the junction of its posterior and lateral surfaces. Each vertebra comprises two **laminae** which are thin plates of bone that extend from either side of the vertebral body and meet at the spinous process. Together, the laminae and the vertebral body surround the spinal cord and give rise to the vertebral foramen. The **articular processes** of a vertebra, two superior and two inferior, spring from the junctions of the pedicles and laminae. The articular surfaces are coated with hyaline cartilage. The **transverse processes** of a vertebra, two in number, project one at either side from the point where the lamina joins the pedicle, between the superior and inferior articular processes. They serve for the attachment of muscles and ligaments. The **spinous process** of a vertebra is directed backward and downward from the junction of the laminae, and serves for the attachment of muscles and ligaments.

Each vertebra is composed of cancellous tissue, covered by a thin coating of compact bone; the latter is perforated by numerous orifices, some of large size for the passage of vessels. The interior of the bone is traversed by one or two large canals, for the reception of veins, which converge toward a single large, irregular aperture, or several small apertures, at the posterior part of the body. The thin bony lamellae of the cancellous tissue are more pronounced in lines perpendicular to the upper and lower surfaces and are developed in response to greater pressure in this direction (**Figure 2-5**). The arch and processes projecting from it have thick coverings of compact tissue. The cortical shell and bony endplates surrounding the vertebral body are very thin, ranging from 0.40 mm to 0.70 mm thick, Panjabi *et al.* (2001). Measured thicknesses of the cortical bone and bony endplates can be found in **Table 2-1**.

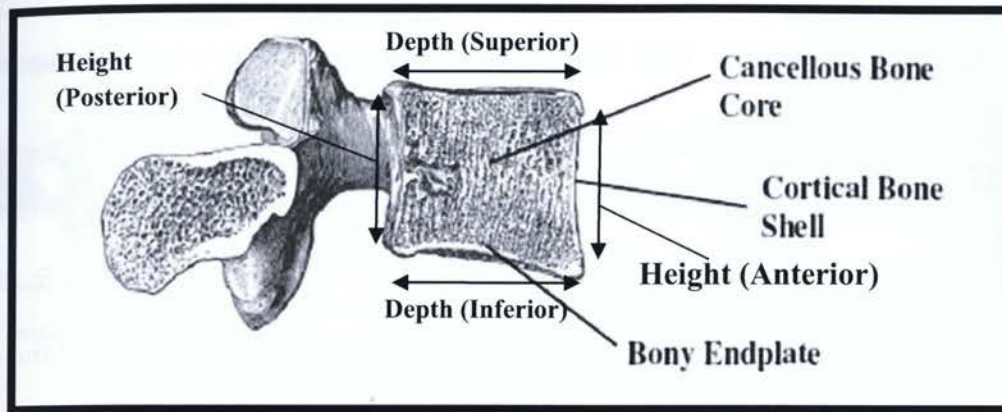


Figure 2-5: Sagittal section of a vertebra (Adapted from www.apparelyzed.com).

The seven cervical vertebrae are characterized by their small size and by presence of a foramen in each transverse process. The cervical vertebra body is short in height and square shaped when viewed from above and has a concave superior surface and a convex inferior surface. The spinous process of this kind of vertebrae is short and bifid, and its vertebral foramen is triangular in shape. Finally, its transverse process is trough shaped and perforated by a round foramen transversarium (**Figure 2-4**). The dimensions of the cervical vertebrae body as measured by Gilad and Nissan (1986) and Panjabi *et al.* (1991a) can be seen in **Table 2-1**.

The upper cervical spine is made up of two vertebrae, the atlas (C1) and the axis (C2), have forms that differ from those of all the other vertebrae, enabling them to support and secure the head and ensure its mobility.

The atlas (C1) articulates with the head (**Figure 2-6**). Its major distinguishing feature is that it lacks a vertebral body. When viewed from above, the atlas is ring-shaped and composed of two lateral masses interconnected by an anterior arch and posterior arch. Each lateral mass articulates above with an occipital condyle of the skull and below with

the superior articular process of the axis. The transverse processes of the atlas are large and protrude further laterally than those of the other cervical vertebrae, Drake *et al.* (2005).

The axis (C2) is characterized by the large tooth like dens, which extends superiorly from the vertebral body (**Figure 2-6**). The anterior surface of the dens has an oval facet for articulation with the anterior arch of the atlas. The two superolateral surfaces of the dens process circular impressions that serve as attachment sites for strong alar ligaments, one on each side, which connect the dens to the medial surfaces of the occipital condyles, Drake *et al.* (2005).

Table 2-1: Vertebral Dimensions and Bone Thickness.

Vertebral Body		C2 (mm)	C3 (mm)	C4 (mm)	C5 (mm)	C6 (mm)	C7 (mm)
Depth (Gilad et al., 1986)	Superior	12.6±2.1	14.8±1.5	15.5±1.7	15.5±1.7	16±1.7	16.4±1.4
	Inferior	15.3±1.6	15.6±1.5	15.8±1.5	16.1±1.5	16.6±1.4	16.3±1.4
Height (Gilad et al., 1986)	Anterior	19±3.2	14.1±1.3	13.4±1.3	12.7±1.3	13±1.3	14.6±1.4
	Posterior	16.6±2.5	14.5±1.4	13.9±1.2	13.8±1.4	13.9±1.6	14.9±1.4
Width (Panjab et al., 1991a)	Superior	-	15.8	17.2	17.5	18.5	21.8
	Inferior	17.5	17.2	17	19.4	22	23.4
Cortical Thickness (Panjab et al., 2001)	Anterior	-	0.51	0.55	0.62	0.66	0.70
	Posterior	-	0.41	0.41	0.44	0.49	0.48
Endplate Thickness (Panjab et al., 2001)	Superior	-	0.63	0.62	0.55	0.63	0.60
	Inferior	-	0.58	0.56	0.62	0.65	0.67

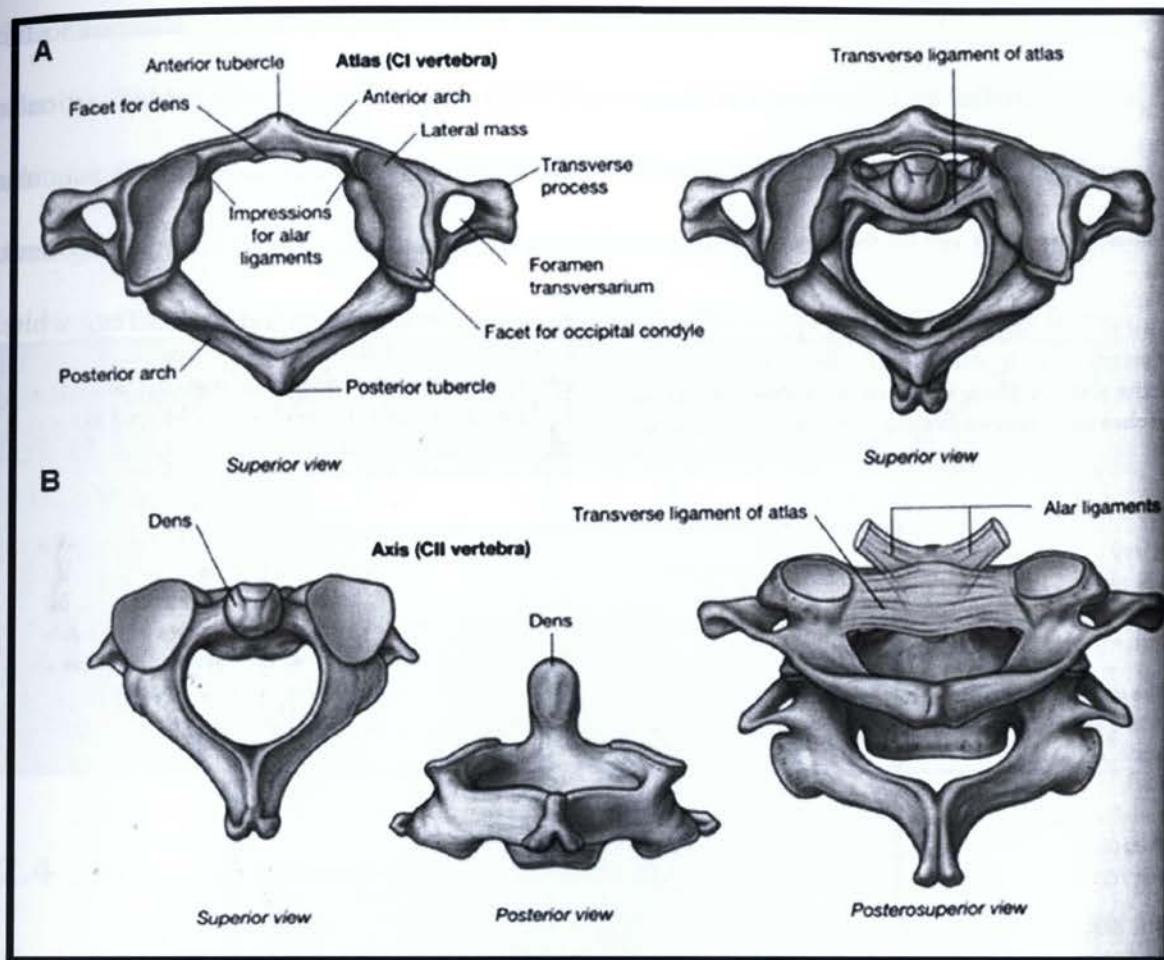


Figure 2-6: Regional vertebrae, A. Atlas (C1), B. Axis (C2) (Adopted from Drake *et al.*, 2005).

2.3.2 Vertebrae Joints

A typical vertebra has a total of six joints with adjacent vertebrae: four synovial joints (two above and two below) and two symphyses (one above and one below). Each symphysis includes an intervertebral disc.

The **symphysis** between adjacent vertebral bodies is formed by a layer of hyaline cartilage on each vertebral body and an intervertebral disc, which lies between the layers.

The **synovial** joints between superior and inferior articular processes on adjacent

vertebrae are the zygapophysial or facet joints. A thin articular capsule attached to the margins of the articular facets encloses each joint. There is a gap between the articular cartilages which is filled with synovial fluid that reduces friction between the articular cartilage and other tissues in joints to lubricate and cushion them during movement. Normal synovial fluid is clear, colourless and noticeably thick and stringy, like egg white. In cervical regions, the zygapophysial (facet) joints slope inferiorly from anterior to posterior (**Figure 2-7**). This orientation facilitates flexion and extension.

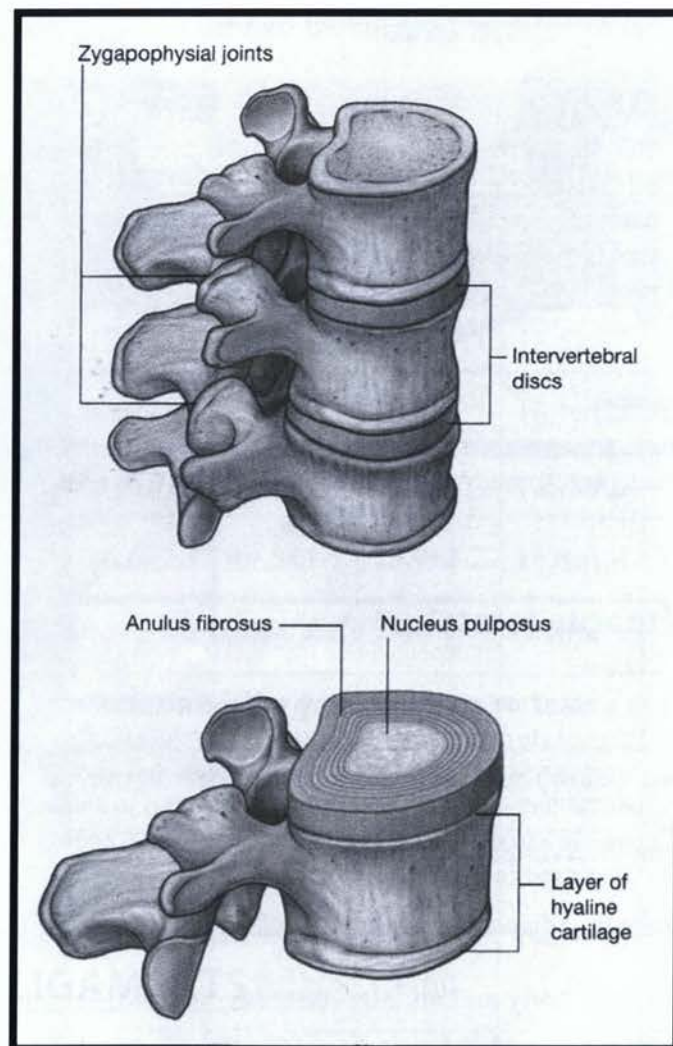


Figure 2-7: Vertebrae Joints (Adopted from Drake *et al.*, 2005).

The dimensions of the cervical facet joints as measured by Panjabi *et al.* (1993) can be seen in **Table 2-2**. Panjabi *et al.* (1993) measured the superior and inferior of the articular facet widths and heights of both left and right facet joints. **Table 2-2** shows the average of the left and right values.

Table 2-2: Superior and inferior articular facet linear dimensions.

Facet Joints		C2 (mm)	C3 (mm)	C4 (mm)	C5 (mm)	C6 (mm)	C7 (mm)
Height (Panjab et al., 1993)	Superior	17.9	11.6	12.2	11.6	11.0	11.4
	Inferior	12.4	12.4	12.3	11.2	12.3	12.7
Width (Panjab et al., 1993)	Superior	16.4	11.1	11.5	12.1	12.4	12.6
	Inferior	10.9	11.4	11.7	11.8	12.9	13.3

2.4 Intervertebral Disc Structure

The intervertebral discs (IVD) are soft tissue structures and make up one fourth of the spinal column's length. There are no discs between the Atlas (C1), Axis (C2), and Coccyx. The discs are flat, round structures about a quarter to three quarters of an inch thick with tough outer rings of tissue called the **Annulus Fibrosis (AF)** that contain a soft, white, jelly like center called the **Nucleus Pulposus (NP)**. Flat, circular plates of cartilage connect to the vertebrae above and below each disc (**Figure 2-8**). Each disc absorbs the stress and shock the body incurs during movement and prevents the vertebrae from grinding against one another. The intervertebral discs are the largest structures in the body without a vascular supply. The composition and structure of each component is quite distinct, suggesting that each component may have a unique mechanical role.

The Annulus Fibrosus (AF) has discrete fibrous lamellae and they appear as a layered composite with each adjacent lamina having a parallel collagen fiber arrangement varying at approximately $\pm 30^\circ$ to the horizontal axis. The AF is characterized by frequent interruptions in the lamellar structure, described by such structural properties as the percentage of incomplete layers and fiber interlacing angle, which occur more often in the posterior-lateral regions, Marchand and Ahmed (1999). The fibrillar network of the NP is looser and more random than the AF. The **Cartilage End Plate (CEP)** is a thin layer of hyaline cartilage which surrounds the surfaces of the central regions of the disc. The orientation of the collagen fibers and chondrocytes in the CEP has been shown to vary considerably with depth in the cartilage layer, Roberts *et al.* (1989), Iatridis (1996).

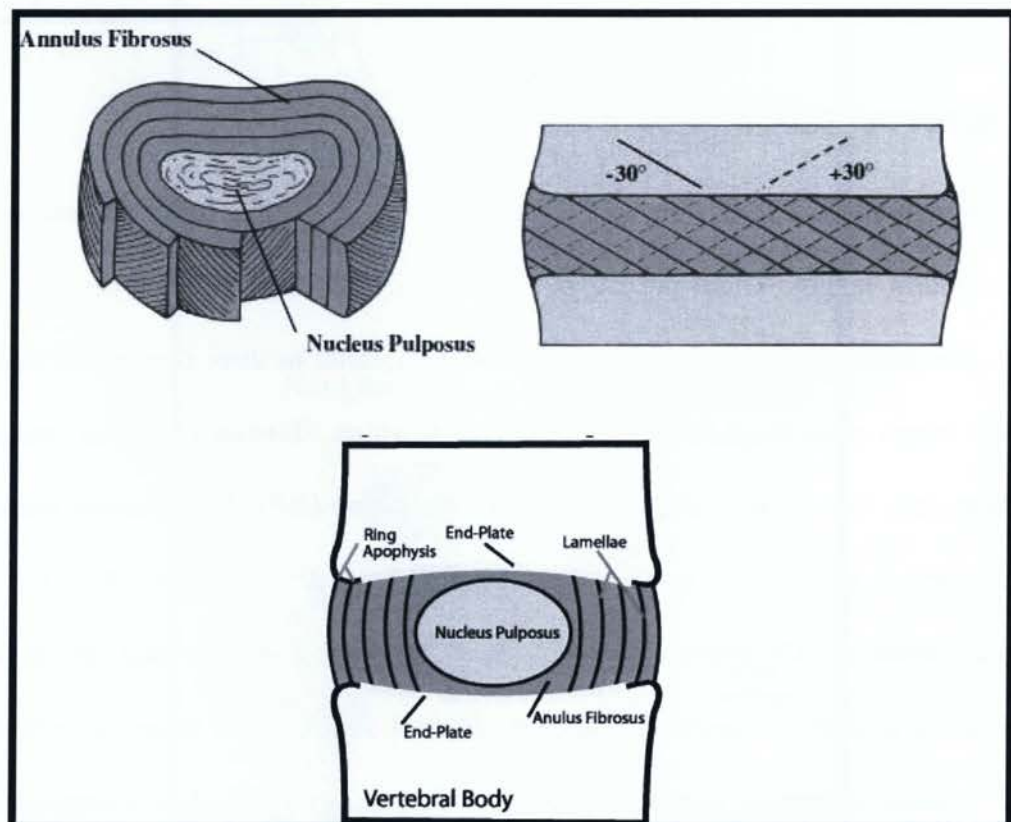


Figure 2-8: Intervertebral disc (Adopted from White *et al.*, 1990 & www.chirogeek.com)

The intervertebral disc is comprised mostly of water with significant quantities of collagen, proteoglycan, and other matrix proteins. Differences in composition and structure in the disc distinguish the different regions in the disc. The composition of the AF, NP and CEP of the intervertebral disc measured by Iatridis (1996) can be found in **Table 2-3**. The outer AF is predominantly type I collagen while the inner AF is mostly type II, with a decreasing ratio of type I/type II from outer to inner AF, Iatridis (1996). The collagen composition of the CEP is almost exclusively type II, and is similar in concentration and organization to that of articular cartilage, Roberts *et al.* (1989), Iatridis (1996). In healthy nondegenerated nucleus pulposus tissue, collagens account for approximately 20% of the dry weight. Type II collagen makes up about 80% of the total collagen content in the nucleus pulposus with small amounts of types II, V, VI, IX and XI collagen, Guerin (2005). The height dimensions of the cervical intervertebral disc as measured by Gilad and Nissan (1986) can be seen in **Table 2-4**.

Table 2-3: Composition of AF, NP and CEP.

Composition Type	AF	NP	CEP
Water (% wet wt)	60-70	70-90	60
Proteoglycan (% dry wt)	10-35	25-60	15-25
Collagen (% dry wt)	15-65	15-35	45-60
Proteins (% dry wt)	5-25	20-45	10-30

Table 2-4: Measured intervertebral disc heights.

Intervertebral Disc		C2 (mm)	C3 (mm)	C4 (mm)	C5 (mm)	C6 (mm)	C7 (mm)
Height (Gilad et al., 1986)	Anterior	4.8±1.0	5.3±0.9	5.5±1.0	5.4±1.0	5.2±1.0	4.7±1.2
	Posterior	3.4±1.0	3.3±0.9	3.0±1.0	3.0±0.9	3.3±1.0	3.5±1.2

2.4.1 Biomechanics of the Intervertebral disc

The disc task in the spine is to maintain flexibility and motion. Along with the facet joints, it is responsible for carrying all the compressive loading to which the trunk is subjected. This includes different types of loads and stresses, like dynamic loads, static loads, tensile stresses, torsional loads, shear stresses and a combination of tensile, compressive and shear stresses.

Compressive loads on the disc result in tensile hoop stresses in the outer annulus fibrosus, Shirazi-ADI *et al.* (1984). At the same time, it results in direct axial compressive stresses in the inner annulus fibrosus and radial compressive stresses from outward bulging of the nucleus pulposus (**Figure 2-9-B**). Water flows out of the disc as it is compressed, balancing osmotic pressure in the nucleus pulposus. The disc is loaded in compression for about 16 hours a day, therefore, a large amount of fluid is expressed. Overnight during rest, the disc is rehydrated and repressurized, Wilke *et al.* (1999). In bending or torsion, the fibers of the annulus fibrosus may be loaded directly in tension at same point around the circumference of the tissue, and bulging of the nucleus pulposus may occur in any direction (**Figure 2-9-C**), Guerin (2005).

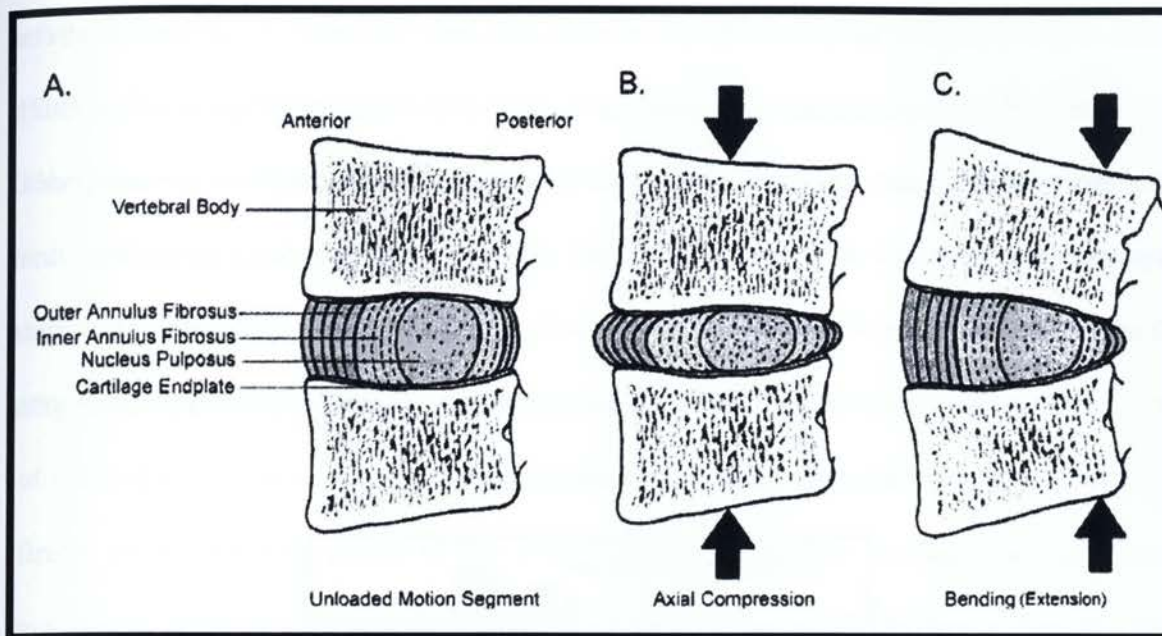


Figure 2-9: Motion segment loading scenarios. A. An uncompressed motion segment. B. Under axial compression. C. Under bending loads (Adopted from Guerin, 2005).

Recent studies have shown that the degeneration of the intervertebral disc results in a loss of demarcation between the nucleus and annulus fibrosus, a decrease in diurnal height changes as the disc loses its ability to rehydrate after loading, and altered loading on the disc and surrounding tissues. In addition, tissue structures of the disc undergo specific changes in composition and mechanical properties that contribute to the global loss of function in the degenerated disc, Kurtz *et al.* (2006).

2.5 Ligaments

Ligaments are fibrous bands of connective tissue linking two or more bones, cartilages, or structures together. One or more ligaments provide stability to a joint during rest and movement. Excessive movements such as hyper-extension or hyper-flexion may be restricted by ligaments. Further, some ligaments prevent movement in certain directions.

The cervical ligaments along with paracervical muscles prevent motion, between vertebrae, that might injure the spinal cord or nerve roots, Malanga *et al.* (2002), ligaments with the intervertebral discs form the primary static stabilizers of the cervical spine. The mid and lower cervical spinal ligaments are the Anterior Longitudinal Ligament (ALL), the Posterior Longitudinal Ligament (PLL), the Capsular Ligaments (CL), the Ligamentum Flavum (LF), the Inter-Spinous Ligaments (ISL), and the Super-Spinous Ligaments (SSL) as shown in **Figure 2-10**.

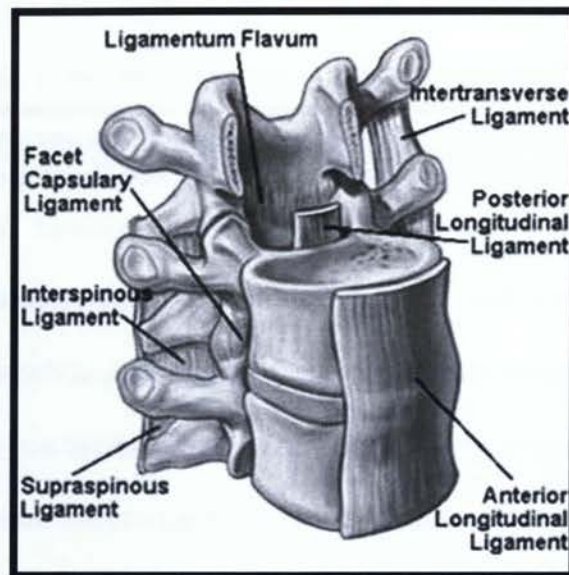


Figure 2-10: Liaments (Adopted form www.spineuniverse.com).

The **Anterior Longitudinal Ligament (ALL)** is a strong band, extending along anterior surfaces of the vertebral bodies and intevertebral discs, from the front of the sacrum to the anterior aspect of C2. The ALL is narrower in the upper cervical spine but is wider in the lower cervical spine than it is in the thoracic region. It is firmly attached to the superior and inferior end plates of the cervical vertebrae, but not to the cervical disc. In the waist

of the centrum, the ligament thickness fills in the concavity of the body. The ALL functions to restrict spinal extension and is thus vulnerable to hyperextension trauma.

The **Posterior Longitudinal Ligament (PLL)** is lying on the anterior aspect of the vertebral canal, it extends from sacrum to the body of axis (C2), where it is continuous with the tectorial membrane. The PLL travels over the posterior aspect of the centrum, attaching to the superior and inferior margins of the body, but is separated from the waist of the body by a fat pad and the basivertebral veins. In addition, this ligament attaches firmly to the posterior aspect of the IVDs, laminae of hyaline cartilage, and adjacent margins of vertebral bodies. The PLL is broader and considerably thicker in the cervical region than in the thoracic and lumbar regions. The PLL functions to prevent disc protrusions and also acts as a restraint to segmental flexion of the vertebral column, Dutton (2004).

The **Capsular Ligaments (CL)** surrounds the articular facets of adjacent vertebrae. They are short and strong fibrous structures that contribute to posterior stability and allow vertebrae to slide and rotate with respect to each other. They offer maximal mechanical resistance to flexion distraction but relatively poor resistance to rotation distraction.

The **Ligament Flavum (LF)**, on each side, passes between the laminae of adjacent vertebrae. These thin, broad ligaments consist predominantly of elastic tissue and form part of the posterior surface of the vertebral canal. Each LF runs between the posterior surface of the lamina on the vertebrae below to the anterior surface of the lamina of the vertebra above, Drake *et al.* (2005). It is a stronger ligament and it helps to restrain hyperflexion. The ligamentum flavum becomes shortened and thicker in hyperextension and elongated and thinner in hyperflexion, Malanga *et al.* (2002).

The **Super-Spinous ligament (SSL)** connects and passes along tips of the vertebral spinous processes from vertebra (C7) to the sacrum. From vertebra C7 to the skull, the ligament becomes structurally distinct from more caudal parts of the ligament and is called the ligamentum nuchae. The ligament nuche is a triangular, sheet like structure in the median sagittal plan. The base of the triangle is attached to the skull, from the external occipital protuberance to the foramen magnum; the apex is attached to the tip of the spinous process of vertebrae C7. Their function is to limit flexion of the cervical spine.

The **Inter-Spinous Ligaments (ISL)**, thin and membranous, connects adjoining spinous process and extends from the root to the apex of each process. They meet the ligamenta falvum in front and the supraspinal ligament behind. The ligaments are narrow and elongated in the thoracic region, broader, thicker, and quadrilateral in form in the lumbar region, and only slightly developed in the neck (**Figure 2-11**).

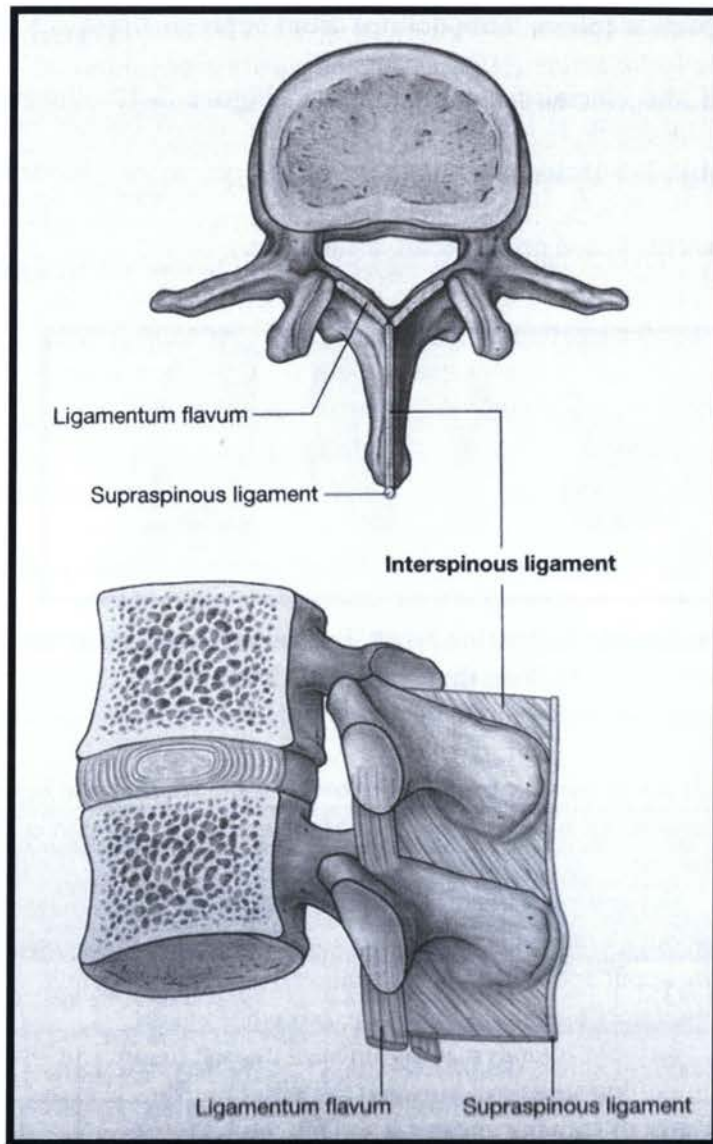


Figure 2-11: LF & SSL and ISL ligaments (Adopted from Drake *et al.*, 2005).

Yoganandan *et al.* (2000) measured and defined the lengths of the cervical spinal ligaments from sagittal sequential anatomic cryomicrotome device sections. This was done using four human cadaver specimens. The following definitions were used for ligament lengths in their analysis. The ALL and PLL were defined from the mid height of the inferior vertebral body to the mid height of the superior body. The LF and ISL were defined from superior points of attachment to the corresponding inferior points of

attachement. The joint capsules were defined from superior tip to the cephalad facet to the inferior tip of the caudal facet articulation. **Figure 2-12** illustrates a schematic representation. **Table 2-5** includes a summary of the geometric properties of the human cervical spine ligaments based on described definition.

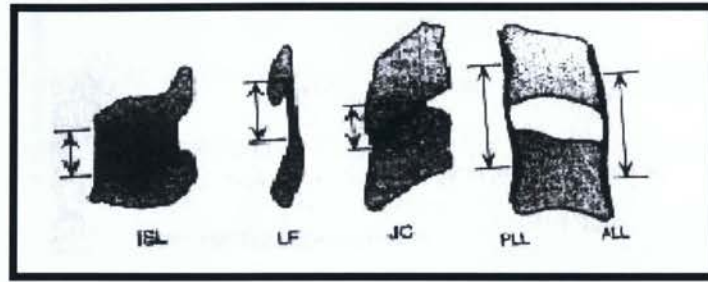


Figure 2-12: The length definition used for the various ligaments (Adopted from Yoganandan *et al.*, 2000).

Table 2-5: Area (n=4) and length (n=4) of cervical spine ligaments.

C2-C5			C5-T1	
Type	Area(mm ²)	Length(mm)	Area(mm ²)	Length(mm)
ALL	11.1±1.93	18.8±1.04	12.1±2.68	18.3±0.5
PLL	11.3±1.99	19.0±1.04	14.7±6.77	17.9±0.54
JC	42.2±6.39	6.92±0.68	49.5±12.28	6.72±0.45
LF	46.0±5.78	8.45±0.85	48.9±7.9	10.6±0.64
ISL	13.0±3.27	10.4±0.77	13.4±1.03	9.87±0.69

2.6 Spinal Cord

The spinal cord is located in the vertebral foramen and is made up of 31 segments: 8 cervical, 12 thoracic, 5 lumbar, 5 sacral and 1 coccygeal. A pair of spinal nerves exits from each segment of the spinal cord. In cross section, the spinal cord is composed of white matter and gray matter. The **gray matter** of the spinal cord form is H-shaped structure in the axial plane and varies in size according to the spinal level. Nerve cell bodies are located in the gray matter. Surrounding the gray matter is **white matter** (lighter color shading) which is where the axons of the spinal cord are located. From low sacral segments to high cervical segments, the volume of white matter increases progressively because the number of nerve fibers is larger in the high cervical sections

Figure2-13.

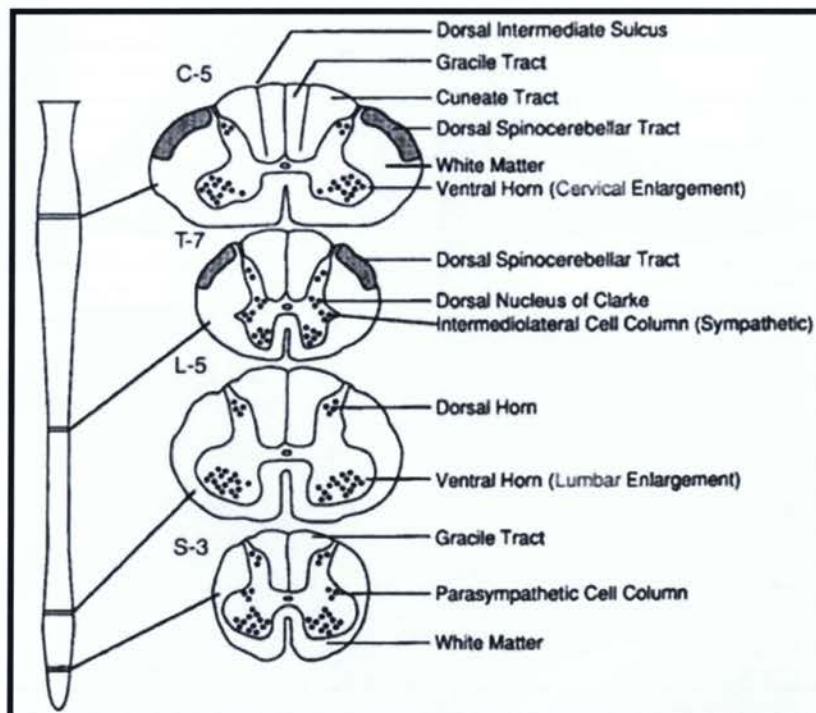


Figure 2-13 : Schematic diagram showing variations in spinal cord segments at different levels (Adopted from Afifi *et al.*, 2005).

The spinal cord is covered by three meningeal coats; these are the pia, arachnoid, and dura mater **Figure 2-14**. The arachnoid is closely adherent to the dura mater. The space between the dura and arachnoid is very narrow space visible with the aid of a microscope in histologic preparations in normal conditions. The space between the arachnoid and pia, in contrast, is wider and contains the cerebrospinal fluid (CSF). The spinal dura mater, unlike the dura within the skull, is firmly attached to bone only at the margin of the foramen magnum. Elsewhere, the spinal dura is separated from the vertebral periosteum by the epidural space. The spinal cord terminates at the level of the L1 and L2 vertebrae, whereas the dura mater extends down to the level of the S1 and S2 vertebrae, Afifi *et al.* (2005).

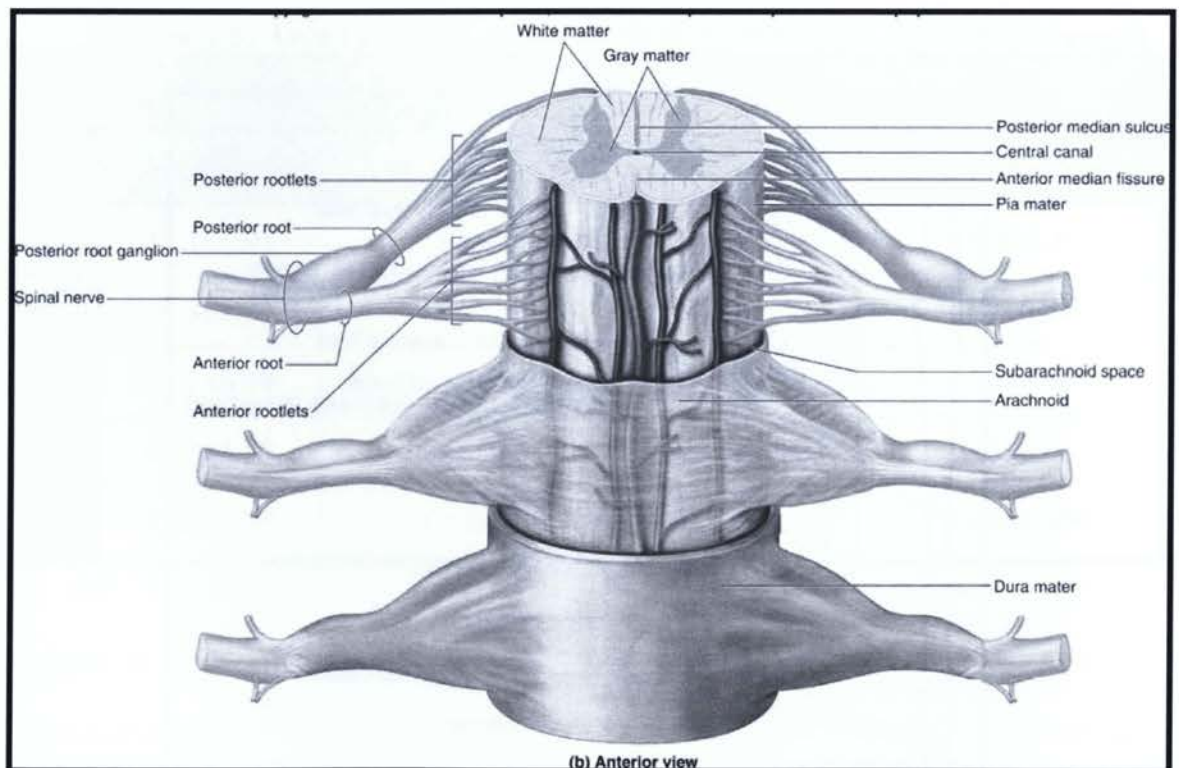


Figure 2-14 : Schematic of spinal cord showing the meningeal coats (Adopted from www.academic.kellogg.cc.mi.us).

The length of the spinal cord is much shorter than the length of the bony spinal column. It is about 45 cm long in men and 43 cm long in women. The shape of the cervical cord is essentially elliptical, through the degree varied at different levels. It is more circular at C2/3 and C7/T1 levels, but flatter at C3/4 to C6/7 levels. The cord measurements by Yu *et al.* (1985) are presented in **Table 2-6**. It shows that the sagittal diameter decreased progressively from C2/3 to C6/7. The cord transverse diameter is widest at C3/4 and C4/5 levels. The cord area was relatively constant from C2/3 to C5/6 level. **Figure 2-15** shows the locations of anteriorposterior and transverse diameters and transverse area.

Table 2-6 : Diameters and area of the cervical cord.

Type	Anteriorposterior Diameter (mm)	Transverse Diameter (mm)	Area(mm ²)
C2/3	7.8	12.8	85.1
C3/4	7.5	13.4	86.6
C4/5	7.1	13.8	87.0
C5/6	6.9	13.4	84.2
C6/7	6.8	12.6	76.9
C7/T1	7.0	10.9	70.3

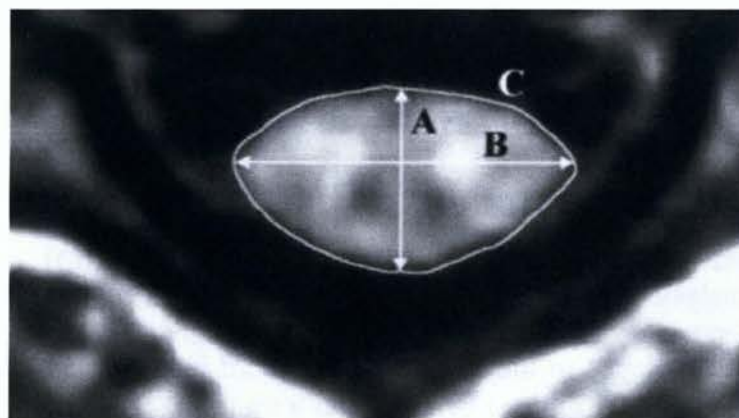


Figure 2-15: Measurements of the spinal cord. Anteroposterior diameter (A). Transverse diameter (B). Spinal cord area (C) (Adopted from Ishikawa *et al.*, 2003).

Chapter 3

Literature Review

3.1 Introduction

Experimental and numerical studies on the biomechanics of human cervical spine are important and challenging which have multiple clinical applications. Numerical models such as the finite element (FE) method are usually used to find the structural response to external loading and have important function in establishing the internal response such as stress and strain in response to external loading. An important step in creating the FE model is validating the FE results with experimental data obtained from *in vitro* human cadaver experiments. As such, this chapter presents a brief literature review of experimental and numerical studies to date in the following manner:

1. A review of the FE modeling performed on the human cervical spine will be presented.
2. A review of experimental studies on cervical spine from the early 1900s to date will be presented.

3.2 Finite Element Models

Finite element analysis is an essential part of many of today's engineering activities. The method was first developed in the 1950s in the aircraft industry and continues to be an indispensable tool in the design of most of the critical components in today's aircraft, Fagan *et al.* (2002a). One of the earliest FE analyses in human spine was reported by Liu

and Ray (1973) where they performed a FE analysis of wave propagation in human spine. Today, FE analysis plays an important role in simulation of biomechanical range of motion and stress and strain distribution of spinal column. The FE simulation allows testing and optimization of various prosthesis for patient specific applications from cartilage, disc replacement and instrumentation to hip and shoulder bone replacement. Finite element models of the human cervical spine are historically divided into two groups; first group represents a segment (vertebral body, disc and motion segment) of the cervical spine, and second group represents the entire cervical spine from the C7 vertebrae to the skull. This chapter provides an overview of each group in more detail.

3.2.1 Spine Segment FE Models

Segment models are typically a part of spine which is defined through arbitrary or naturally occurring boundaries. Segment used to describe single section of the spine (i.e., as a vertebral body or disc). These models are typically compared against experimental data involving simple quasi-static loading to focus on the load-carrying behavior of the local tissue. This section reviews a few of these literatures.

The FE models of single vertebrae have been used to analyze stress patterns in the vertebral bone during loading, in an effort to predict fracture mechanisms. For example, Bozic *et al.* (1994) developed a three-dimensional (3D) finite element model of a mid cervical vertebra (C4) using inhomogeneous material properties from quantitative computed tomography (CT) scan data (**Figure 3-1**). Their objective was to predict regions of high risk in vertebra during compressive loading. The material properties of the cortical and cancellous bone were assigned based on the CT scan apparent density.

The model was subjected to 4 mm axial compression through linear spring elements. They obtained higher shear stresses in the cancellous core and concluded that the regions of safety as determined by their model overlapped the fracture lines as frequently discovered clinically in a typical burst fracture. This model was a single vertebra model that lacked ligaments, facets and disc and therefore had very limited extension and applications.

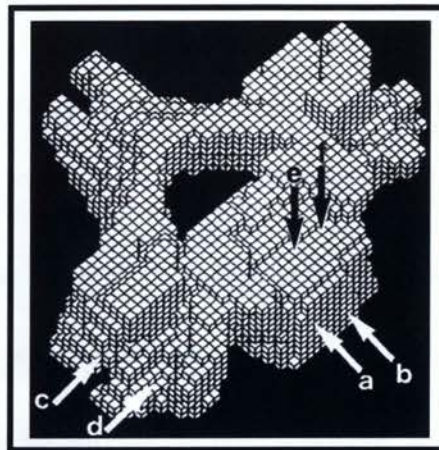


Figure 3-1: Finite element model of a C4 vertebra (Adopted from Bozic *et al.*, 1994).

The intervertebral disc (IVD) is the most critical component in most finite element models of the spine as indeed it is in the natural spine, and its representation in the models is therefore of great importance , Fagan *et al.* (2002b). Therefore, there have been a number of FE models of intervertebral discs reported in the literature and most of those have used the FE models to study loading conditions or material behavior of the disc which may not be easily achieved experimentally. For example, Belytschko *et al.* (1974) were the first to present details of a finite element analysis of an IVD and adjacent lumbar vertebrae. They used an axisymmetric FE model to study the behavior of an IVD under axial loading condition (**Figure 3-2**). All material models were linear isotropic

elastic except for the annulus fibrosus (AF) that was linear orthotropic. The model indicated that the mechanical stress-strain state of the nucleus pulposus is isotropic, while that of the AF was highly anisotropic. Their results were then presented on the effects of material properties and geometry on the stress-distribution and intradiscal pressures. They found that the hoop stress was greatest at the periphery of the IVD with a predicted value of 3.35 times the applied pressure. This model was later redeveloped by Kulak *et al.* (1976) to include a nonlinear orthotropic representation of the annulus fibrosus for a more accurate response.

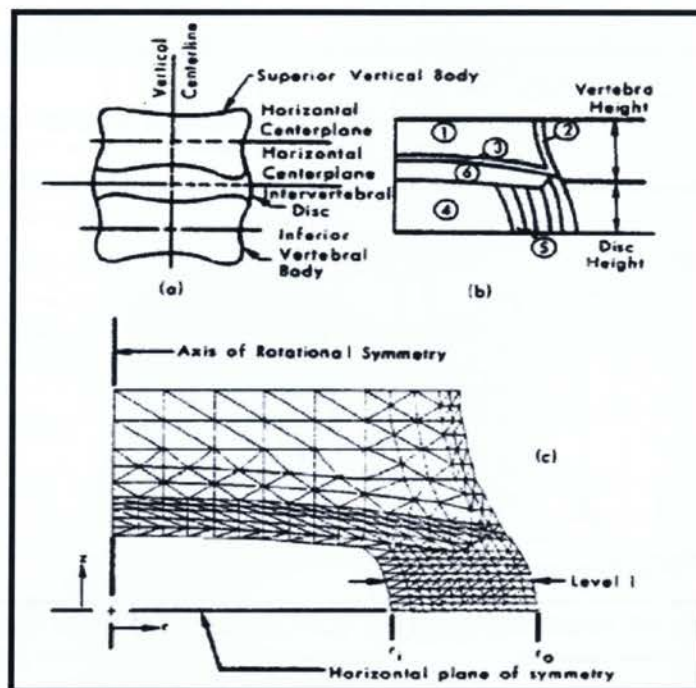


Figure 3-2: Finite element model of IVD (Adopted from Belytschko *et al.*, 1974).

Other studies have used 3D models with more realistic geometries of the IVD and vertebral bodies. For example, Shirazi-Adl *et al.* (1984) developed a 3D nonlinear finite element model of the lumbar (L2-L3) body-disc-body in which the nucleus pulposus

modeled as an incompressible, inviscid fluid and annulus was represented as a composite material of collagenous fibers embedded in a ground substance (**Figure 3-3**). The axial elements used to model the fibers of the annulus in a crisscross pattern with nonlinear properties to reflect the softening of the fibers at higher strains. Under compressive load, the states of stress and strain were computed, and the results showed that the most vulnerable elements are the cancellous bone and the endplate.

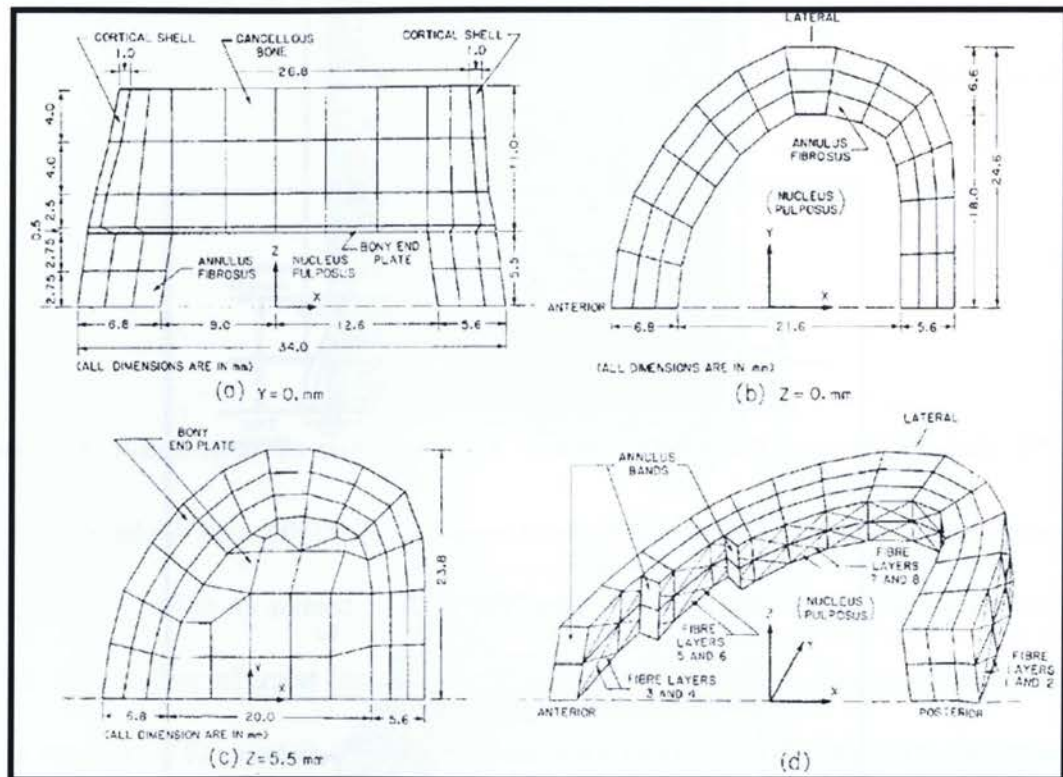


Figure 3-3: The 3D nonlinear model of L2-L3 (Adopted from Shirazi-Adl *et al.*, 1984).

This basic model was developed further to include contact at the facet joints and nonlinear tension-only truss elements for ligaments under pure sagittal plane moments to further advance the capabilities in complex loading, Shirazi-Adl *et al.* (1986), and latter under combinations of more complex loading conditions, Shirazi-Adl (1991). They also

examined the effects of facet geometry in detail and undertook a more detailed examination of the constitutive models of the annulus, Shirazi-Adl (1989), the role of the nucleus pulposus, Shirazi-Adl *et al.* (1992), and the effects of the bone's properties, Shirazi-Adl (1994). Furthermore, Agroubi and Shirazi-Adl (1996) modified the model again to include poroelastic properties for the disc. They investigated the 3D poroelastic creep response of a lumbar motion segment under constant axial compression. The annulus bulk was modeled as a nonhomogeneous composite of collagenous fibers and annulus bulk (Figure 3-4). They studied the role of facet joints, strain-dependent variable permeability, boundary pore pressure, and coupled sagittal rotation on the creep response. Their results showed that the strain dependent variable permeability and boundary pore pressure stiffen the response and decrease forces on the facets.

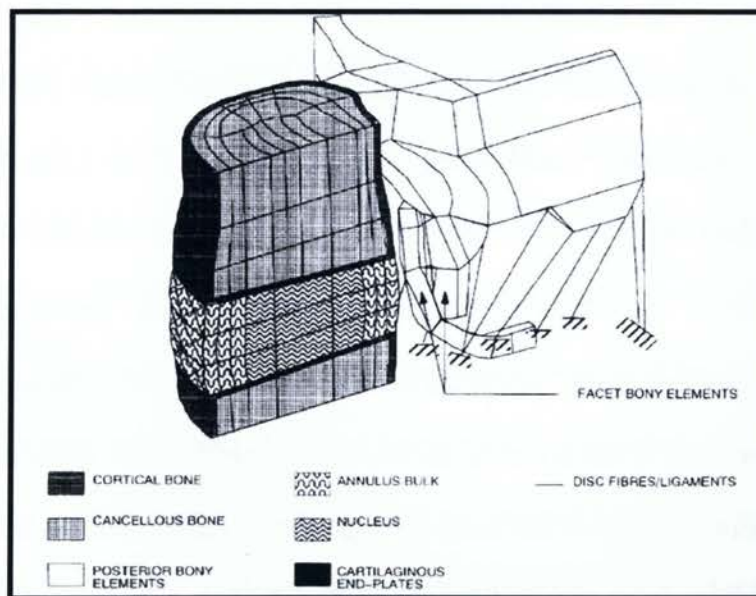


Figure 3-4: The 3D nonlinear model of L2-L3 (Adopted from Shirazi-Adl *et al.*, 1996).

Numerous other researchers have also reported analysis with one or more motion segments. For example, the first significant cervical spine segment model was developed

by Yoganandan *et al.* (1996b). They used 1.0 mm CT slices to develop the first most anatomically correct model of the C4, C5 and C6 vertebrae (**Figure 3-5 A**). Eight-node brick elements were used to generate the cancellous bone and discs. Four-node shell elements were used for the cortical bone and the endplates. The material properties of the spinal components were assumed to be linear, homogeneous and isotropic. The discs were represented as continuum material and the facets were assumed to be 3D solids. The validation was done in axial compression using the Shea *et al.* (1991) experimental data from a complete cadaver model of the cervical spine. The model lacked some details at the disc and ligaments levels. This model was later redeveloped by Kumaresan *et al.* (1997) to include a better model of the disc and ligaments. The disc was modeled with annulus fibers and ground substance in combination with linear elastic solid elements for the nucleus pulposus, which is the first model to include anisotropic behavior of the disc. Nonlinear spring elements were used to model the ligaments (**Figure 3-5 B**). Validation was performed in quasi-static compression, flexion, and torsion. In addition, Kumaresan *et al.* (1999) studied the effect of variations in the material properties of the cervical spinal components on the output of the finite element analysis (external and internal responses of the cervical spine) under physiologic load vectors. Although their model was physically complex, it did not consider any non-linearity in the material properties of the disc or ligaments nor did it use nonlinear geometry. Later, Kumaresan *et al.* (2001) used their previous model to quantify the overall and internal responses of the cervical spine during progressive degenerative changes in the intervertebral disc and to investigate the plausible biomechanical reasons for the formation of osteophytes during disc degeneration. Their results showed that the overall stiffness of the spine increased with

increasing severity of degeneration. In addition, the intervertebral disc bulge, and annulus stress and strain decreased at the degenerated level.

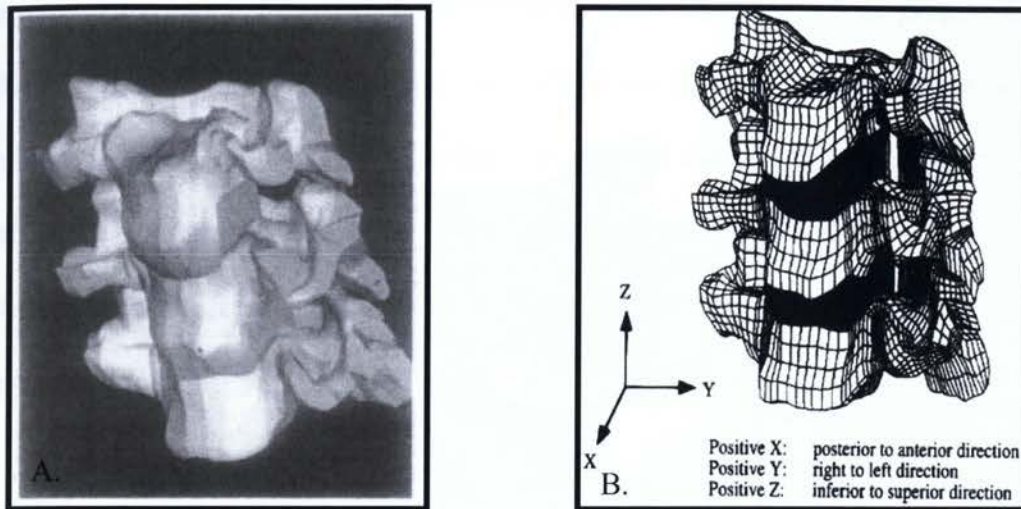


Figure 3-5: 3-D finite element model of C4-C5-C6. A. Yoganandan *et al.*, 1996b and B. Kumaresan *et al.*, 1999.

Clausen *et al.* (1996 and 1997) developed 3D symmetric model of C5-C6 motion segment based on the geometry of a 68-year-old man as obtained through CT scans at slice intervals of 1.5 mm (**Figure 3-6**). The model included the two vertebrae, a composite disc and all the articulations. The model employed bi-linear elastic, tension-only cable elements for ligamentous structures. Facet surfaces were oriented manually at 45 degrees from the transverse plane, and articulation was modeled using gap elements. The annulus fibrosus was modeled using a linear elastic hexahedral matrix representation, with tension-only cable elements that defined six distinct layers of fiber reinforcement. The nucleus pulposus was modeled as an incompressible fluid. Hexahedral elements, with isotropic, linear elastic material properties were used for cortical, cancellous, and end plate structures. The model was subjected to an axial compressive load (73.4 N) and

to 1.8 Nm bending moments. This was compared to the experimentally obtained data of Moroney *et al.* (1988) and the results were in excellent agreement.

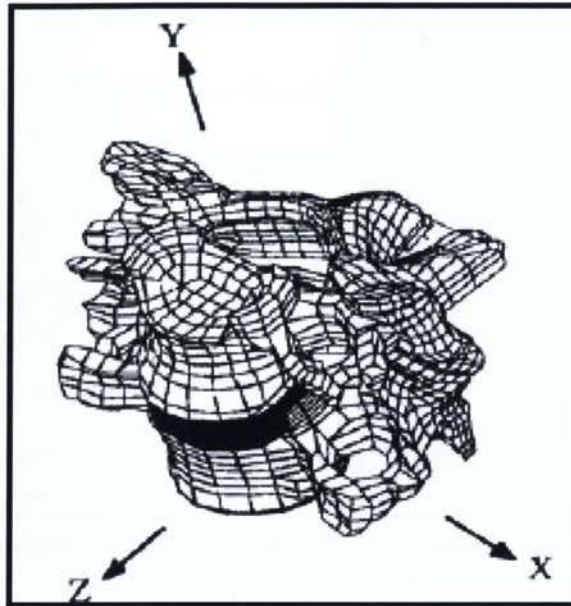


Figure 3-6: 3D finite element of C5-C6 (Adopted from Clausen *et al.*, 1997).

Maurel *et al.* (1997) developed a 3D model of the complete lower cervical spine (C3-C7) and used the model to compare the characteristics of 53 lower cervical vertebrae, whose key geometric features were obtained by a coordinate measuring machine. They studied the effect of the facet joint geometry on its biomechanical response. The model contained cortical shell, cancellous core, the endplates, composite discs, and the major ligaments (**Figure 3-7 A.**). The vertebrae were assumed to be symmetrical with regard to the sagittal plane. The material properties of the spinal components were assumed to be linear, homogeneous and isotropic. In this study, the model was analyzed in flexion, lateral flexion, axial torque and extension. The authors computed the principal and the coupled motions for various facet angles and concluded that the orientation of the facets governed both the principal and the couple motions.

Wheeldon *et al.* (2008) modeled a FE model of young adult human cervical spine (C4-C7). The model used a three-zone composite disc and a nonlinear spring elements for ligaments. Hexahedral elements, with isotropic, linear elastic material properties were used for cortical, cancellous, and end plate structures (**Figure 3-7 B.**). The model was validated against their experimental data for normal, nondegenerated cervical spines tested in flexion and extension, right and left lateral bending, and right and left axial rotation. The FE results were found to be within one standard deviation of the experimental results.

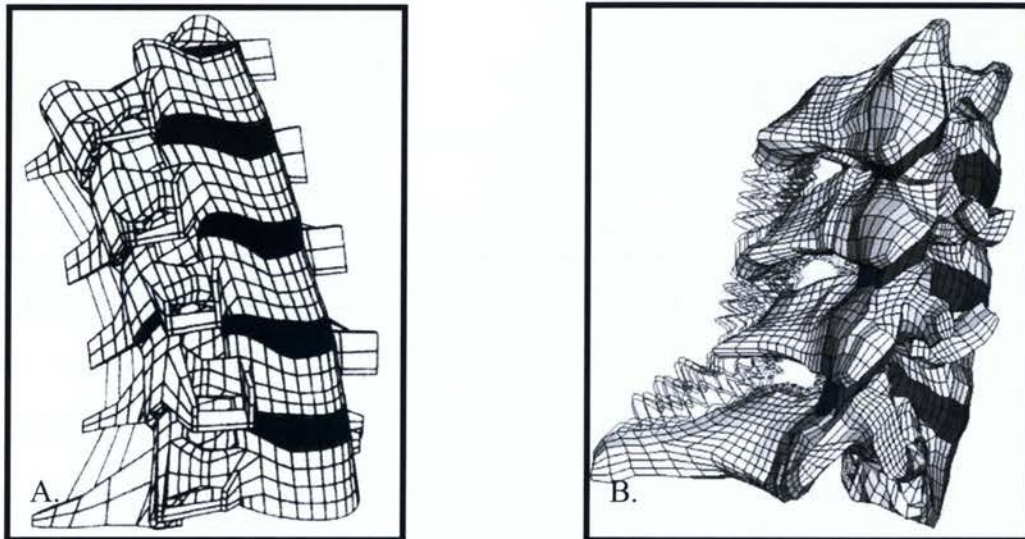


Figure 3-7: 3D finite element model of cervical spine, A. C3-C7 model of Maurel *et al.*, 1997 and B. C4-C7 model of Wheeldon *et al.*, 2008.

Scifert *et al.* (2002) developed a 3D, nonlinear FE model of C5-C6 with the cervical spine cord placed in ligamentous motion segment (**Figure 3-8**). The material properties of the spinal components were assumed to be linear, homogeneous and isotropic. Compressive loads along with flexion and extension moments were applied to the bony segment. Motion data shown in flexion and extension were calculated and validated

against different *in vivo* experimental data. The authors computed the von mises stress plots and strains on the cervical spinal cord and were compared with Yvan *et al.* (1998) published data. The results showed that the posterior surface of the cord was strained more than the anterior surface during flexion, which was in agreement with the published data. This model represents a first attempt by the authors to analytically quantify the mechanical response of the spinal cord to cervical spine injury.

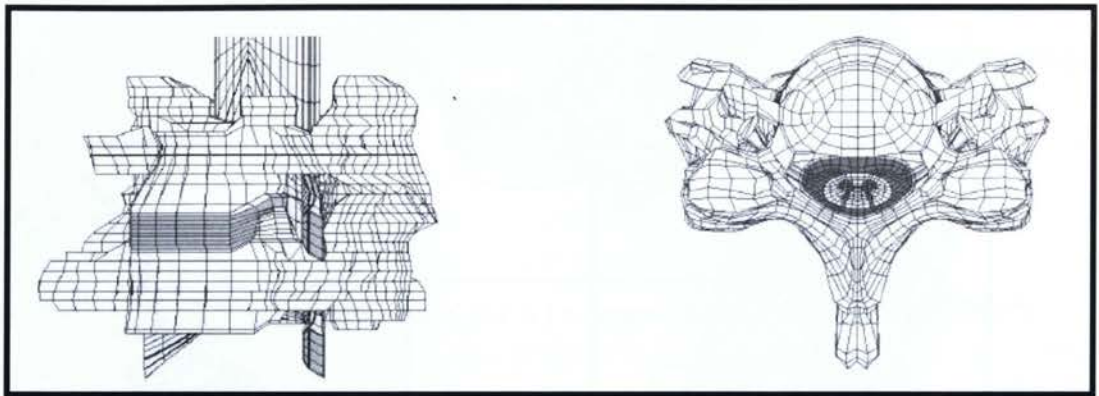


Figure 3-8: C5-C6 model of cervical spine with spinal cord (Adopted from Scifert *et al.*, 2002).

Later, Greaves *et al.* (2008) developed a 3D FE model of a three vertebrae (C4-C6) segment of the human cervical spine and spinal cord (**Figure 3-9**). The dura mater was modeled with 3D shell elements with four nodes. The ligaments and discs were modeled using links. Linear elastic material properties were assigned to the tissues. They investigated the differences in cord strain distributions during various column injury patterns. The results showed that for a distraction injury, relevant to column distortion injuries, a 2.6 mm axial displacement to the cord resulted in more uniform strains throughout the cord and low peak strains. For a dislocation injury, as would occur in a fracture dislocation, an anterior displacement of C5 corresponding to 30% of the sagittal

dimension of the vertebral body resulted in high peak strain values. This study was the first 3D model of spinal cord that includes verification of cord displacements under static load.

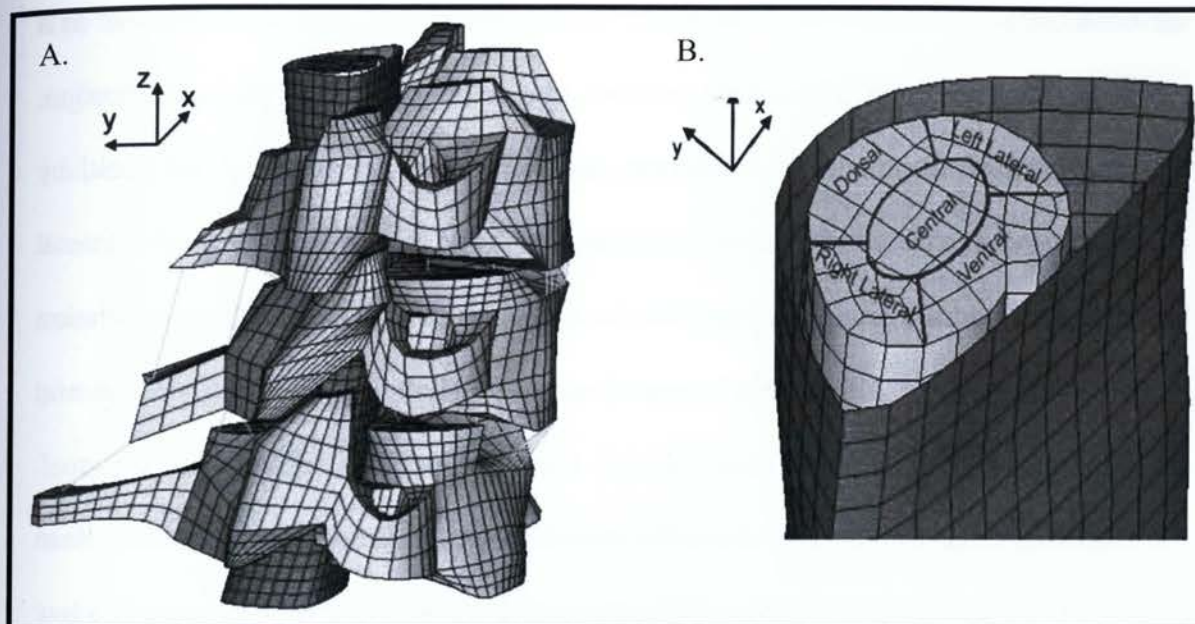


Figure 3-9: A. Anterolateral view of the C4-C6 vertebrae, spinal cord and connecting ligaments. B. Anterolateral view of the spinal cord and dura matter (Adopted from Greaves *et al.*, 2008).

3.2.2 Full cervical spine Models

Full cervical spine modeling is primarily of interest to clinicians and biomechanical engineers from the point of view of cervical spinal cord injury. Also, these models are typically compared against experimental data involving dynamic or impact loading. To date, there has been much less effort spent on modeling the full model cervical spine and its components than a full model of lumbar or thoracic human spine. The first 3D model of the cervical spine (head-T1) was reported by Kleinberger in 1993 and is shown in **Figure 3-10 A**. It included a rigid head and was made for dynamic simulations. The

vertebrae were rigid bodies, the intervertebral disc was homogenous, and the ligaments were modeled with brick elements. All soft tissues were given isotropic, linear elastic material properties. The upper cervical spine was modeled as separate vertebrae and included the odontoid process on the axis. The occipitoatlantal joint was simplified as a pin joint, allowing for rotation about one axis and maintaining atlas contact in tension. The author used the model to investigate the large strain response of the neck, by applying a forced axial displacement of 10 mm at C1, and also to simulate an 8 G frontal crash sled test and the results revealed that the head rotation lags behind the neck rotation by about 12 degrees. Kleinberger's model was validated for axial compression and frontal impacts.

Jost and Nurick (2000) developed another complete finite element model of the human head-neck that was used to simulate the dynamics of the head and neck subjected to low and high lateral deceleration (**Figure 3-11**). The vertebrae were modeled with shell elements to simulate the cortical bone. The cancellous bone in the vertebrae was neglected. Ligaments were modeled with tensile membrane elements with linear elastic material properties, in combination with spring-damper elements to model the viscoelastic material behavior. The first cervical vertebra C1 consists of two lateral masses connected by an anterior and posterior arch. The posterior wall of the anterior arch of C1 forms with the dens of the second cervical vertebra C2 a rotational pivot which provides multiple degrees of freedom for the head movement. The lower and upper cervical spine was modeled with anatomical detail. The model was validated at low and high G-level lateral accelerations and only the resulting head motion was evaluated.

Ng, Teo, and colleagues have published a number of articles outlining the development and application of a nonlinear model of the lower cervical spine, to cite a few, Ng and Teo 2001, 2004, 2005; Ng, Teo, and Lee 2004; Ng, Teo, and Zhang 2005; Ng *et al.* 2003; Teo and Ng 2001; Teo *et al.* 2004. Their C2-C7 model assumes symmetry about the sagittal plane (**Figure 3-10 B**). Each vertebra modeled using solid brick elements included the cortical bone, cancellous bone, and posterior structures. Posterior articular facets were simulated using 3D nonlinear contact elements. Each intervertebral disc consisted of disc annulus, disc nucleus, unconvertbral joint, annulus fibers, and end plates. All ligaments were model using nonlinear two node tension-only cable elements. Isotropic linear-elastic material properties were assigned to the hard tissue structures, as well as for the matrix of the annulus fibrosus. Two-noded nonlinear tension-only cables were used to model the fiber reinforcement of the annulus fibrosus. A fluid material representation was used for the nucleus pulposus. Their model was validated for flexion and extension within the published experimental data and has been used for different purposes. For example, in 2001, Ng and Teo used C4-C6 segment of the model to analyze the force-displacement response and disc bulging of the cervical spine related to changes in the modeling techniques and the disc components.

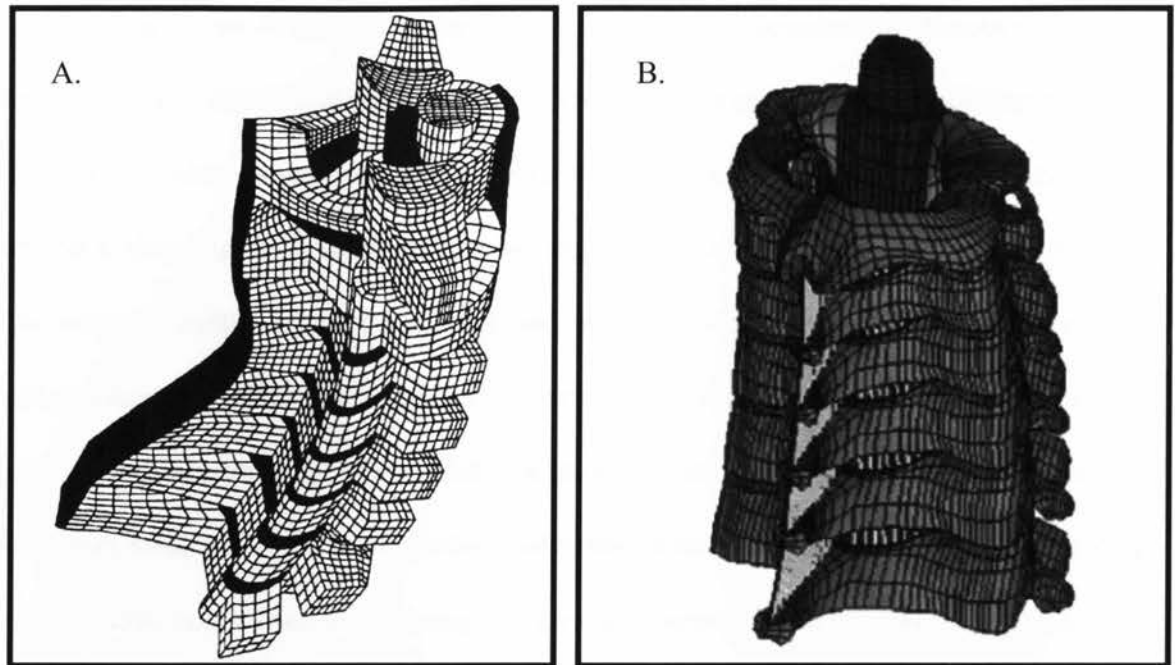


Figure 3-10: 3D full finite element model of cervical spine, A. C1-T1 model of Kleinberger, 1993 and B. C2-C7 model of Ng, Teo and Zhang, 2005.

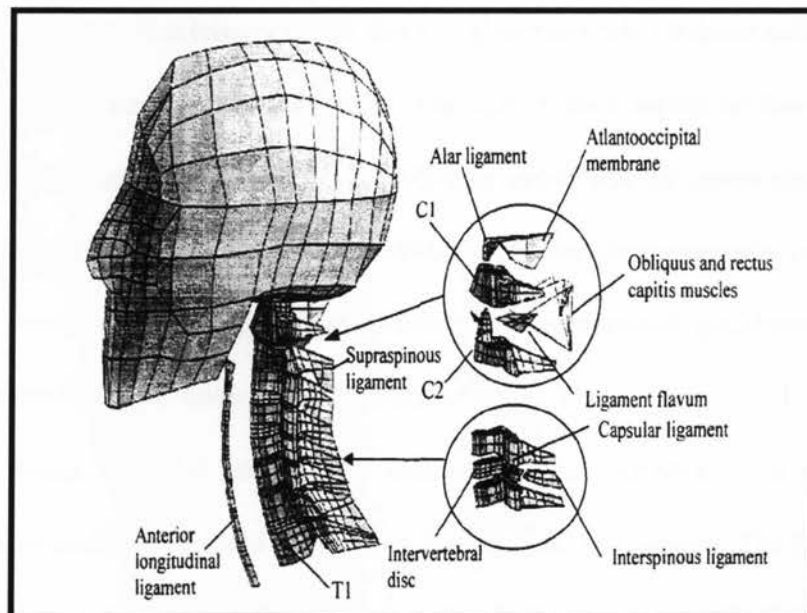


Figure 3-11: 3D finite element model of head-T1 (Adopted from Jost and Nurick, 2000).

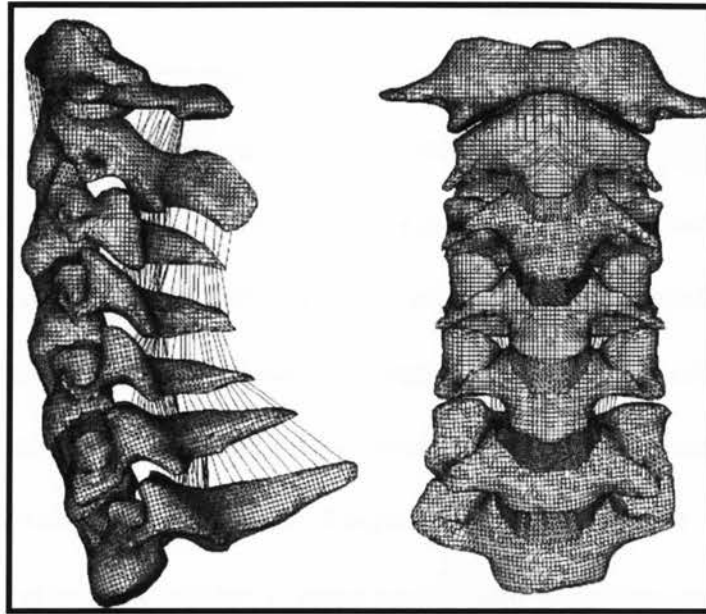


Figure 3-12: 3D finite element of C0-C7 (Adopted from Palomar *et al.*, 2008)

Palomar *et al.* (2008) developed a 3D finite element model of C0-C7 multi-level cervical spine to study the internal stresses and strains of the intervertebral disc under quasi-static loading conditions (**Figure 3-12**). The discs were modeled as nonlinear, anisotropic and incompressible subjected to large deformations. The vertebrae were treated as rigid bodies; therefore, the bones were meshed using triangle and quadrilaterals elements. The ligaments were modeled using nonlinear truss elements. The model was subjected to flexion-extension moments from 0.5 to 2 Nm. This was compared to the experimentally obtained data of Wheeldon *et al.* (2006) and the results were in excellent agreement. Also, their results have shown that the use of a fiber reinforced model to describe the behavior of the annulus of the discs would predict higher maximum shear strains than an isotropic one.

In the reviewed models, either some soft tissues were missing or the geometry of the spinal components were modeled very simplistic and were assumed to be symmetric. A

detailed and anatomically accurate 3D model could offer a better insight and will lend itself to a more physiologically accurate simulation of the human cervical response to external loading. Therefore, there is a need for an anatomically accurate model. In light of the first objective of this research, an accurate 3D FE model of cervical spine segment consisting of C3 to C5 with spinal cord and all ligaments has been developed. This model was utilized to study the effect of external loading and was validated against the published experimental data. There have been very few studies that have considered the spinal cord into their cervical spine model. Moreover, little is known about the relationship between vertebral motion and spinal cord distortion. Therefore, one of the objectives of this study is to develop anatomically accurate model of spinal cord and to study its behavior under various loading conditions.

Most of the previous models considered bone as an elastic material and the discs as an elastic or viscoelastic material. Therefore, one of the main goals of this study was to develop finite element model of middle cervical spine based on a linear, isotropic, two-phase material model (biphasic) for the vertebrae and discs.

3.3 Experimental Studies

Knowledge of the load-displacement properties of the spine is useful in understanding its mechanical behavior and for investigating a number of spine pathologies, Moroney *et al.* (1988). Therefore, several investigations have examined the strength of the cervical spine *in vitro*. For example, Moroney *et al.* (1988) reports the load-displacement behavior of 35 fresh human cadaver cervical spine motion segments tested in compression, shear, bending and axial torsion. Maximum loads used were 73.6 N of compression, 21.6 Nm

bending, and 39 N of shear. For each mode of loading, principal and coupled motions were measured and stiffnesses were calculated. Their results showed that the stiffness of the cervical motion in compression were similar to those of thoracic and lumbar motion segments. However, in other modes of loading, cervical stiffnesses were considerably smaller than thoracic or lumbar stiffness. Furthermore, the authors studied the influences of both the intervertebral disc level and the degree of degeneration. The results showed that the degenerated cervical disc segments were 50% less stiff in compression and three times stiffer in shear than less-degenerated segments.

Shea *et al.* (1991) conducted a study to determine the biomechanical properties along the human cervical spine and investigated the mechanism of injuries for sagittal plane loadings using 18 fresh human cadavers. First, they determined the *in vitro* load-displacement response of the mid (C2-C5) and lower (C5-T1) cervical spine for combinations of sagittal plane, and those pre-torqued axially. Second, they measured possible variations in the load-displacement and failure properties for each level. The t-test comparisons of a unpaired specimens results showed that the mid cervical region was stiffer in compression than the lower region and stiffer in extension than specimens from the lower region. The strength of mid cervical specimens was 7 Nm with a mean flexion angle of 26 degree at failure. The strength of the lower cervical spine with combined flexion-compression loading was 12.1 Nm and 2158 N. Also, their results showed that at up to 300 N axial forces, all specimens were significantly stiffer in compression than in tension. The authors also applied 150 N shear forces and noticed no significant difference between the posterior and anterior shear.

Physicians and biomechanical engineers are in need of comprehensive and representative data concerning the segments of the human spine, Gilad *et al.* (1986). As a result, few studies have investigated the geometric dimensions and relations of the vertebra and disc. In experimental studies of Gilad *et al.* (1986), the geometric configuration and dimensions of the human vertebrae were investigated using x-ray photographs of 157 normal, healthy men. The results showed that the average height of a cervical vertebrae is about one half that of a lumbar vertebrae. The intervertebral spacing are more variable, but the average cervical spacing is also nearly one half that of the lumbar one. In 1993, Panjabi and colleagues reported quantitative 3D surface geometry in the form of linear, area, and angular dimensions of the articular facets of the spine from C2 to L5 vertebrae. Later, Panjabi and colleagues (2001) quantified the cortical shell and endplate thicknesses, and external dimensions such as angles formed by adjacent walls, wall concavities, and heights and depths of the vertebral bodies in the middle and lower cervical spine regions. The results showed that the anterior cortical shell was thicker than the posterior cortical shell at all spinal levels. The central region of the superior endplate was consistently thinner than the corresponding region of the inferior endplate, making it relatively more prone to fracture. Yoganandan *et al.* (2000) determined the lengths and cross-sectional areas of the five ligaments from eight human cadavers. Further, the biomechanical force-deflection, stiffness, energy, stress, and strain data were obtained from 25 cadavers using *in situ* axial tensile tests. It was found that for all ligaments, cross-sectional areas were higher in the C5-T1 than in the C2-C5 group; and lengths were higher in the C2-C5 than in the C5-T1 group with the exception of the flavum. The results showed that the failure strains were higher for the ligaments of the posterior than

the anterior ligaments. In contrast, the failure stress and young's modulus were higher for the anterior longitudinal ligaments as compared to the ligaments of posterior ligaments.

Other researchers have also examined the flexibility of the cervical spine over a range of flexion and extension moments using either the entire cervical spine or individual motion segments. Nightingale *et al.* (2007) tested 41 male spinal segments (C0-C2, C3-C4, C5-C6, and C7-T1) in flexion-extension. Loads of +/- 3.5 Nm were applied at 0.5 Nm increments and held for 30 seconds to reach an equilibrium position. The results were compared with a previous study (Nightingale *et al.* (2002)) of females and showed that the male upper cervical spine was stiffer than the female and stronger than the female in flexion/extension.

Wheeldon *et al.* (2006) used seven young, normal fresh adult cadaver cervical spine segments C2-T1 ranging age from 20 to 51 years. Spine segments were tested in flexion-extension. The authors applied 0.33, 0.5, 1.0, 1.5 and 2 Nm ranges of loads to specimens. The results showed greater flexibility in flexion and less flexibility in extension than results previously reported in the literature. Also, the flexion-extension curves are asymmetric with a greater magnitude in flexion than in extension.

There are few experimental studies that have focused on the spinal cord deformation and movement *in situ* during both physiologic and traumatic loading conditions. For example, Bilston (1994) measured the *in vivo* quasi-static motion of the cervical spinal cord in human during neck flexion and extension using a motion tracking magnetic resonance imaging (MRI) technique. The results showed that the spinal cord moves and deforms considerably during the flexion and extension maneuvers within the normal range of motion. Also, as a result of full flexion, they observed slight inferior movement of the

upper cord and larger superior movement of the lower cord. However, the study was limited to the anterior surface of the spinal cord in two volunteers. Sometimes latter, Yuan *et al.* (1998) investigated the deformation and movement of both anterior and posterior surfaces of the cervical spinal cord during flexion of the neck in a larger cohort of human volunteers using a spatial modulation of magnetization (SPAMM) pulse sequence. To that end, a custom designed device was built to guide the flexion of the neck and enhance motion reproducibility. The results showed that between a neutral posture and full flexion, the entire cord (C2-C7) elongated linearly with head flexion, increasing 10% and 6% of its initial length along the posterior and anterior surfaces, respectively. Average displacement was on the order of 1-3 mm, and varied with region. An important step in creating the FE model is validating the FE results with experimental data obtained from *in vitro* human cadaver experiments. Therefore, in the next chapters, some of these experimental studies will be used for validation and comparison.

Chapter 4

Model Development

4.1 Model Construction

A previously developed surface cervical model of 25-30 year-old healthy male was imported into finite element pre-processing software (Hypermesh 8.0 Altair Engineering Inc., Troy, MI) and MSC.Marc (MSC Software Copr., Los Angeles , U.S.A). The data conversion procedure for developing the surface cervical model used previously is shown in **Figure 4-1**. First, the Computed Tomography (CT) scan data were used to construct non-uniform rational B-splines (NURBS) CAD surfaces. The sequential DICOM file were loaded into Amira (Konrad-Zuse-Zentrum fur informationstechnik Berlin), a software for visualization and segmentation of three-dimensional (3D) scanned data, through which 3D surface images were obtained from the sequential cross-section outline of the vertebrae at the 1 mm interval. The images were then converted and saved as AutoCAD DXF (Drawing eXchange Format). Next, the generated DXF files, where loaded into 3D scan data processing software RapidForm to perform smoothing operation. The three-dimensional geometrical data were converted into a universal graphics data format (IGES), Ha (2006).

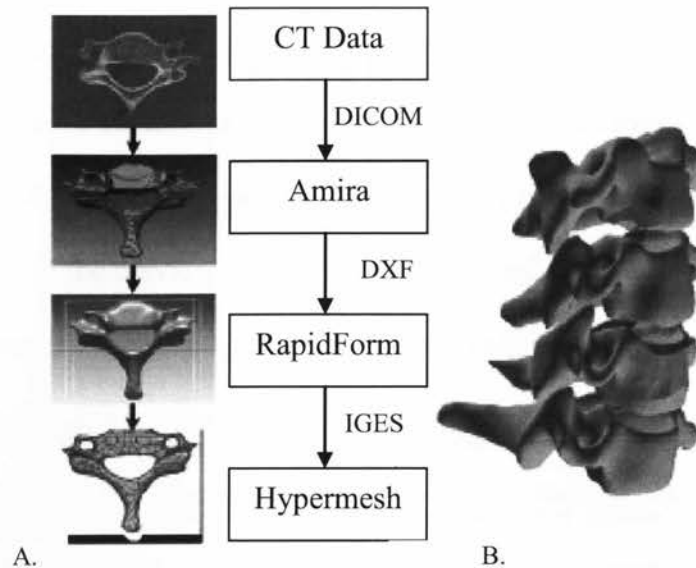


Figure 4-1 : A. Image conversion procedure for FE mesh and B. generated CAD data of C3-C6 vertebrae.

The IGES files were imported into Hypermesh 8.0 finite element analysis software for geometry validation and mesh generation. Altair HyperMesh 8.0 was used because of its high-performance finite element pre-processor. Altair HyperMesh 8.0 generate file format that are used by most popular finite element solvers and allows engineers to analyze product design performance in a highly interactive and visual environment. Also, it has advanced functionality that allows users to efficiently manipulate geometry and mesh highly complex models.

4.1.1 Vertebrae Construction

The C3 to C5 vertebrae were modeled as deformable bodies, consisting of separate elements for cortical bone and cancellous bone since the mechanical properties of cancellous and cortical bone are different. Before mesh generation, the dimensions of each vertebra were measured and compared against experimentally measured values published by Gilad and Nissan (1986, see **Table 2-1**) which is know as 50% percentile

males or mid-sized male. The validation showed that the models were within one standard deviation of experimental data. **Table 4-1** summarizes the dimensions of the vertebral body and the endplate thicknesses.

Table 4-1 : Measured dimensions of vertebral body and endplate.

Vertebral Body		C3 (mm)	C4 (mm)	C5 (mm)
Width	Superior	16.3	17.3	17.8
	Inferior	17.4	16.8	19.5
Depth	Superior	13.9	14.5	14.9
	Inferior	14.6	14.8	15.5
Height	Anterior	14.0	13.6	12.2
	Posterior	13.8	13.8	12.8
Endplate Thickness	Superior	0.63	0.62	0.55
	Inferior	0.58	0.56	0.62

Using the automesh panel ability in Hypermesh, the surfaces of each vertebra was meshed manually using the 2D quadrilateral shell elements. Because of the geometric complexity of the vertebrae and to control the distribution of mesh density at different locations, a mixture of fine mesh (smaller size elements) and a sparse mesh (larger size elements) were used. This was done to ensure the geometry of vertebrae was accurately modeled. While meshing the surfaces, the quality of the elements was checked and poor quality elements were re-meshed. The mesh size was chosen so that the aspect ratio and element distortion of each element was within the acceptable tolerance. The tolerance for aspect ratio was chosen to be .5 or less and distortion ratio was chosen to be .2 as

recommended by Hypermesh. It is imperative to mention that Hypermesh does not generate element that does not meet these two requirements.

To create the cortical bone and bony endplates, the 2D meshed elements (Shell elements) were converted to 3D solid hexagonal elements by offsetting them to an appropriate thickness. Note that the same mesh quality that was explained for shell element was considered for 3D element as well. Meaning, the aspect ratio of .5 and distortion of .2 was maintained for 3D elements.

Even though the thickness of the cortical bone varies depending on each vertebral body and on the location (anterior and posterior), Panjabi *et al.* (2001, see **Table 2-1**), in this study, an average measured anterior and posterior cortical thickness value was used. Therefore, the cortical bone thicknesses of 0.46 mm, 0.48 mm and 0.53 mm were assigned to C3, C4 and C5 vertebrae, respectively. For bony endplates, the superior and inferior elements of the C3-C5 vertebrae body were given thicknesses as measured by Panjabi *et al.* (2001).

In the majority of existing models, the cortical bone and bony endplates were both modeled using 2D quadrilateral shell elements, which were overlaid onto the outer surfaces of the solid cancellous bone elements. The choice of using a shell element rather than a solid element for both the cortical bone and the bony endplate is due to the relatively thin (less than 1 mm) nature of these tissues, to cite a few, Yoganandan *et al.* (1996), Maurel *et al.* (1997), Kumaresan *et al.* (1999), Ha (2006), Basa *et al.* (2006), Lodygowski *et al.* (2005). In their analysis, they modeled the vertebrae components (articular cartilage, endplate, cortical and cancellous bones) as a single phase material. However, in this study, the vertebrae components were modeled as biphasic material

therefore, all the models were developed using the 3D solid hexagonal elements (20 noded). The three-dimensional finite element model of cortical bone and bony end plates of C3 vertebra can be seen in **Figure 4-2**. All cortical bones and endplates were created using two layers of solid elements.

The geometric profile of cancellous bone in the vertebrae was model using the inner elements of the cortical bone. The inner elements of cortical bone were used to create a surface. This surface constituted the outer surface of cancellous bone. Again, using Hypermesh, the surface of the inner elements was meshed as quadrilateral shell elements using larger size elements. The meshed elements were imported into pre-processor MSC.Marc software to convert the shell element to 20 noded hexahedral meshes.

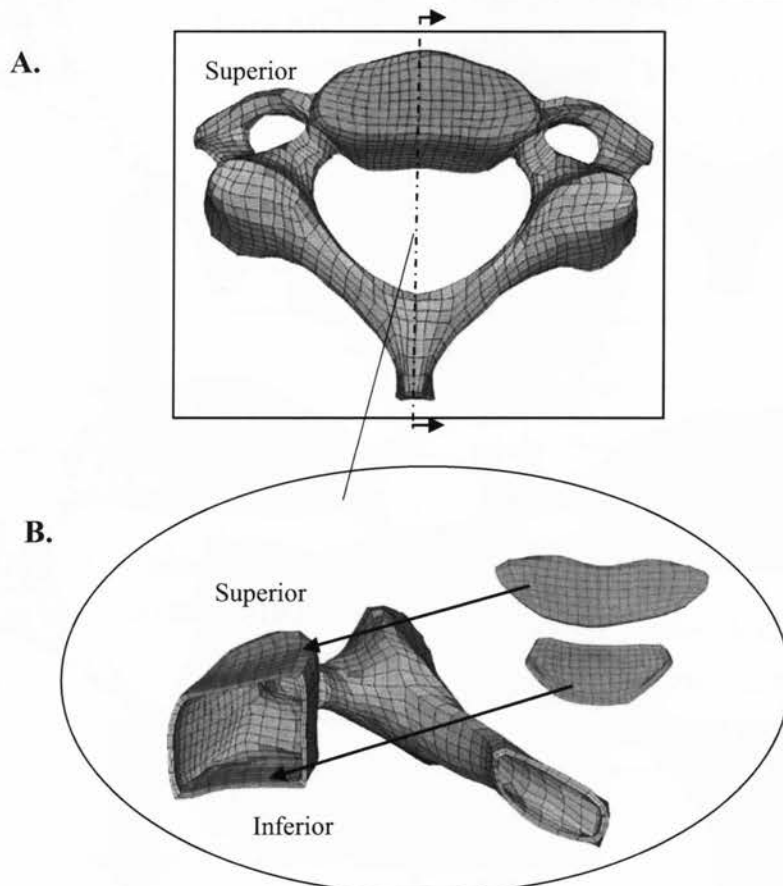
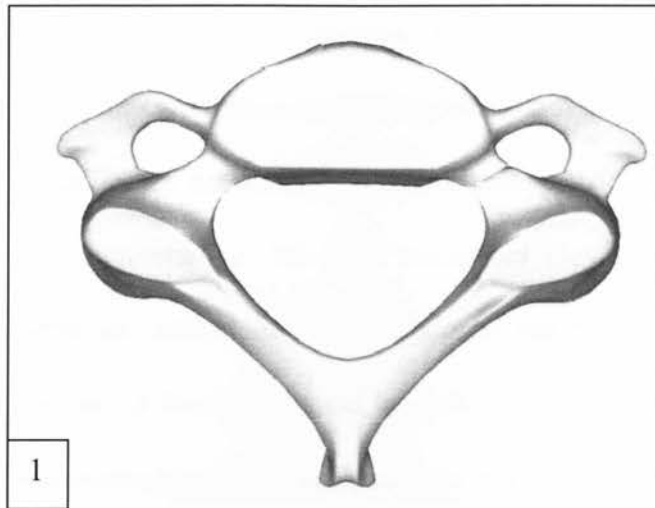
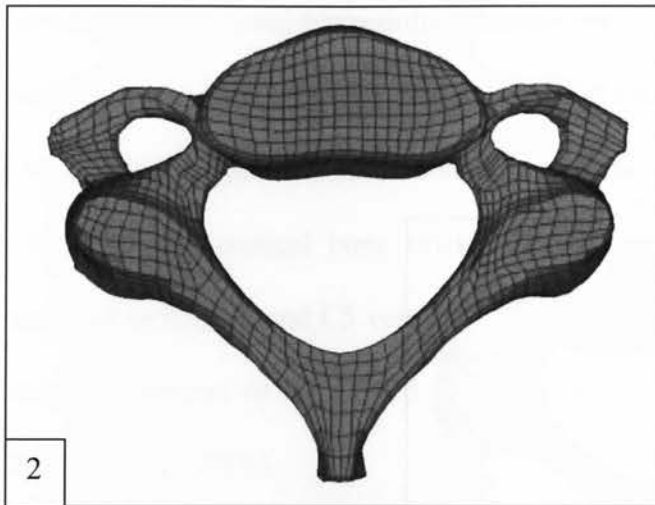


Figure 4-2 : A. Superior view of the C3 vertebra and B. Cross section view of the C3 vertebra showing the superior and inferior endplates.



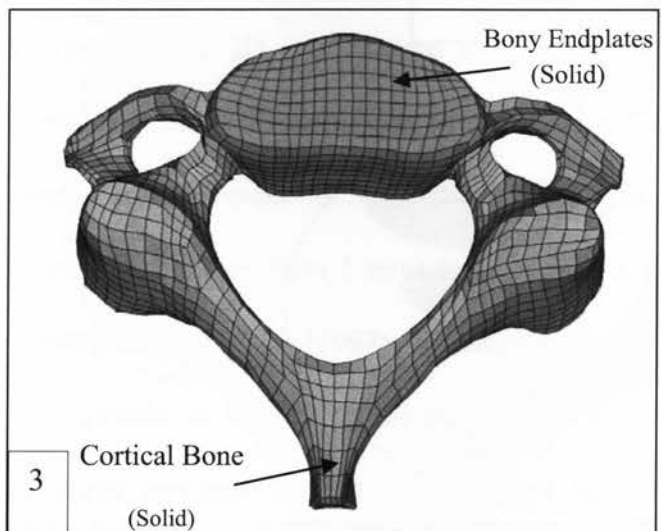
Step 1:

Previously developed surfaces were imported into Hypermesh as an IGES file.



Step 2:

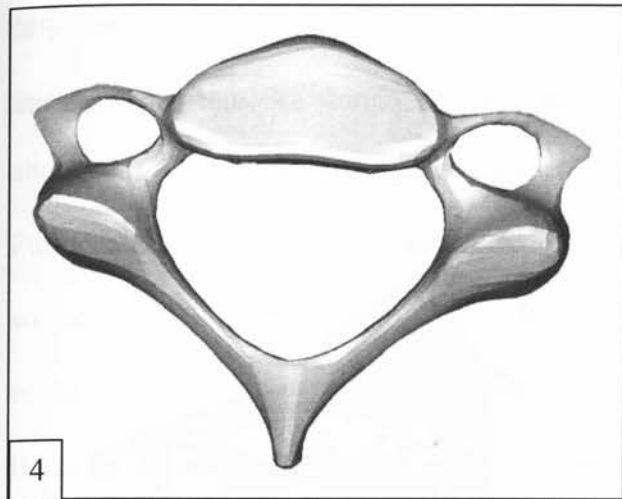
The surfaces were meshed using quadrilateral shell elements.



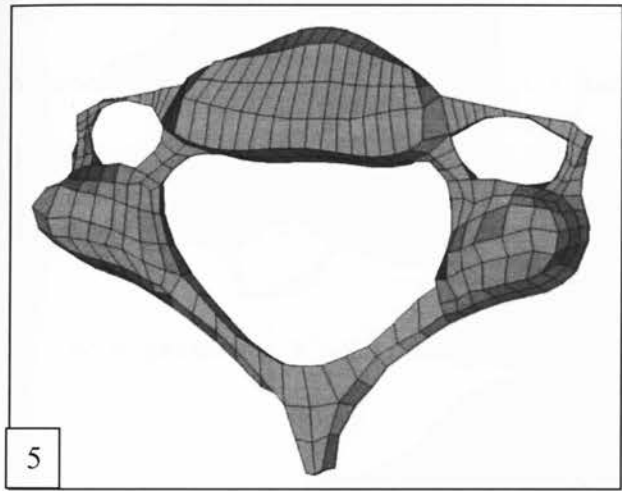
Step 3:

The shell elements converted to solid elements using offset panel.

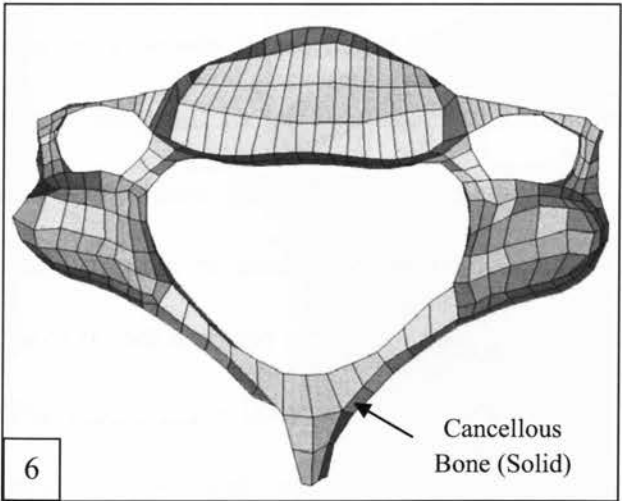




Step 4:
Surfaces were created from the inner elements of cortical bones.



Step 5:
The surfaces meshed using larger sized shell elements.



Step 6:
The shell elements were converted to solid elements using MSC.Marc Software.

Figure 4-3 : The construction of a typical deformable vertebra.

The construction of a typical deformable vertebra can be seen in **Figure 4-3**, while all meshed C3 to C5 vertebrae including cortical bone, endplates, articular cartilages and cancellous bone can be seen in **Figure 4-4**.

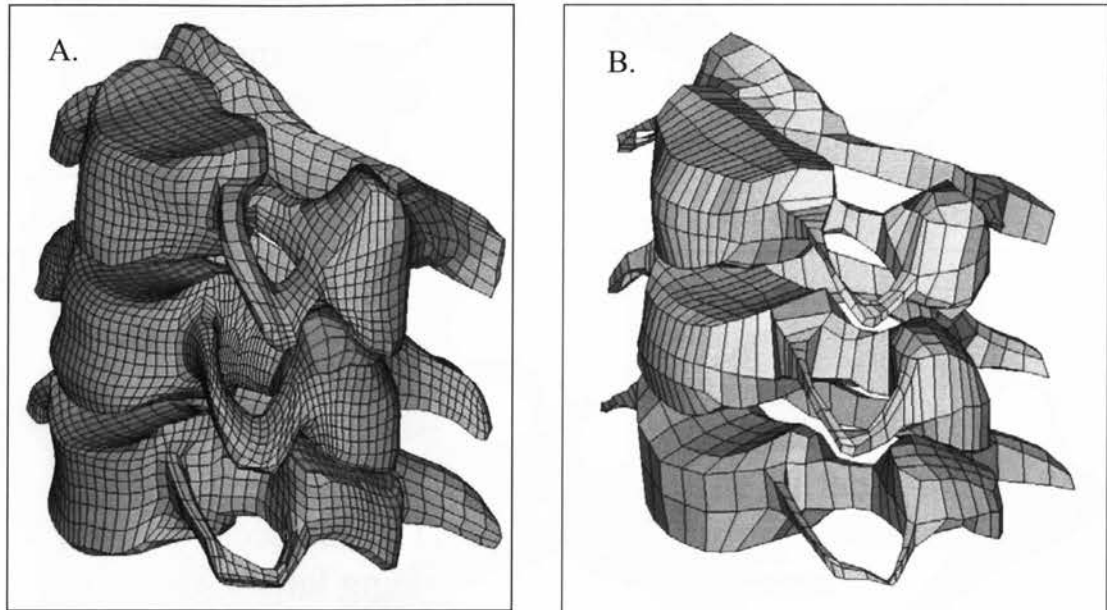


Figure 4-4 : A. The C3-C5 cortical bone and B. The C3-C5 cancellous bone.

4.1.2 Facet Joint Construction

In the FE analysis of spinal segment, modeling of facet joints draws special attentions since they are major sources for nonlinear biomechanical behavior of the spine. Facet joints usually have contact phenomena depending on the loading conditions, and conventional solid elements or gap elements have been often used to simplify their modeling, Yoganandan *et al.* (1996a). In this study, the facet joints between the C3 to C5 vertebrae (vertebrae end processes) were represented in the cervical spine model with solid elements for articular cartilage. The size of the articular cartilages was modeled using Panjab *et al.* (1993) measured dimensions (see **Table 2-2**). The shape of articular

cartilages was dependent on the vertebral geometry. All articular cartilages were created using one layer of solid elements (**Figure 4-5**). The articular cartilage elements were attached to the vertebrae using tied contact to allow for attachment of dissimilar meshes. Furthermore, a finite sliding frictionless contact was defined between articular cartilages so that if there is any contact due to applied load, a penetration between the surfaces could be avoided.

Because of the relative sliding motion between upper and lower articular surfaces of a facet joint during physiological loading, using fluid elements for the synovial fluid between the cartilage can result in highly distorted elements. This can lead to sharply decreasing time step size and numerical instability, Kumaresan *et al.* (1998). Therefore in this study, the synovial fluid was ignored.

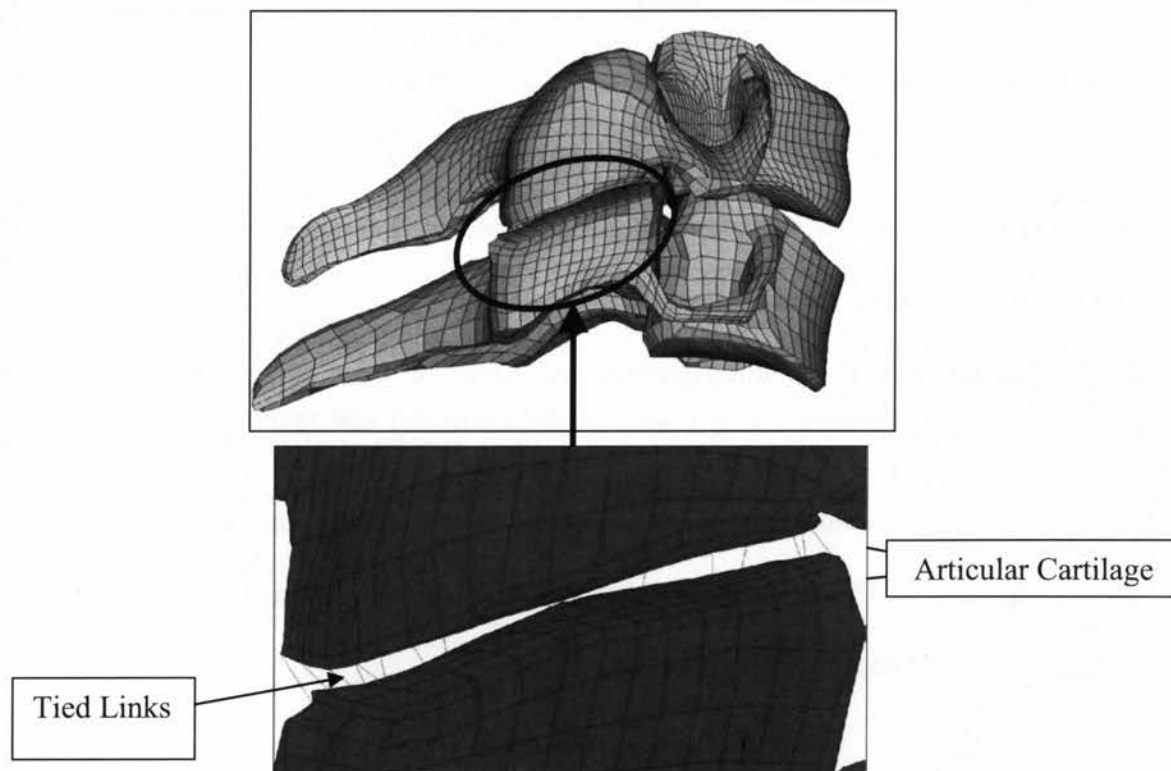


Figure 4-5 : Construction of a Typical Facet Joint

4.2 Intervertebral Disc Construction

The Intervertebral Disc (IVD) was divided into two components: nucleus pulposus and annulus fibrosus. The geometries of the C3-C4 and C4-C5 discs were imported into the Hypermesh 8.0. The anterior and posterior heights of each disc were measured and compared with 50% percentile males of Gilad and Nissan (1986, see **Table 2-4**), and it was found that the dimensions were within one standard deviation of the aforementioned published data. The measured heights of each disc can be seen in **Table 4-2**.

Table 4-2 : Measured heights of intervertebral discs.

Intervertebral Disc		C3-C4 (mm)	C4-C5 (mm)
Height	Anterior	5.1	5.3
	Posterior	3.2	3

The surface of each disc was meshed using quadrilateral shell elements. The elements were exported as Nastran file and were imported into MSC.Marc finite element software. By using the hex mesher module of MSC.Marc, the shell elements of the each disc were converted to 20-noded solid elements.

Cross-sectional area of the intervertebral disc varies between 200 – 400 mm², with the disc having an elliptical shape, Pooni *et al.* (1986). Iatridis *et al.* (1996) reported that the ratio of the nucleus pulposus area to the total intervertebral disc area in healthy human is approximately 1:2. Therefore, half of the disc area were selected and were given nucleus pulposus material properties (see **Figure 4-6**).

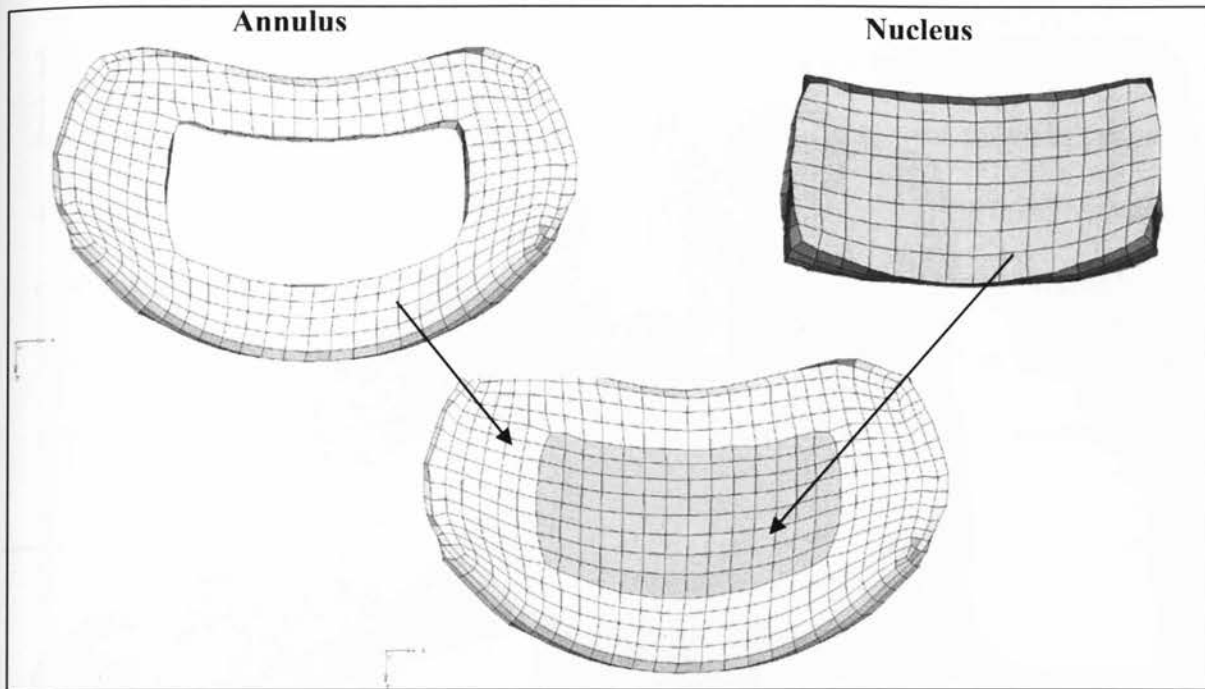


Figure 4-6 : Superior view of the C3-C4 Intervertebral disc

4.3 Ligament Construction

In this study, five major ligaments, the anterior longitudinal ligament (ALL), the posterior longitudinal ligaments (PLL), the ligamentum flavum (LF), the interspinous ligament (ISL), the supraspinous ligament (SSL) were considered, and modeled using 20-noded solid elements. The ligaments were created using one layer of solid elements. The location of each ligament was determined according to anatomical descriptions (**Figure 4-7**). These ligaments were modeled using Yoganandan *et al.* (2000) experimentally measured dimensions (see **Table 2-5**).

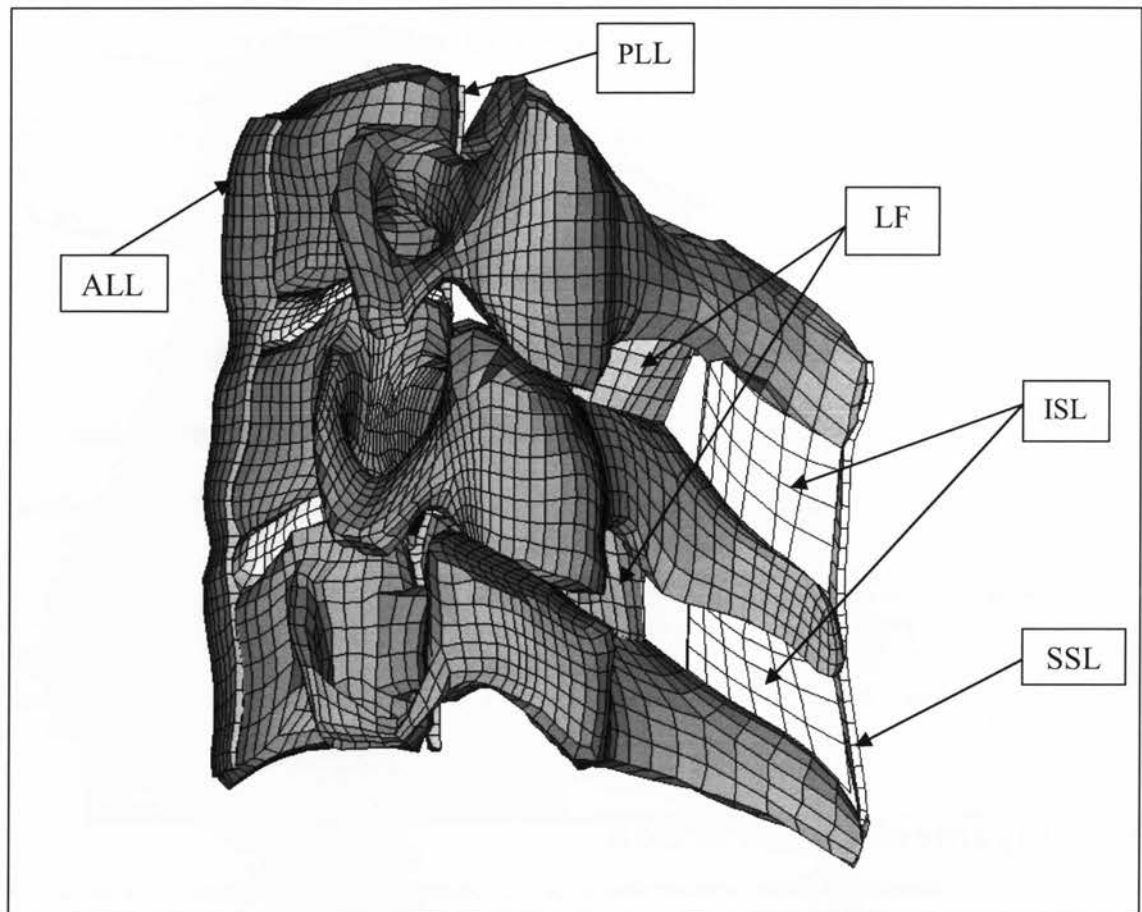


Figure 4-7 : Ligaments in middle cervical spine.

4.4 Spinal Cord Construction

The 2D transverse cross-section of human spinal cord between the C3-C2 vertebrae were modeled using Yu *et al.* (1985, see **Table 2-6**) experimentally measured transverse and anterior-posterior diameters of spinal cord. The 3D mesh was built up by offsetting the transverse elements to a certain height (50 mm). The cross-sectional area of the spinal cord between the C3-C4 and C4-C5 vertebrae were changed as the area changes throughout the length of the cervical spine from C2 to C5 vertebrae.

The grey and white matters of spinal cord tissue were modeled together as a continuous structure since their individual mechanical characteristics are not yet fully understood. The CSF and dura matter were generated in Hypermesh by expanding the outer boundary of the white matter until it touched the ligaments. The outer layer of the spinal cord was given dura matter property and the layers in-between the dura and white matters were given the CSF property. **Figure 4-8** shows the 3D finite element of C2-C5 spinal cord.

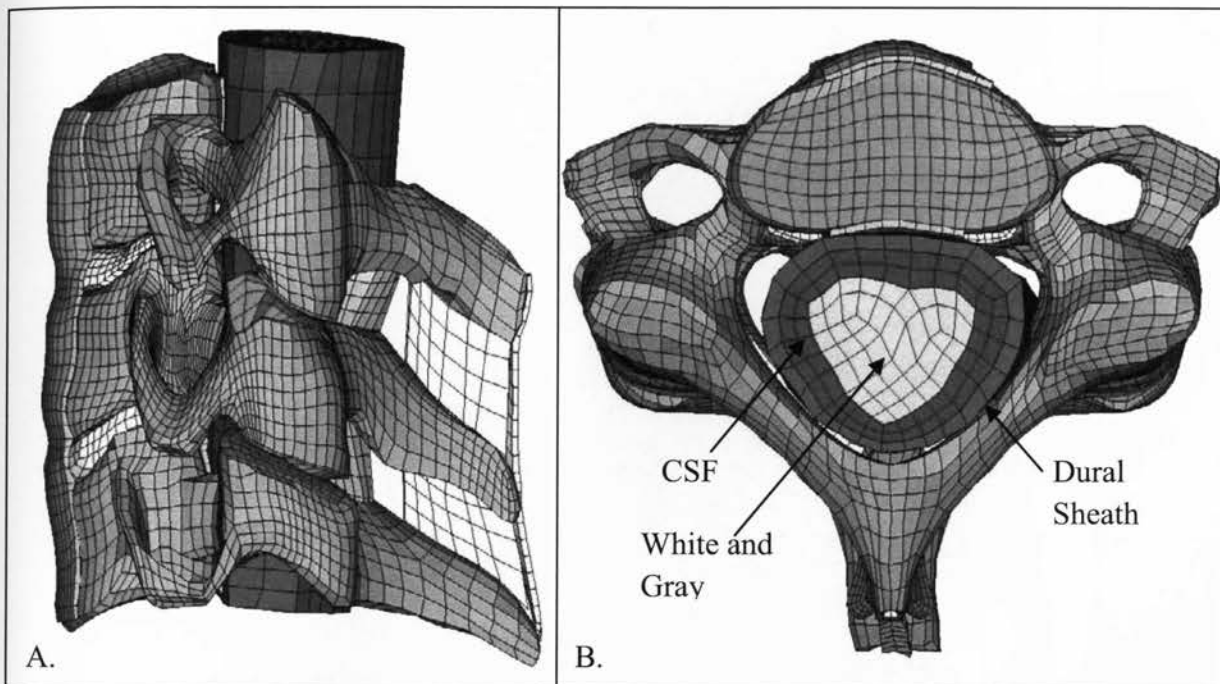


Figure 4-8: A. Side view of C3-C5 vertebrae with the spinal cord. B. Superior view of the C2-C5 spinal cord.

4.5 Full Middle Cervical Model

The detailed three dimensional finite element model of C3-C5 middle cervical spine with spinal cord is shown in **Figure 4-9**. The model includes three vertebrae (includes cortical bone, cancellous bone, boney endplates and facet joints), two intervertebral discs

(includes nucleus pulposus and annulus fibrosus), spinal cord (includes white and gray matter, CSF, and dura matter), and ligaments (includes ALL, PLL, LF, ISL, SSL). Each spinal component was modeled using 20-noded hexagonal elements. The full model has 25060 solid elements and 75456 nodes. An element-breakdown summary of various parts in the cervical spine model can be seen in Table 4-3, 4-4, 4-5 & 4-6.

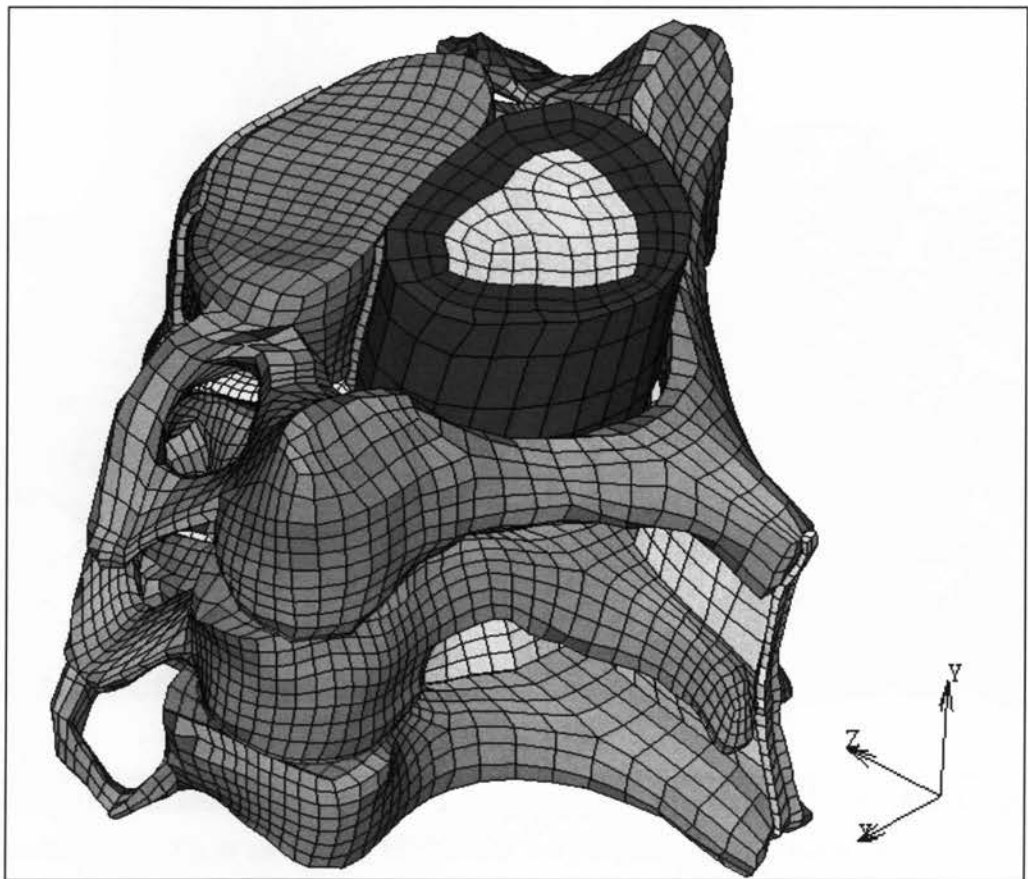


Figure 4-9 : C3-C5 Finite element model.

Table 4-3: Element breakdown summary of vertebrae.

Vertebra	Cortical bone	Cancellous bone	End Plates Superior & Inferior	Articular Cartilages (Superior & Inferior
C3	4484	318	588	126
C4	7243	373	1203	367
C5	4137	250	639	216

Table 4-4: Element breakdown summary of intervertebral disc.

Intervertebral Disc	Annulus Fibrosus	Nuclous Pulposus
C3-C4	896	448
C4-C5	450	250

Table 4-5: Element breakdown summary of ligaments.

Ligaments	PLL	ALL	LF	ISL	SSL
Number of Elments	369	396	162	48	50

Table 4-6: Element breakdown summary of spinal cord.

Spinal Cord	Dural Sheath	CSF	Cord
Number of Elements	494	969	836

Chapter 5

Material Modeling of the Soft Tissues

5.1 Introduction

One of the key components of any accurate FE analysis is the accurate modeling of the material physics. Therefore, the objective of any analysis is to discover a material model that is able to conduct the physical properties of the model. Until now, a number of theories related to soft tissue's mechanical behavior have been developed, and many experimental observations suggested that it would be more realistic to consider biological tissue as a multi-phase system. Therefore, two theories of multi-phase behavior have been proposed to study the soft tissue. They are biphasic theory and poroelastic theory; both theories and their development are reviewed in this chapter. Few finite element models of the cervical spine have used the multi-phase theory. Most of the previous models considered bone and intervertebral disc (soft tissues) as a single phase (solid) material model, (Ng *et al.* (2001), Ha *et al.* (2006), Scifert *et al.* (2002), Kumaresan *et al.* (1999)). Therefore, one of the objectives of this study was to develop finite element model of middle cervical spine based on a linear, isotropic, two-phase material model for the vertebrae and discs.

After choosing an appropriate material model for all components, the next step is to input accurate material properties of the spinal component into the material model. This chapter discusses the method that was used to come up with appropriate properties.

5.2 Biphasic Theory

A finite deformation biphasic theory for intrinsically incompressible mixtures was first formulated by Mow and coworkers (1980), which use the theory of mixtures, as developed by Truesdell and Toupin (1960) and others. In this theory, the tissue is modeled as a two phase immiscible mixture, consisting of an intrinsically incompressible solid phase (collagen and proteoglycan) and an intrinsically incompressible fluid phase (interstitial water). This model has been shown to accurately describe both the stress distribution and interstitial fluid flow within the cartilage tissue under various loading conditions, Armstrong *et al.* (1984). The biphasic theory has been extended to include nonlinear behaviors such as strain dependent permeability (Holmes *et al.* (1985)) and finite deformation (Holmes, 1986). In 1990, Holmes and Mow developed a hyperelastic biphasic theory to describe finite deformation behaviors of articular cartilage. The theory has various strain-energy and strain-dependent permeability functions, and are mathematically valid under various material assumptions and it can describe both the kinematic and equilibrium compressive behaviors of articular cartilage under high strain fields. In this model, the solid phase of cartilage was assumed to be a hyperelastic and isotropic medium. Cohen and coworkers (1997) extended the finite deformation biphasic theory to account for a specific form of tissue anisotropy as well. Also, Spilker *et al.* (1990) proposed a finite element formulation of the linear biphasic model for articular cartilage and other hydrated soft tissues where the fluid phase and solid phase are considered as incompressible.

Recently, the biphasic model has been used for many practical applications in soft tissue biomechanics. These include evaluation of load transmission in normal and pathological joints, evaluation of surgical protocols and development of synthetic tissue replacements. Additionally, applications of biphasic model has been extended to understand mechanics fundamental to joint mechanics such as representation of fluid flow within articular cartilage as a prerequisite for understanding the mechanics of lubrication, friction and wear, Edgard *et al.* (1998).

The background mathematical formulation of biphasic theory is summarized in Appendix A. The mathematical equations were taken from Suh *et al.* (1991), Edgard *et al.* (1998) and Levenston *et al.* (1998) literatures.

5.3 Poroelastic Theory

A poroelasticity theory has been developed and used to solve the viscoelastic behavior of soils. Simon and Wu (1985) were the first to include poroelastic behavior into the finite element modeling of soft tissues in the spinal motion segment. In a poroelastic approach, the disc is modeled as having two distinct phases: a fluid phase and a permeable solid phase. The deformable porous solid and moving pore fluid were modeled using both solid and fluid displacements. The field equations given by Biot (1941) include an overall dynamic equilibrium equation and a generalized Darcy law for the dynamic equilibrium for the fluid motion. Later, Simon (1992) extended this work to large strains. He gave both Eulerian and Lagrangian forms of the governing equations. The model was extended by Laible *et al.* (1993) to include the effects of swelling caused by osmotic pressure such

that load bearing by the fluid phase that may occur even at equilibrium, with corresponding reduction in solid phase support and stresses.

The poroelasticity theory is different from the biphasic theory of mixtures in that the former specifies a continuous distribution of pores in the solid matrix whereas the latter specifies a continuous distribution of solid and fluid phases. Consequently, the poroelasticity theory uses the displacement of the continuum and the average relative fluid displacement as field variables, whereas the biphasic theory uses the solid and absolute fluid displacement as field variables. This difference in the primary unknowns leads to different expressions of the field equations (Prendergast *et al.* (1996)). Given this difference between the biphasic approach used for soft tissues and the poroelastic approach developed for soil mechanics, it has been shown that poroelastic models are equivalent to biphasic models provided that the fluid phase is inviscid (Bowen (1980) and Simon (1992)). Prendergast *et al.* (1996) compared three commercial FEMs (MARC, DIANA, and SWANDYNE) with the model of Spilker *et al.* (1988) for a confined compression test of a biphasic cartilage layer. They concluded that the soil mechanics capability of finite element codes can be used to model biphasic tissues with reasonable accuracy, for both linear and nonlinear cases. Based on their findings, this study uses the soil mechanics capability of MSC.Marc to model biphasic tissues for linear case, given the fluid in this study is assumed inviscid. Hence, the components of vertebrae and intervertebral discs were modeled as a linear isotropic biphasic model, and the ligaments and spinal cord components were modeled as a linear isotropic model. In the biphasic theory, the tissue is modeled as a two phase immiscible mixture, consisting of an

intrinsically incompressible solid phase (collagen and proteoglycan) and an intrinsically incompressible fluid phase (interstitial water).

There are three types of soil analysis available in MSC.Marc. In first type, the analysis calculates the fluid pressure in a porous medium. In such analyses, heat transfer elements are used. In the second type of soil analysis, the pore (fluid) pressure is directly defined, and the structural analysis is performed. For this model, it is important to define an initial (compressive stress) to ensure a stable model. In the third type of soil analysis, a fully coupled approach is used, this type was chosen for this study. The “Herrmann” elements (element type 32, 33, or 35), which are conventionally used for incompressible analyses are available. This study used element type 35 which is a 20-noded and isoparametric element and was used for all spinal components. The porosity ϕ is given in MSC.Marc through the INITIAL POROSITY or the INITIAL VOID RATIO option which in this study initial void ratio $e = \phi/(1-\phi)$ was selected. For a detailed explanation of these three types, the reader is referred to MSC.Marc Manual (Volume A: Theory and user information). The summary of the mathematical formulations that Msc.Marc uses for poroelastic (soil) formulation are presented in Appendix A which is a summary of MSC.Marc Volume A: Theory and user information manual.

5.4 Material Property

Upon choosing an appropriate material model for all components, the next step was to input accurate material properties of the spinal component into the material model. However, material properties of the human cervical spine components reported in the literature vary drastically depending on the approach, method, and specimen preparation

(i.e. Argoubi *et al.* (1996), Wu *et al.* (1996), Lee *et al.* (2000), Loret *et al.* (2004), Simon *et al.* (1985), Ha (2006) and Scifert *et al.* 2002).

In this study, material properties of each component of the cervical model were varied within the range of values reported in the literature. This was done so that an optimum match of the model output was obtained in comparison to the published experimental data under compression. Hence, numerous analyses were performed in an iterative manner so that one specific set of material properties (**Table 5-1, 5-2 & 5-3**) proved to be an optimum matches to the experimental output. It is understood that the biological tissue has inherent variability in mechanical response due to age, physical condition and physiological condition. Thus, the assumption her is that the material taken from published data represent an accurate average data for 25-30 years old male.

As it was mentioned, the components of vertebrae and intervertebral discs were modeled as a biphasic model. Therefore, it was assumed that the fluid was of a single phase. Thus, it was required to define both the soil and fluid properties. For the fluid phase, it was necessary to identify the density of fluid, dynamic Viscosity, fluid bulk modulus and porosity properties. In the majority of the soft tissue studies, the fluid phase was considered to have the same properties as that of water (Simon *et al.* (1985), Lee *et al.* (2000) and Wu *et al.* (1996)). This study used same assumption; the density and dynamic viscosity of the water were used. In addition, the soli (solid) properties were selected from previous literatures such as Argoubi *et al.* (1996), Loret *et al.* (2004), Simon *et al.* (1985) and Ha (2006). **Table 5-1** summarized the properties that were used for vertebrae and intervertebral discs components.

Table 5-1: Material properties of Vertebrae and Intervertebral discs components.

Spinal Components	Soil (Solid) Phase Properties				Fluid Phase Properties			
	Elastic Modulus E (MPa)	Poisson's Ratio ν	Initial Permeability k_0 ($m^4 N^{-1} s^{-1}$)	Density [Kg/m^3]	Density of Fluid [Kg/m^3]	Dynamic Viscosity [N/m^2]	Fluid Bulk Modulus [N/m^2]	Initial Voids ratio e_0
Cortical Bone	10,000 [6]	0.29 [6]	1.0×10^{-20} [1]	1.83×10^3 [3]	1000	2.1×10^9	$2.2 \times 10^{7*}$	0.02 [1]
Cancellous Bone	100 [6]	0.29 [6]	1.0×10^{-13} [1]	$1.12 \times 10^{3\otimes}$	1000	2.1×10^9	$2.2 \times 10^{7*}$	0.40 [1]
Endplate	500 [6]	0.4 [6]	7.0×10^{-15} [1]	1.12×10^3 [4]	1000	2.1×10^9	$2.2 \times 10^{7*}$	4.00 [1]
Articular Cartilage	500 [6]	0.4 [6]	7.0×10^{-15} [1]	1.12×10^3 [4]	1000	2.1×10^9	$2.2 \times 10^{7*}$	4.00 [1]
Annulus Fibrosis (AF)	4.2 [6]	0.45 [6]	3.0×10^{-16} [1]	1.061×10^3 [5]	1000	2.1×10^9	2.2×10^7 [2]	2.33 [1]
Nucleus Pulpous (NP)	1.5 [1]	0.49 [6]	3.0×10^{-16} [1]	1.342×10^3 [5]	1000	2.1×10^9	3.35×10^6 [2]	4.00 [1]
[1] Argoubi <i>et al.</i> , 1996 [2] Wu J.S.S <i>et al.</i> , 1996 [3] Lee C.K <i>et al.</i> , 2000					[4] Loret B <i>et al.</i> , 2004 [5] Simon B.R <i>et al.</i> , 1985 [6] Ha S.K, 2006			
* Assumed to be the same as Annulus Fibrosis value.					⊗ Assumed to be the same as Endplates .			

The ligaments and spinal cord components were modeled using linear isotropic model. The material properties of these components were taken from Ha (2006) and Scifert *et al.* (2002) literature studies and shown as **Table 5-2 & 5-3**. Although the spinal cord components behave as biphasic, the spinal cord was modeled as an elastic model due to lack of property definitions in the literature.

Table 5-2: Material properties of the ligaments.

Ligaments	Posterior Longitudinal Ligament (PLL)	Anterior Longitudinal Ligament (ALL)	Supra-Spinous Ligament (SSL)	Inter-Spinous Ligament (ISL)	Ligamentum Flavum(LF)
Elastic Modulus E (MPa)	20 [6]	54.5 [6]	1.5 [6]	1.5 [6]	1.5 [6]
Poisson's Ratio ν	0.3 [7]	0.3 [7]	0.3 [7]	0.3 [7]	0.3 [7]
[6] Ha S.K, 2006 [7] Scifert J <i>et al.</i> , 2002					

Table 5-3: Material properties of spinal cord.

Spinal Cord	CSF	Dural Sheath	Gray Matter	White Matter
Elastic Modulus E (MPa)	0.001 [7]	31.5 [7]	0.0667 [7]	0.0667 [7]
Poisson's Ratio ν	0.49 [7]	0.45 [7]	0.49 [7]	0.49 [7]
[7]Scifert J <i>et al.</i> , 2002				

Chapter 6

FE Simulation and Results

6.1 Introduction

The next stage of the FE process was analysis. The FE was conducted here to simulate compression, flexion, extension and two lateral bending. These analyses allow the determination of deformations, strains, and stresses which are caused by applied the aforementioned loads. This chapter explains the simulation methods that were used for model validation. Furthermore, the results of the FE analysis are presented and the comparisons of the numerical results with published data are demonstrated.

6.2 FE Simulation Method

In this study, soil formulation implemented in MSC.Marc was adopted under the hypothesis of large deformations. The analyses were implicit, quasi-static and incorporated nonlinear geometry. The finite element model of C3-C5 cervical spine was subjected to an axial compressive load of 600 N centered over superior nodes of C3 vertebrae.

The C3-C5 cervical segment was constrained in all degree of freedom at the C5 inferior vertebral body. For validation, the force-displacement response of middle vertebra was evaluated against the *in vitro* experimental measurements performed by Shea *et al.* (1991). To describe the motion of the vertebra, the position of ten non-collinear points on

the C4 vertebral body was measured from a coordinate system with respect to the fixed reference C5 vertebra. Then, the average of these ten points was considered as the vertebra displacement. **Figure 6-1** shows the superior and inferior locations of the ten points that were used. The ten points averaging method was used for vertebrae rotation measurements. Furthermore, the lateral disc bulge at its mid-height under axial compressive load at anterior and posterior locations of the C4-C5 intervertebral disc was obtained and compared against the linear finite-element model developed by Ng *et al.* (2001).

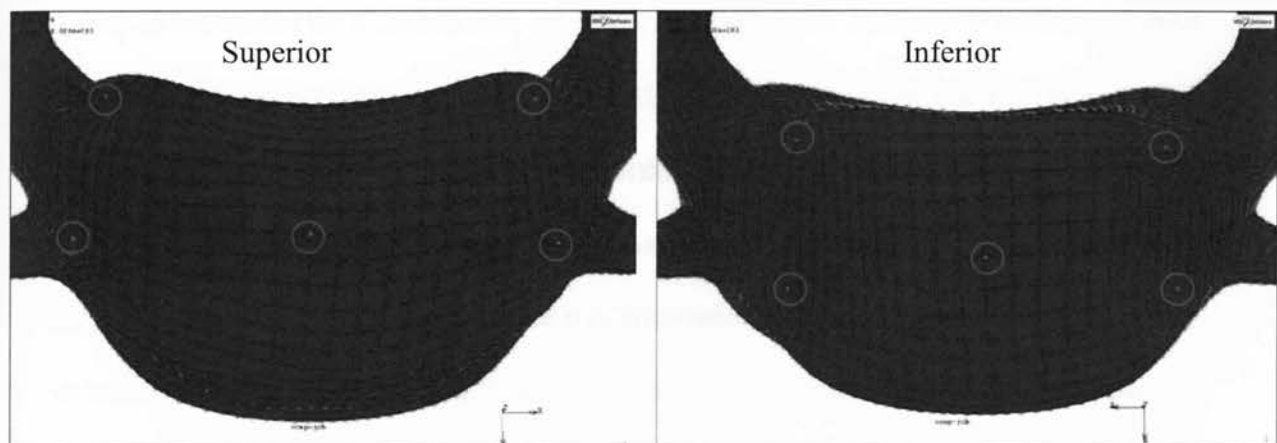


Figure 6-1: The position of ten non-collinear points on the C4 vertebra.

The FE model of C3-C5 was also used to predict the flexion, extension and lateral bending motions. Therefore, for all boundary conditions except compression the following pure moments of 0.33, 0.5, 1.0, 1.5 and 2.0 Nm were applied to the superior end of the C3 vertebra, while the inferior nodes of C5 were constrained in all directions. These values are within the elastic range for cervical spine pure moment testing. The response of the vertebrae to these pure moments was evaluated in the sagittal plane. The resulting external angle response curves were obtained and compared against the

experimental data of Wheeldon *et al.* (2006 and 2008). Furthermore, the lateral disc bulge of each loading modes was computed.

The aforementioned analyses for all loading conditions were repeated by incorporating the spinal cord into the model. To do so, the inferior nodes of the spinal cord were fully constrained, while the top of the cord was left unconstrained. The results of these analyses were compared against the previous analyses (model without spinal cord) and the results are presented in the next section of this chapter.

The current FE model has different deformable parts and each of these parts has contact with one other. Therefore, to perform an accurate simulation, it is necessary to define right contact areas and conditions. For this purpose, contact table option in MSC.Marc was used. A contact table is a set of entries which specifies the relationship between contact bodies in a contact analysis. It indicates which set of bodies may or may not touch each other, so that computational time can be saved. It defines different properties per set of contact bodies, like friction coefficient, error tolerance and separation force. In addition, it can be used to activate glued contact, which can be effectively used to couple separately meshed parts of a structure.

A very powerful analysis capability in MSC.Marc program is the automatic contact analysis. The boundary nodes and segments for a given set of elements will be determined and when the analysis requires it, automatically the boundary conditions to be applied will be adapted. When two bodies come in contact, Marc automatically determines the area of contact and calculates the contact normal and friction stresses. Marc Mentat supports this analysis capability completely. This study used this ability (contact automatic algorithm) to describe contact between the soft tissue parts. The

definition of the various contact bodies is shown in **Figure 6-2**. Also, **Table 6-1** summarizes the list of defined contacts between the bodies.

First general boundary condition is the contact between endplate and disc (AF and NP). As explained earlier, there is a loose connection between endplates and discs such that virtually the disc moves freely within the endplates space. After extensive literature review, it was found that there is extremely limited information available regarding the physiological contact properties between disc and vertebral body. To this end, a recursive FE method was conducted to determine the contact properties.

The following briefly explains the recursive method used in this work. Two contact surfaces were defined; one for the outer surface of the disc and second for the outer surface of the endplates and they were connected to each other using MSC.Marc Touch contact option. To determine the coefficient of friction value for two touching bodies, several axial compression analyses were performed with different values for coefficient values (e.g. 0.001, 0.005, 0.01, 0.05, 0.1, and 0.2). For each analysis, the lateral disc bulging of C4-C5 disc was obtained and compared against the linear finite-element model developed by Ng *et al.* (2001). It was found that coefficient frictions of 0.001 and 0.005 give less bulging compared to Ng *et al.* (2001) result, while coefficient frictions of 0.05, 0.1 and 0.2 give more bulging (disc slip out). Finally, the coefficient frictions of 0.01 resulted in a comparable amount of bulging to that of Ng *et al.* (2001). Therefore, to represent the real life condition closely, Coulomb frictional contact with coefficient of friction of 0.01 was chosen for the contacting surfaces. The rest of the deformable tissue parts were connected to each other using MSC.Marc Glue contact option with the exception of the articular cartilages. As it was mentioned previously, a finite sliding

frictionless contact was defined between articular cartilages so that if there is any contact due to applied load, a penetration between the surfaces could be avoided therefore, frictionless Touch contact option was used.

In addition, the second general boundary condition is the contact between spinal cord and the cervical spine components. The spinal cord by itself has different components such as white and gray matter, dural sheath and CSF. Therefore, these components were connected to each other by sharing their nodes. To connect the spinal cord aggregate to the cervical spine, two surface contacts were defined; one for outer surface of dural sheath and second for outer surfaces of the spinal canal and posterior aspect of the discs and ligaments. In order to represent the real life condition, these two contact surfaces were glued to each other.

Table 6-1: List of defined contacts between the bodies.

Components	Type of Contact	Contacting Body
Cancellous	Glued	Cortical
Cortical	Glued	End plates, Cancellous, Articular Cartilage, ALL, PLL, LF, ISL,SSL, Spinal cord
End Plate	Touched	AF, NP
End Plate	Glued	Cortical
Annulus Fibrosus (AF)	Touched	End Plate
Annulus Fibrosus (AF)	Glued	NP
Nucleus Pulpous (NP)	Touched	End Plate
Nucleus Pulpous (NP)	Glued	AF
Articular Cartilage	Touched	Articular Cartilage
Articular Cartilage	Glued	Cortical
PLL, ALL, LF, ISL,SSL	Glued	Cortical
Spinal Cord	Glued	PLL, LF, Cortical

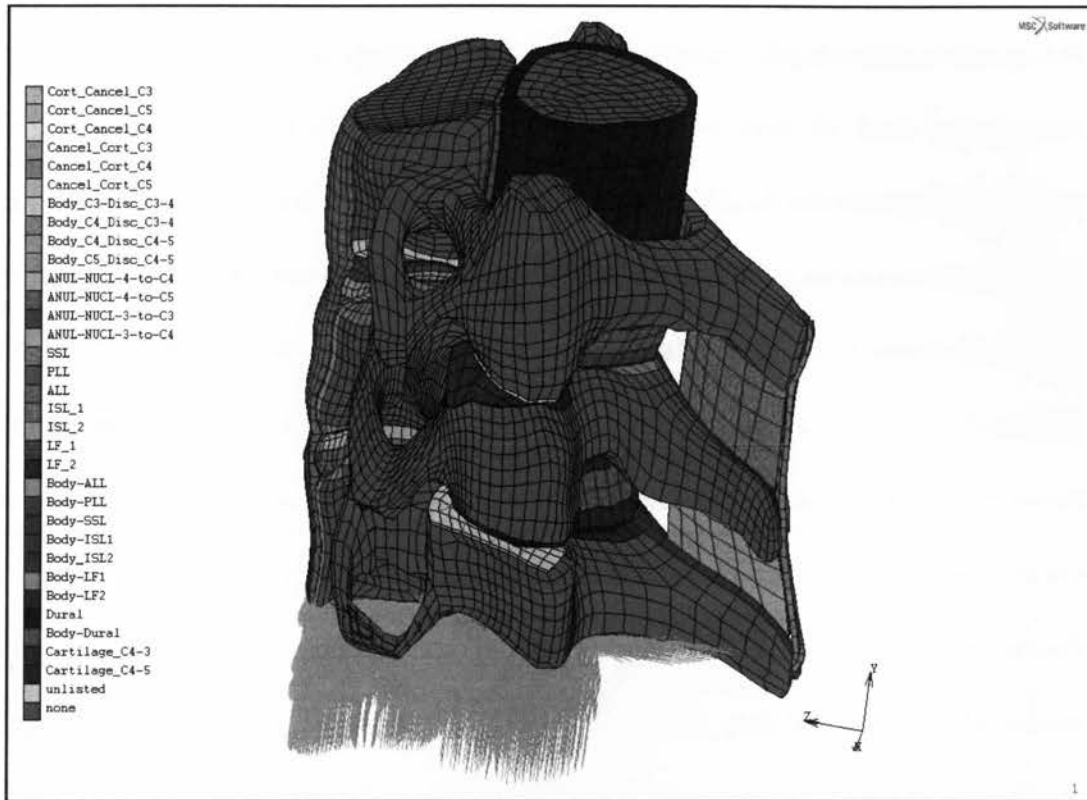


Figure 6-2 : Contact body definition of middle cervical spine.

6.3 Simulation Results

To ensure that the process of modeling and assigning material properties to various components of the cervical spine were accurate and suitable, the FE model of C3-C5 cervical spine was validated against the results reported in the literature. A reasonable agreement between the simulation results and published data was considered as the validation of the model. Once the model was validated, further analyses were performed. A literature review showed that most researchers refer to Shea *et al.* (1991) and Wheeldon *et al.* (2006 and 2008) for the comparison of their results. In this work, all results were compared against *in vitro* results of Shea *et al.* (1991) and Wheeldon *et al.* (2006 and 2008).

The force versus displacement curve of C4 vertebra as a result of 600N applied compressive load is shown as **Figure 6-3**. Moreover, **Figure 6-4** shows the Y displacement (axial displacement) contour plots of C4 vertebra. As it can be seen, the C4 vertebra was compressed by an average of 0.82mm at 600 N axial compressive loads. The result showed that there is an average of 4% discrepancy between this analysis and published experimental data presented by Shea *et al.* (1991). Note that the **Figure 6-3** shows the displacement as positive. It is only shown as positive for the purpose of illustration and the actual displacements are compressive. Generally, the force-displacement response of the current model corresponds reasonably well with the published experimental data Shea *et al.* (1991). Furthermore, the lateral disc bulge at its mid-height under axial compressive load at anterior and posterior locations of the C4-C5 intervertebral disc was obtained and compared against the linear finite-element model developed by Ng *et al.* (2001).

Figure 6-5 shows the predicted variation of the lateral disc bulge at posterior and anterior locations of C4-C5 disc. The result showed that there is an average of 17% (anterior) and 35% (posterior) discrepancy between this analysis and Ng *et al.* (2001) analysis.

It was explained that recursive method was used to determine the contact properties. Since Ng *et al.* (2001) used linear isotropic material properties, the same linear material properties were used to determine the contact properties. Once this was achieved, the biphasic linear material properties were incorporated into the model and all analysis for this study were conducted using biphasic materials. Nonetheless, the maximum bulge occurs at the anterior location of the C4-C5 disc which this is in agreement with their observation. At anterior and posterior locations, the maximum value of disc bulge was

found to be 0.57 mm and -0.44 mm, respectively. Note that the positive and negative values for displacements indicate that the disc bulges outward for both anterior and posterior locations. **Figure 6-6** shows the contour plots of C4-C5 lateral disc bulge which in this study the Z displacement demonstrates the lateral bulging. In this study, only the results of C4-C5 disc are shown, and the C3-C4 disc results have not been considered due to having direct contact with load.

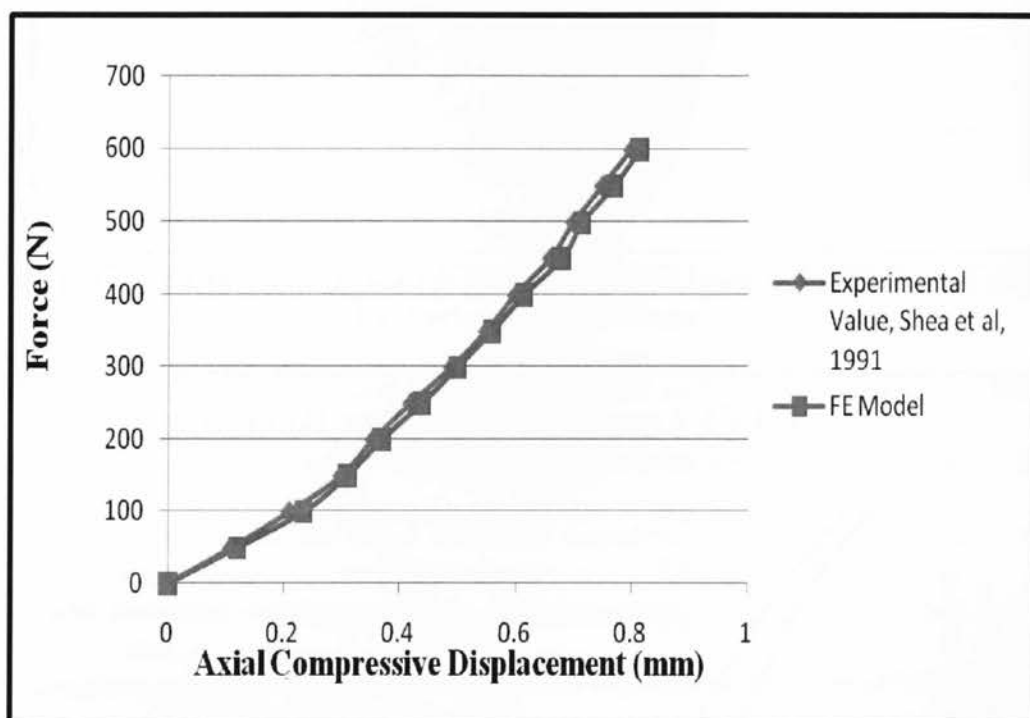


Figure 6-3 : Comparison of the force-displacement response between present and the Shea *et al.* (1991) results.

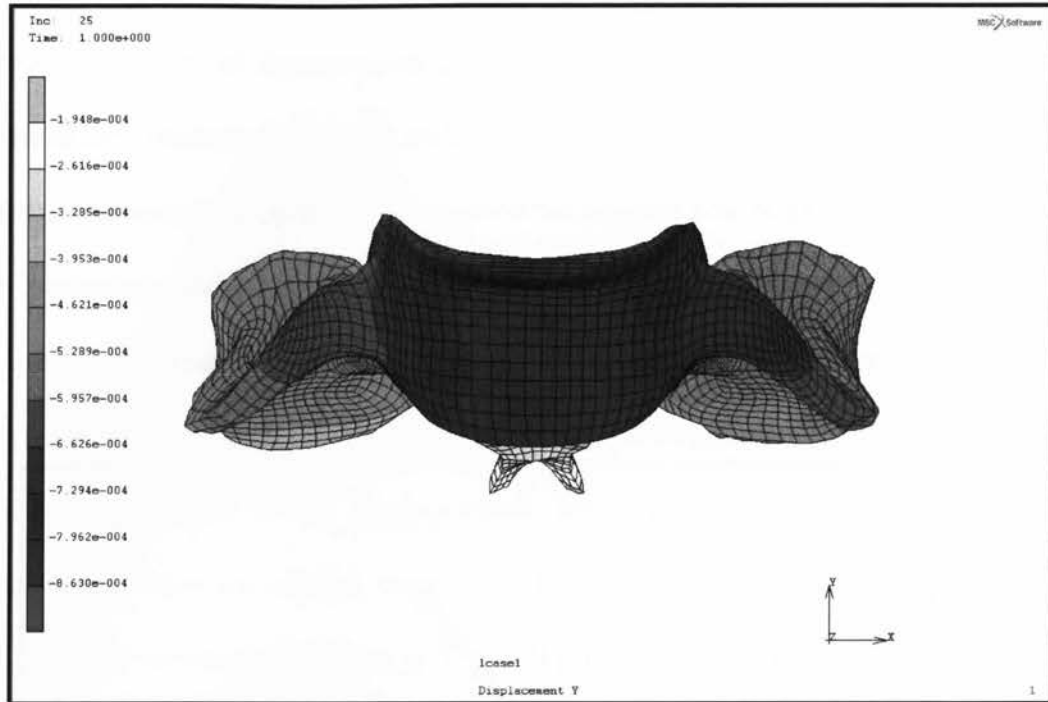


Figure 6-4 : Y-Displacement counter plots of the C4 vertebra as a result of 600 N applied compressive load.

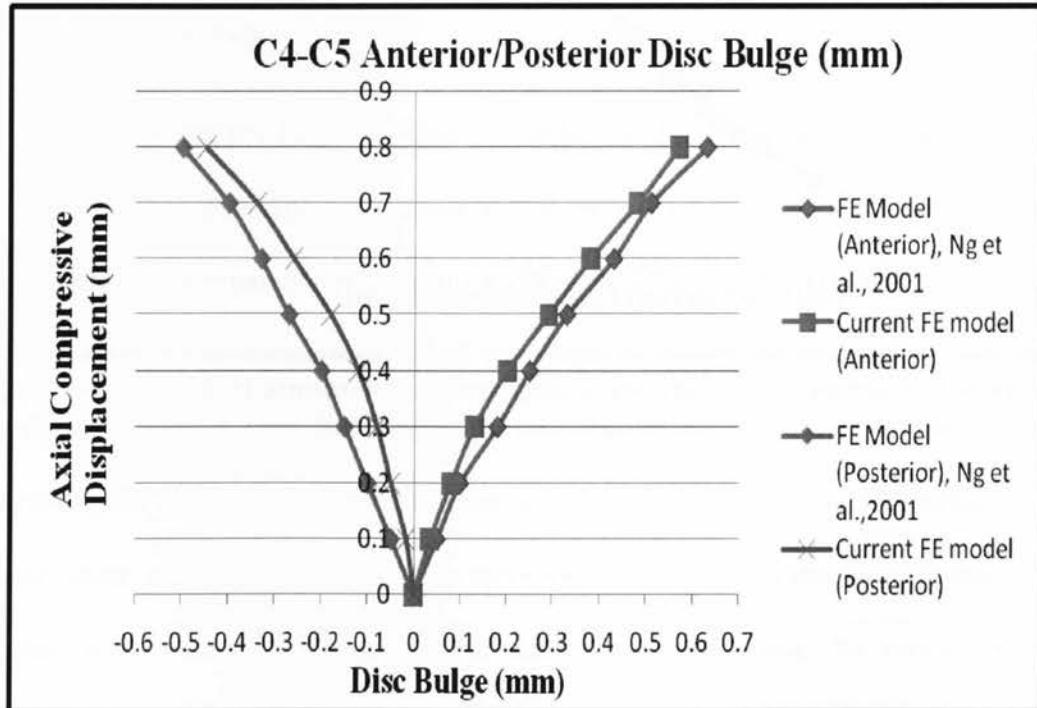


Figure 6-5 : Comparison of the lateral C4-C5 anterior and posterior disc bulge between the present and Ng *et al.* (2001) results.

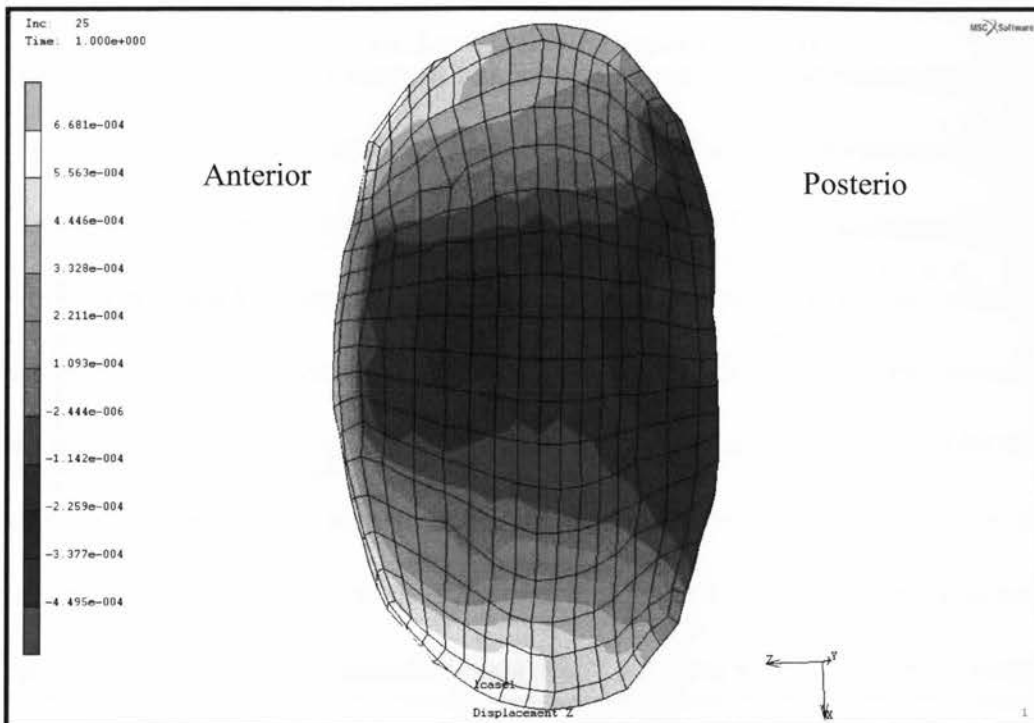


Figure 6-6 : Z-Displacement (lateral bulging) counter plots of C4-C5 intervertebral disc.

Validation of the model in flexion and extension was particularly important, since these are the primary modes of spinal loading. These motions are most often studied for the cervical spine, and have the most available experimental data for validation. Under flexion and extension bending moments, the biomechanical responses of the C3-C4 and C4-C5 segment results corresponded well within experimental results of Wheeldon *et al.* (2006) (**Figure 6-7** and **Figure 6-8**). In flexion, the acceptable ranges (experimental range) of rotation at 2 Nm moments for C3-C4 and C4-C5 segments are 4.7 to 12 and 5.2 to 11 degrees, respectively. In this study, the maximum rotation degree at 2 Nm moments for C3-C4 and C4-C5 vertebrae was found to be 6.7 and 5.5 degrees respectively which fall within the experimental range. In extension, the acceptable range of rotation for both C3-C4 and C4-C5 vertebrae are 3.5 to 6 degree. Current result showed that the maximum

degree of rotation for C3-C4 is 5.7 degree and for C4-C5 vertebra is 4.8 degree which fall within the experimental range. Note negative and positive in **Figure 6-7** and **Figure 6-8** indicate the extension and flexion response. In addition to flexion/extension, right and left lateral bending moments were applied to the model and the results showed that they were within one standard deviation of the experimental results (**Figure 6-9**). Since the experimental results of lateral bending of C3-C4 segment were not available in Wheeldon et al (2008) research, this study has only shown the C4-C5 lateral bending results. For C4-C5 segment, the maximum experimental ranges of rotation at 2 Nm during right and left lateral bending are 2.7 to 6 and 2 to 6 degrees, respectively. This study has shown the maximum rotation of 4 degree for right and 3 degree for left lateral bending that correspond to experimental data. Note that negative and positive in **Figure 6-9** indicate the left and right response, respectively.

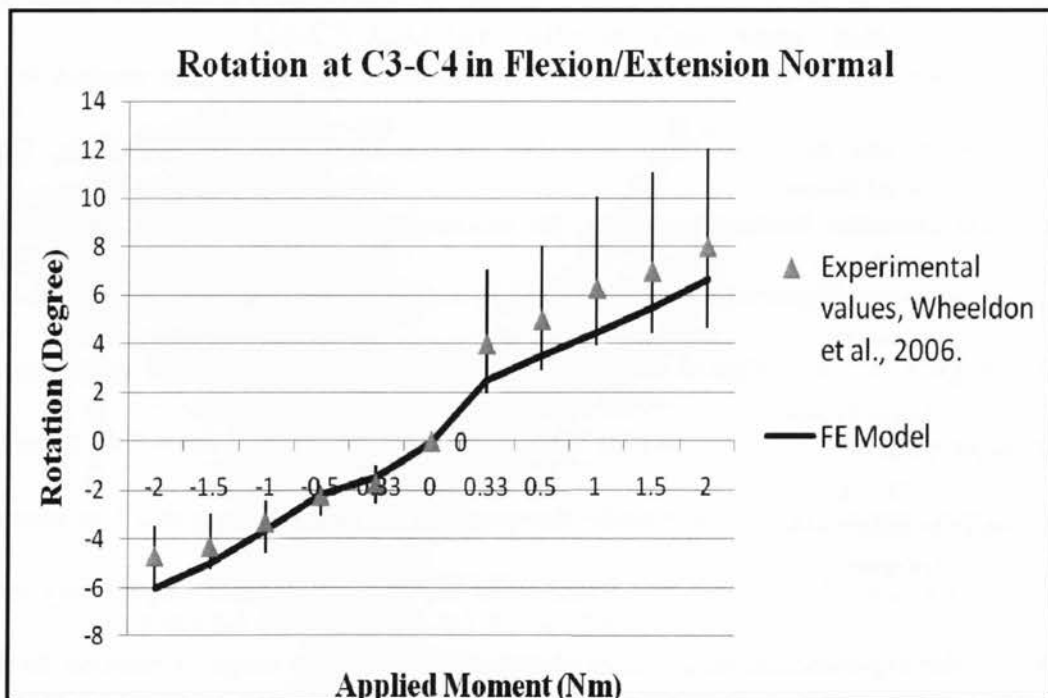


Figure 6-7 : Comparison of the C3-C4 moment-rotation relationship between current results and Wheeldon *et al.* (2006) results.

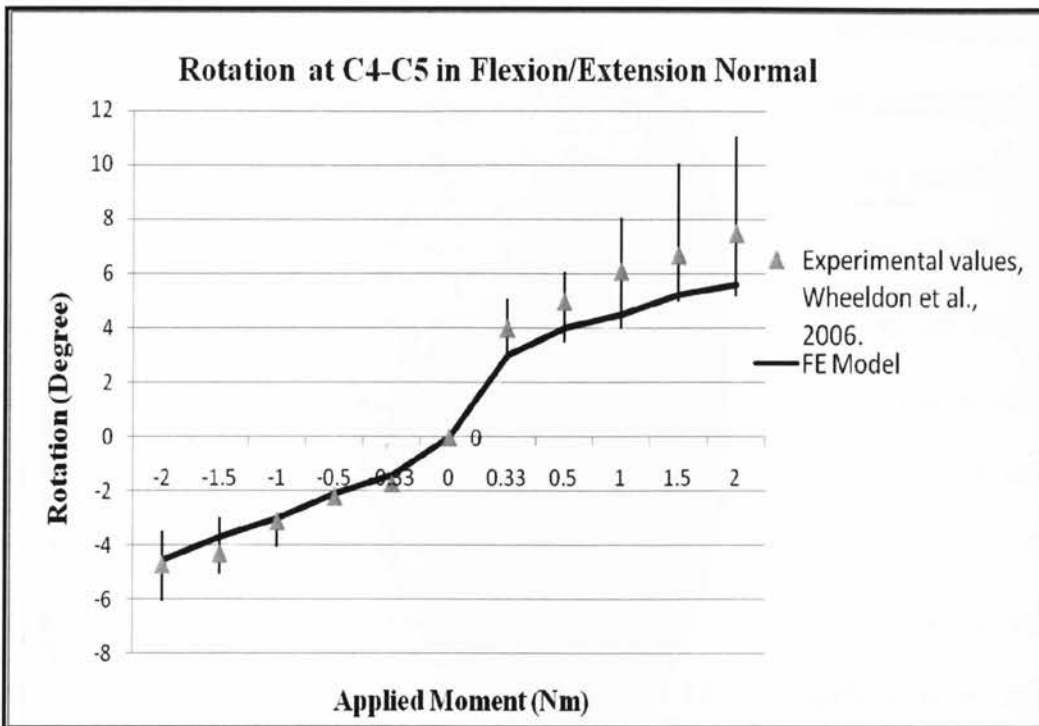


Figure 6-8 : Comparison of the C4-C5 moment-rotation relationship between current results and Wheeldon *et al.* (2006) results.

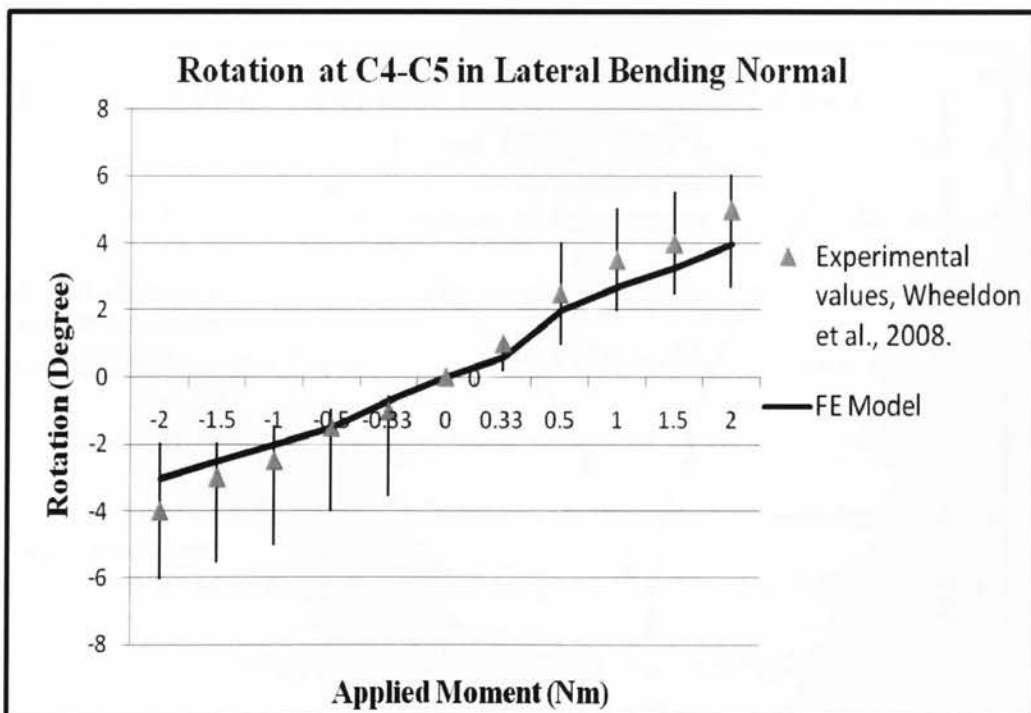


Figure 6-9 : Comparison of the C4-C5 moment-rotation relationship between current results and Wheeldon *et al.* (2008) results.

The responses of the current FE model of cervical spine were validated at compression, flexion, extension and lateral bending. Therefore, this model was used for further analysis and that was to consider spinal cord response into the model.

The FE model with spinal cord was subjected to pure axial compressive load of 600 N applied to the upper bony endplate (cartilaginous end plate) section of the C3 vertebra.

The disc bulge of the C4-C5 disc was determined for both anterior and posterior locations (Figure 6-10). The results were compared with the previous analysis (FE model without spinal cord). In compression, it was found that the axial displacement (Y-direction in the model) of C4 vertebra was reduced by 0.06 mm. Therefore, this reduced the lateral disc bulging by an average of 0.03 mm at the anterior and by 0.07 mm at the posterior locations. Figure 6-11 shows the Z displacement contour plots of C4-C5 intervertebral disc.

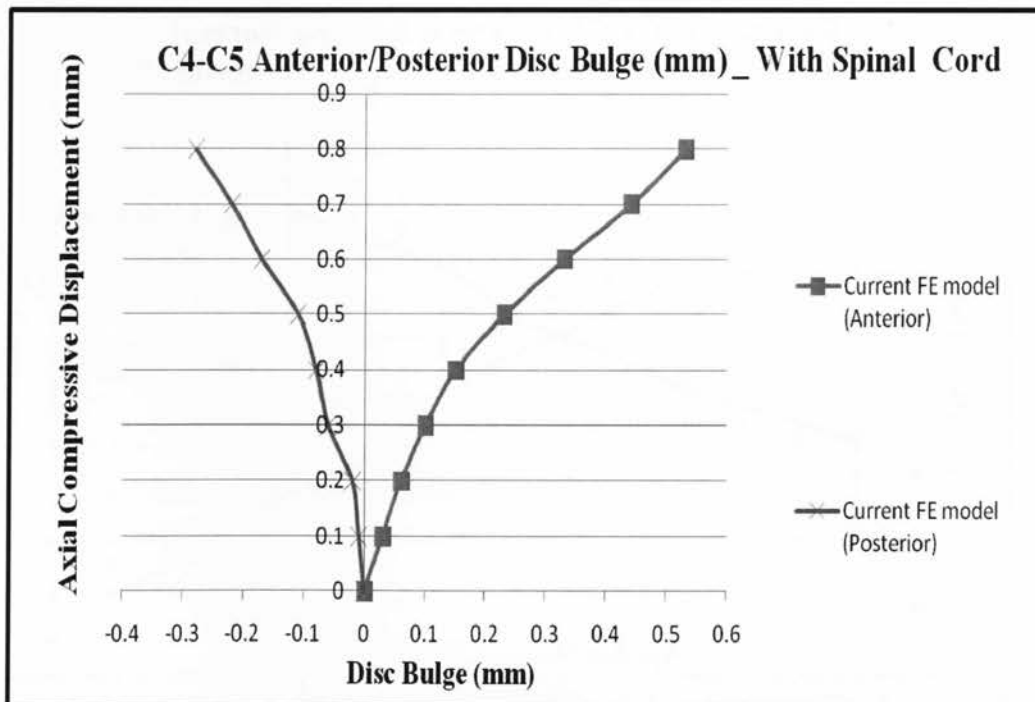


Figure 6-10 : Predicted variation of the lateral disc bulge with axial compressive load for the finite element model with spinal cord.

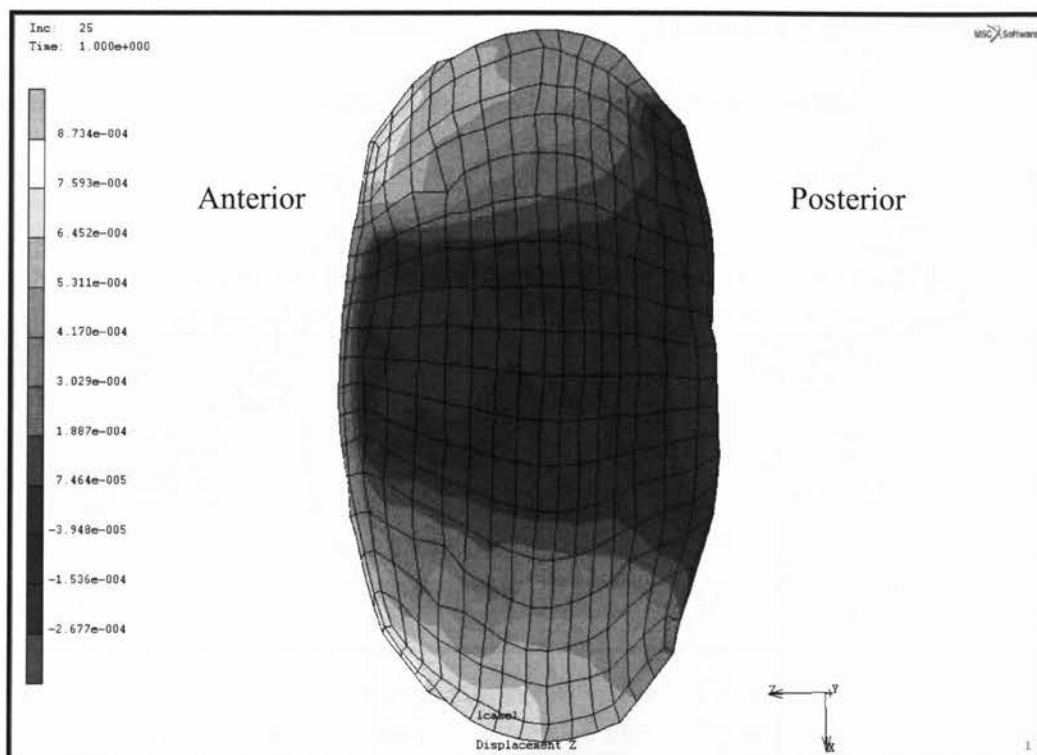


Figure 6-11 : Z-Displacement (lateral bulging) counter plots of C4-C5 intervertebral disc.

Under flexion and extension bending moments, the median, minimum and maximum values of C4-C5 disc bulge of the two models (with and without spinal cord) were summarized in **Table 6-2**. A comparison of these results indicates that removal of the spinal cord alters the pattern of the relative variation of the disc bulge magnitude around the outer layer of annulus fibrosis. It was found that during the flexion and extension, the model with spinal cord gave less disc bulge compared to the model without spinal cord. In flexion, the model with spinal cord reduced the degree of rotation by an average of 0.5 degree. This resulted in reduction of disc bulge of 0.06 mm and 0.03 mm at the anterior and the posterior respectively. Equally, in extension the rotational degree was reduced by an average of 0.8 degree. Similarly, for extension, the amounts of disc bulge for anterior and posterior locations were reduced by 0.11 and 0.13 respectively. The **Figure 6-12**

shows the comparison between the two models for both flexion and extension modes. The contour plots of extension/flexion analyses (with spinal cord model) are shown in Appendix B.

Table 6-2 : Median, Maximum and minimum values in millimeters of disc bulging data evaluated for anterior and posterior locations.

Loading Direction	Location	Without Spinal Cord			With Spinal Cord		
		Median	Max	Min	Median	Max	Min
Flexion	Anterior	0.79	0.93	0.55	0.73	0.9	0.51
	Posterior	0.28	0.36	0.12	0.25	0.34	0.11
Extension	Anterior	-0.62	-0.67	-0.56	-0.51	-0.55	-0.33
	Posterior	-0.45	-0.52	-0.37	-0.32	-0.38	-0.16

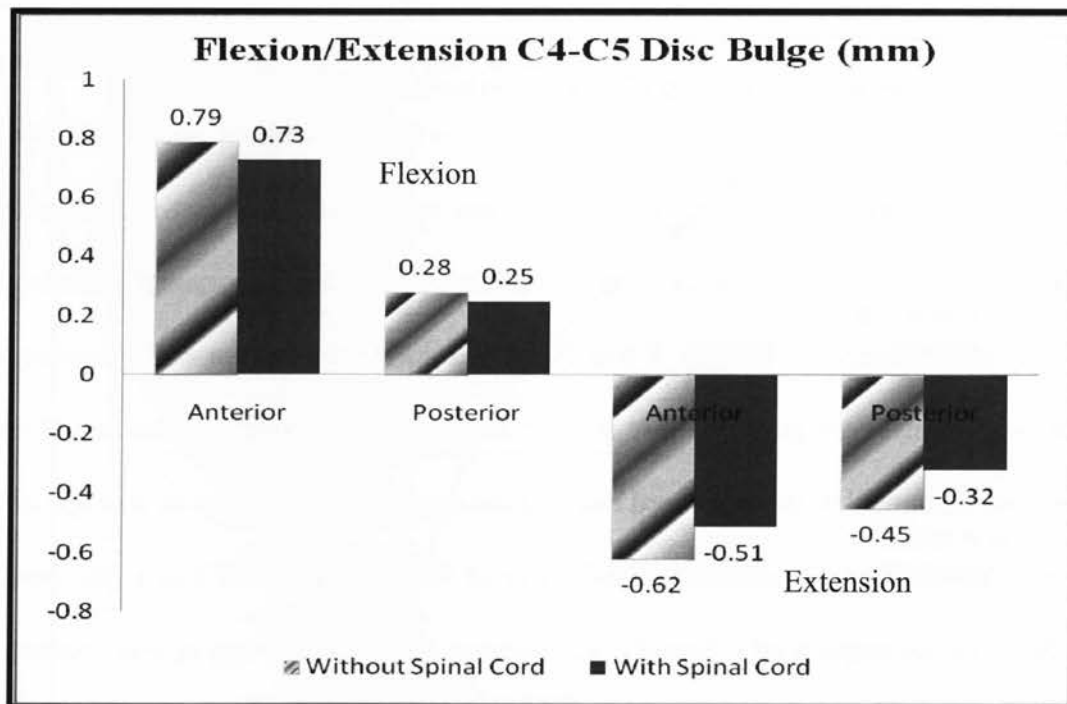


Figure 6-12 : Comparison of the C4-C5 disc bulge between model with and without spinal cord.

Table 6-3 summarizes the amount of right and left hand sides of C4-C5 disc bulge of two models during both left and right lateral bending moments. As it can be seen in **Figure 6-13**, presence of the spinal cord in the FE model resulted in lower bulging for both left and right lateral bending modes. In right and left lateral bending (the model with spinal cord) the degree of rotation was reduced by an average of 0.3 and 0.2 degree. These translate to 0.07 mm and 0.03 mm on the left and right hand side in right lateral bending 0.02 mm and 0.02 mm on the left and right hand side in left lateral bending. The contour plots of right/left lateral bending analyses (with spinal cord model) are shown in Appendix B.

Table 6-3 : Median, Maximum and minimum values in millimeters of disc bulging data evaluated for anterior and posterior locations.

Loading Direction	Location	Without Spinal Cord			With Spinal Cord		
		Median	Max	Min	Median	Max	Min
Right Lateral Bending	Left	-0.32	-0.52	-0.13	-0.25	-0.34	-0.10
	Right	0.61	0.80	0.43	0.58	0.71	0.36
Left Lateral Bending	Left	0.34	0.46	0.22	0.32	0.45	0.2
	Right	-0.1	-0.20	-0.02	-0.08	-0.15	-0.01

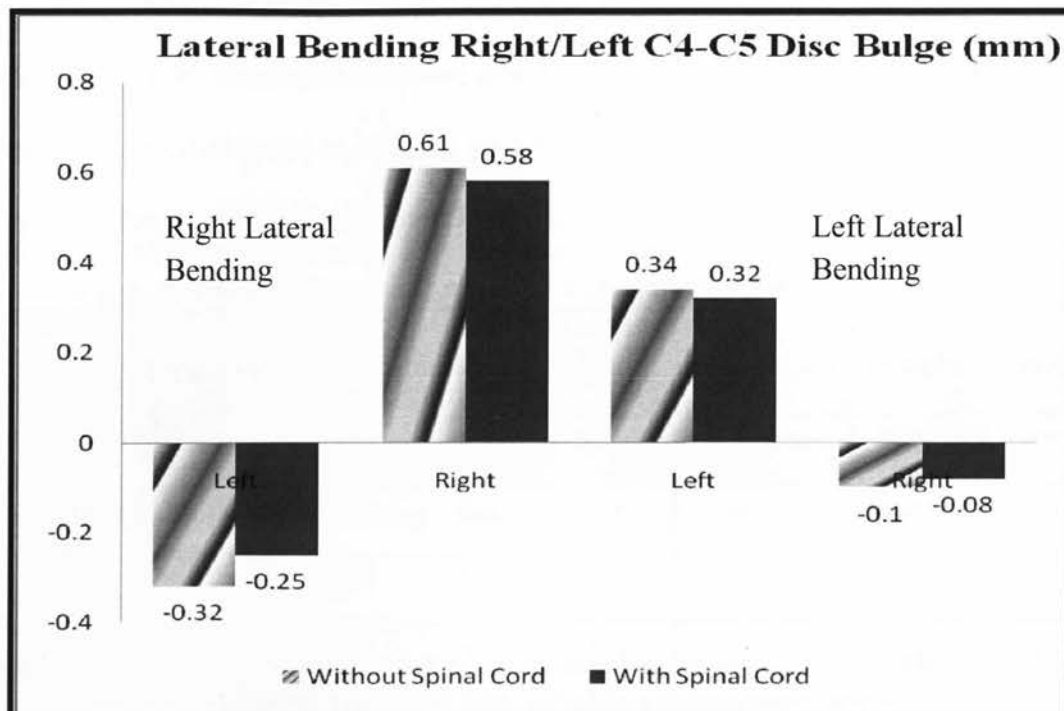


Figure 6-13: Comparison of the C4-C5 disc bulge between model with and without spinal cord.

Additionally, the stress contour plots of the C4-C5 disc, C4 cortical and cancellous bones for compression, flexion/extension and right/left lateral bending (with spinal cord model) were shown in Appendix B. Also, **Table 6-4** summarizes the maximum equivalent von mises stress of with and without spinal cord models. The results showed that the presence of spinal cord into the model has less impact on discs than vertebrae which is almost negligible. In compression, the amounts of stress difference between the two models are almost negligible for both vertebrae components and disc. However, in flexion/extension, having the spinal cord into the model reduced the amount of stress that the cortical and cancellous bones see.

Table 6-4 : Maximum equivalent von misses stress.

Load Direction	Models	Maximum Von Misses Stress [MPa]		
		C4-C5 Disc	C4 Cortical	C4 Cancellous
Compression	Without Spinal Cord	3.60	113	3.00
	With Spinal Cord	3.57	112	2.84
Flexion	Without Spinal Cord	3.33	90.5	1.93
	With Spinal Cord	3.08	75.4	1.18
Extension	Without Spinal Cord	1.03	71.1	1.17
	With Spinal Cord	1.03	62.7	0.78
Right Lateral Bending	Without Spinal Cord	1.52	70.0	3.73
	With Spinal Cord	1.51	69.0	3.63
Left Lateral Bending	Without Spinal Cord	2.12	61.6	2.61
	With Spinal Cord	1.96	55.2	2.15

The pattern of axial motion of the cervical spinal cord varied significantly with vertebral level of the cord. Therefore, the displacements, equivalent von misses stress and axial strain of the anterior and posterior surfaces of the cervical spinal cord were computed from a set of elements along the C4-C5 disc space of the dural sheath, CSF and cord (Table 6-5 and Table 6-6). Anterior surface of the spinal cord is a surface that has a contact with posterior longitudinal ligament and has direct contact to external loads. The results showed that in compression, the anterior surface of spinal cord sees more displacement, stress and strain than posterior surface and vice versa for flexion/extension. The contour plots of dural sheath in compression were shown as Figure 6-14, Figure 6-15 and Figure 6-16 and the rest of the contour plots in compression were shown in Appendix B. Note negative value indicate that the surface is in compression and positive value show that the surface is in tension.

Table 6-5 : Anterior displacement, stress and % of strain in dural sheath, CSF and cord during compression, flexion and extension.

Load Direction	Location	Dural Sheath	CSF	Cord
Compression	Anterior Displacement (mm)	-0.21	-0.21	-0.12
	Stress (KPa)	361	320	0.25
	Axial Strain	-1.3%	-1.6%	-1.1%
Flexion	Anterior Displacement (mm)	0.5	0.44	0.40
	Stress (KPa)	190	96	0.17
	Axial Strain	-0.9%	-0.5%	-0.3%
Extension	Anterior Displacement (mm)	-0.38	-0.31	-0.26
	Stress (KPa)	179	80	0.16
	Axial Strain	0.65%	0.5%	0.4%

Table 6-6: Posterior displacement, stress and % of strain in dural sheath, CSF and cord during compression, flexion and extension.

Load Direction	Location	Dural Sheath	CSF	Cord
Compression	Posterior Displacement (mm)	-0.08	-0.09	-0.10
	Stress (KPa)	220	107	0.14
	Axial Strain	-0.7%	-0.9%	-1%
Flexion	Posterior Displacement (mm)	0.7	0.55	0.51
	Stress (KPa)	520	260	0.58
	Axial Strain	2%	1.6%	0.9%
Extension	Posterior Displacement (mm)	-0.45	-0.35	-0.31
	Stress (KPa)	280	113	0.42
	Axial Strain	-1.1%	-0.9%	-1%

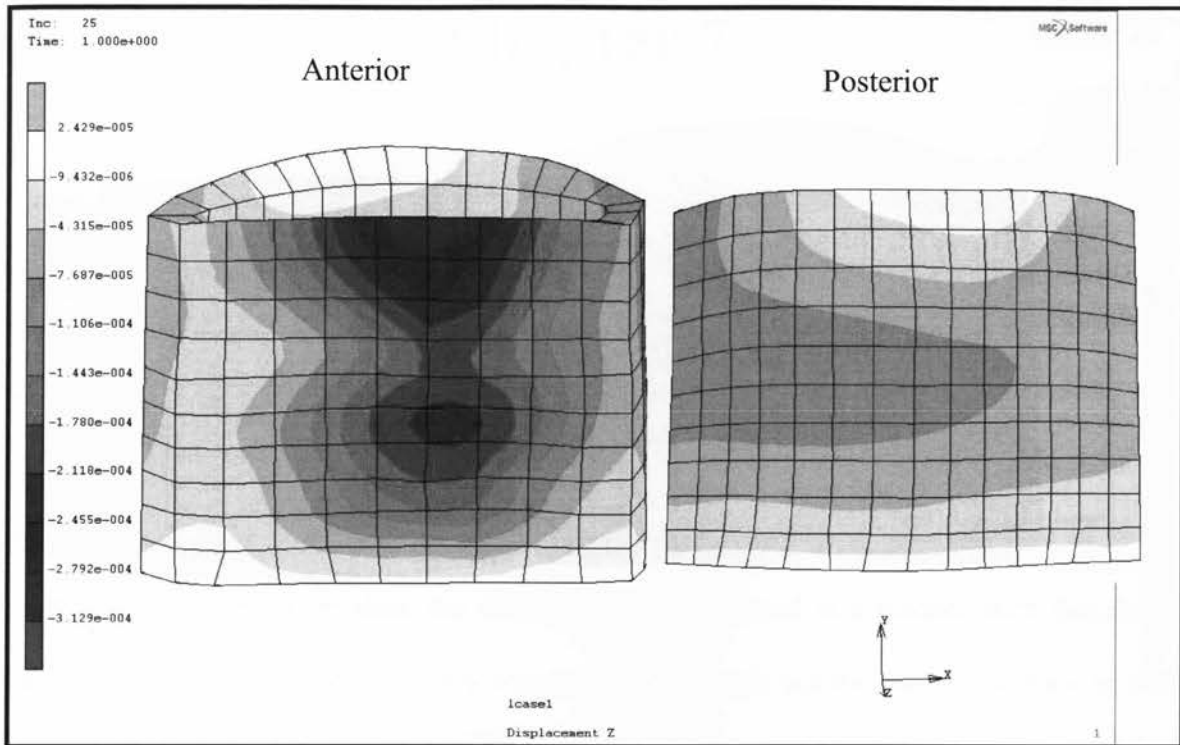


Figure 6-14: Dural sheath z displacement under axial compressive load.

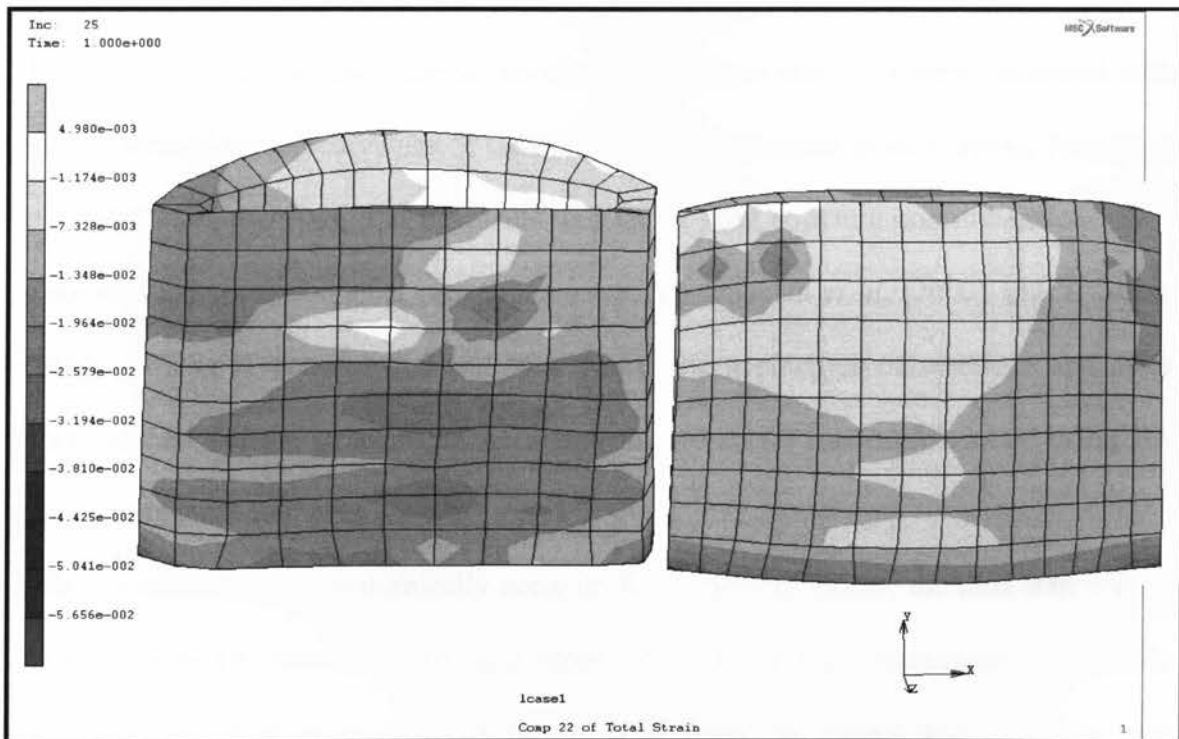


Figure 6-15 : Dural Sheath axial strain under axial compressive load.

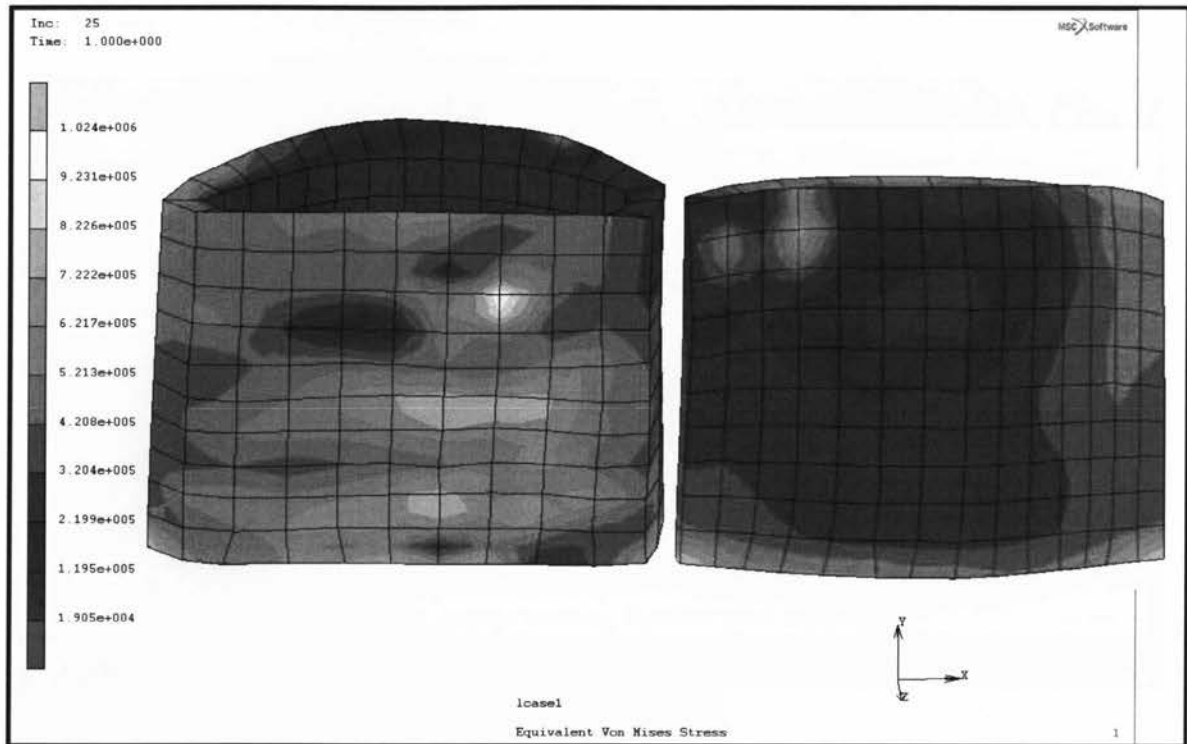


Figure 6-16: Dural sheath equivalent von mises stress under axial compressive load.

Chapter 7

Conclusions

Anatomically accurate and detailed three-dimensional finite element model of the human middle cervical spine (C3-C5) using actual geometric data was developed. All the vital anatomic features of the middle cervical spine, such as the intervertebral disc, cortical bone, cancellous bone, endplates, ligaments and spinal cord were modeled. In most published FE cervical models, the vertebrae were generated in a manner such that there was mid sagittal plane of symmetry which in reality that's not the case. Therefore, in this study, an accurate and non-symmetrical three-dimensional finite element model of complete middle cervical spine with spinal cord was created.

To do so, the structure and dimensions of each vertebrae and discs were compared with experimentally measured values of Gilad *et al.* (1986), Panjabi *et al.* (1991a), Panjabi *et al.* (1993). Furthermore, the ligaments and spinal cord structure and dimensions were generated using experimental measurements of Yoganandan *et al.* (2000) and Yu *et al.* (1985). Using Hypermesh 8.0 and MSC.Marc, the geometries of vertebrae and discs were meshed and the structure of the ligaments and spinal cord were created using 20-noded hexagonal elements.

After incorporating an anatomically accurate finite element model, the next step was to adopt appropriate material model and properties to the spinal components. This study used the soil mechanics formulation of MSC.Marc to model the vertebrae and intervertebral discs as linear biphasic tissue. Also, the ligaments and spinal cord

components were modeled as a linear isotropic model. Note that although the spinal cord components behave as biphasic, the spinal cord was modeled as an elastic model due to lack of property definitions in the literature. Numerous analyses were performed so that one specific set of material properties from values reported in literature proved to be an optimum match to the experimental output under compression, see **Table 5-3**.

After appropriate material properties were assigned, the next step was to simulate the boundary and loading conditions in the model for analysis. The model was fixed at the inferior end of C5 and axial compressive force or moments were applied to the superior end of C3. This procedure remained unchanged in all the analyses because the current finite element model was validated under these conditions. Additional comparisons were made using the existing finite-element model. The intent of the simulations was to identify the quasi-static response of the cervical spine to evaluate the model against available experimental data. A number of different experimental studies were chosen to address compression, flexion, extension and lateral bending modes of loading to gauge the accuracy of model as thoroughly as possible. The current finite-element model was validated against the *in vitro* experimental measurements performed by Shea *et al.* (1991) and Wheeldon *et al.* (2006 and 2008).

The load-displacement curves for the cervical spine segments were finite even for small applied loads. However, the stress-strain relation is linear since linear biphasic material parameters were used in this analysis. It was important to develop a realistic finite element model that can effectively simulate the general finite displacement (displacement is large) of the human cervical spine. The current finite-element model can predict the biomechanical response of the human cervical spine (C3-C5) by using the nonlinear

contact and geometric options under axial compressive force of up to 600 N and was validated against published data. Compressive loading was coupled with a significant extension motion that agrees with Panjabi *et al.* (1986) who reported various compression loads coupled with an extension loading conditions. Current FE model response under compression agreed with the experimental results of Shea *et al.* (1991). The percentage of discrepancy between this analysis and Shea *et al.* (1991) experimental test was approximately 4%. At 600N axial compressive load, the C4 vertebra was compressed by an average of 0.82 mm.

Under compressive loads, the nucleus pulposus forces the annulus fibrosus to bulge outward in both anterior and posterior directions. The amount of disc bulge for C4-C5 disc was measured and compared against the Ng *et al.* (2001) results. The results showed that there were an average of 17% (anterior) and 35% (posterior) discrepancy between this analysis and Ng *et al.* (2001) analysis. The cause of this discrepancy between the current model and their models was likely attributed to the material model and properties selection. However, the maximum bulge occurs at the C4-C5 anterior location which is the same as that determined by Ng *et al.* (2001).

The flexion/extension curves were determined to be asymmetric about zero reference moment. In all curves, the mean value of the rotation under the extension load was determined to be less than the mean value of the flexion load. This asymmetric result is in agreement to that reported by Wheeldon *et al.* (2006) however, disagrees to that described by Panjab *et al.* (1994), Nightingale *et al.* (2002). The cause of the difference can be explained by the anatomic asymmetry of the human neck in the sagittal plane, as well as an asymmetric vertebral body shape. It was found that the biomechanical

response of the C3-C4 and C4-C5 model correlated well within Wheeldon *et al.* (2006) experimental results. The results showed that the maximum rotation angle for C4-C5 segment at 2 Nm was 5.5 degree in flexion and 4.8 degree in extension which fall within the range of Wheeldon *et al.* (2006) experimental test.

In flexion and extension rotational responses of the motion segments, a “slack” effect can be seen. The initial portions of the responses have a large slope until to approximately 0.33 Nm where the ligaments are not playing as large of a role. Thus, the slope suddenly changes; this is defined as "slack". Once the ligaments have been stretched to a certain point, they influence the rotational response more significantly rather than the vertebral geometry or other factors. During flexion, the interspinous ligament, ligamentum flavum and posterior longitudinal ligament stretched. Conversely, during extension, anterior longitudinal ligament stretched. In addition, the flexion and extension motion is affected by the facet joints. In flexion the superior facet surfaces slid up and forward while in extension the superior facet surfaces slide down and backwards. The facet joint gap also undergoes a narrowing in extension and a widening in flexion, Wheeldon *et al.* (2006).

The lateral disc bulge of the C4-C5 was measured for both anterior and posterior locations. Under both flexion/extension, the maximum disc bulge occurs at the C4-C5 anterior location. However, in flexion the disc bulges outward in anterior location and in extension disc bulges inward in anterior location. In flexion, the nucleus pulposus tended to shift backward (towards posterior location) even though the disc bulged outward in the anterior. Furthermore, the disc bulges inward (concave) in the posterior location under flexion. Under extensional loading, the disc tends to shift inward at anterior location (disc bulge in) and it bulged outward in the posterior. The displacement on nucleus pulposus is

opposite to the disc bulge out at posterior location. This is identical to the disc behavior under flexion. This behavior of the intervertebral disc agrees with qualitative observation of White and Panjabi (1990). Also, in flexion, the superior vertebrae was inclined to move in the anterior direction, and vice versa for the extension case which is similar to the motions reported by Moroney *et al.* (1988).

In addition to extension and flexion, the right and left lateral bending response of the C4-C5 vertebrae were computed and compared against the Wheeldon *et al.* (2008) experimental results. The maximum rotation angle for C4-C5 segment at 2 Nm was 4 degree in right and 3 degree in left lateral bending and these values correspond to Wheeldon *et al.* (2008) findings. These FEM results of lateral bending were within one standard deviation of the experimental results. Finally, the left and right hand side of C4-C5 disc bulge were measured. The results showed that in right lateral bending, the disc bulges more toward the right hand side and vice versa in left lateral bending. It was found that the applied lateral bending moment produced complementary axial rotational motion. This means that applied lateral bending moment induces small axial rotation (twisting of the vertebrae). This happens primarily because of the asymmetric geometry of cervical vertebrae. This coupled motion agrees well with results reported by Moroney *et al.* (1988).

There were very few studies (three studies in all) that have considered the spinal cord into their cervical spine model. Therefore, one of the objectives of this study was to develop anatomically accurate model of spinal cord and to study its behavior under various loading conditions. To accomplish this goal the compression, flexion/extension and right/left lateral bending analyses were repeated by considering the spinal cord into the

model aggregate. The disc bulge of these analyses for both anterior and posterior locations of C4-C5 disc were measured and compared with the results of the previous model (cervical spine without spinal cord). The results showed that inclusion of the spinal cord into the model reduced the amount of lateral disc bulged. In compression, the spinal cord compressed and bulged outward and this could therefore provide considerable resistance to disc bulge. In flexion, the anterior and posterior sides of the spinal cord see compression and tension respectively and vice versa for the extension case. During the flexion/extension, the spinal cord reduced the amount of rotation, thereby reduced the amount of lateral disc bulge. However, in flexion the amount of disc bulge reduction was less than the amount of disc bulge in extension. In extension, the spinal cord acts as a resistance that pushes against the direction of the disc bulge, while in flexion the spinal cord pushes in favor of disc bulge. In right and left lateral bending, the spinal cord provides support to resist the rotational deformation and as such it reduced the disc bulge by a smaller amount than flexion/extension.

In addition, the maximum equivalent von mises stress of the C4-C5 disc, C4 cortical and cancellous bones for compression, flexion/extension and right/left lateral bending were measured. The results of analysis in flexion, extension and lateral bending showed that the presence of spinal cord into the model has less impact on discs stress than vertebrae stress in which case the disc stress difference could be considered negligible. In compression, the amounts of stress difference between the two models are almost negligible for both vertebrae components and discs. However, in flexion/extension, having the spinal cord into the model reduced the amount of stress that the cortical and cancellous bones see.

The maximum amount of stress in C4-C5 disc, disc bulge and the location that the maximum bulge happens for all aforementioned loading conditions for both models (with and without spinal cord) are summarized in **Table 7-1**.

Table 7-1: Maximum C4-C5 disc stress, disc bulge and location.

Loading Conditions	Without Spinal Cord			With Spinal Cord		
	Max Disc Bulge (mm)	Location	Max Stress (Mpa)	Max Disc Bulge (mm)	Location	Max Stress (MP)
Compression	0.57	Anterior	3.6	0.54	Anterior	3.57
Flexion	0.79	Anterior	3.33	0.73	Anterior	3.08
Extension	-0.62	Anterior	1.03	-0.51	Anterior	1.03
Right lateral bending	0.61	Right hand side	1.52	0.58	Right	1.51
Left lateral bending	0.34	Left hand side	2.12	0.32	Left	1.96

The displacements, von misses stress and axial strain of the anterior and posterior surfaces of the cervical spinal cord were computed from a set of elements along the C4-C5 disc space of the dural sheath, CSF and cord. The results showed that in compression, the anterior surface of spinal cord sees more displacement, stress and strain than posterior surface. In compression, the anterior surface of spinal cord has a contact with posterior longitudinal ligament and they have a direct contact with external load therefore, they see more stress and strain. In flexion and extension, the posterior surface of the spinal cord sees more stress, strain and displacement than the anterior, which is in agreement with the experimental published data of Yuan *et al.* (1998).

As with any analytical model, there are some limitations. First, the model does not include muscles. However, as many authors have found, muscles do not react in time to prevent injury from occurring in the case of high and sudden loading. Secondly, since relatively little is known about the exact material properties of the spinal cord

components, assumptions was made based on the data available in the literature. Therefore, the spinal cord material response was model as linear isotropic not linear biphasic. In the future, more experimental work needs to be done to more accurately define the material properties so a more accurate simulation can be performed.

Strength of the current investigation was that the model was validated against experimental curves of healthy young, normal specimens ranging in age from 20 to 51 years. The validation was within one standard deviation of the published experimental and FE findings. This allows the user to have confidence that the internal parameter values (i.e., stresses and strains) will be accurately determined with this model.

Appendix A

A.1 Biphasic Background Mathematical Formulation

The theory of mixtures can be applied to a multi-phase continuum with an arbitrary number of phases. However, for this research purpose we focus on a two-phase mixture of solid and fluid, and define the governing equations accordingly.

Consider two continuum bodies Ω^s and Ω^f in three dimensional space, where the superscripts s and f denote the solid and the fluid constituents, respectively. Let X^α be the position of a particle of the α phase in its reference (undeformed) configuration or material description ($\alpha = s, f$). The current (deformed) configuration or spatial description of each body (x^α) at the time t can be represented by the deformation function χ^α . The current spatial position x^α of the particle X^α at the time t can be expressed as:

$$x^\alpha = \chi^\alpha(X^\alpha, t), \quad \alpha = s, f \quad (\text{A-1})$$

Consider an apparent domain Ω of the soft tissue at time t in three dimensional space which coincides with the domain Ω^s of the solid phase (**Figure A-1**). Let Γ denote the boundary of Ω , and let V denote the volume of Ω . Using the same reference axes for both x^α and X^α , the deformed configuration of the solid and fluid phases can be written as :

$$x^s = \chi^s(X^s, t) = X^s + u^s(X^s, t) \quad (\text{A-2})$$

$$\mathbf{x}^f = \chi^f(\mathbf{X}^f, t) = \mathbf{X}^f + \mathbf{u}^f(\mathbf{X}^f, t) \quad (\text{A-3})$$

where \mathbf{u}^s is the displacement of the solid phase. The velocity of a particle of each phase can be defined as the time derivative of the corresponding deformation function of equation (A-1):

$$\mathbf{v}^\alpha = \frac{\partial \mathbf{x}^\alpha}{\partial t} \quad (\text{A-4})$$

The deformation gradient for the α -constituent, F^α , and its Jacobian (volume ratio), J^α are defined as:

$$F^\alpha = \nabla_o \chi^\alpha = \frac{\partial \mathbf{x}^\alpha}{\partial \mathbf{X}^\alpha} \quad (\text{A-5})$$

$$J^\alpha = \det F^\alpha \quad (\text{A-6})$$

The subscript 'o' on the gradient operator implies that the operation is performed with respect to the initial coordinates. The right hand side of the equation expresses the change in the relative position of two neighboring particles before and after deformation. Note that F^α is always nonsingular and J^α must be strictly positive to prohibit self-interpenetration of each continuum.

The right Cauchy-Green tensor C^s and the left Cauchy-Green tensor (Piola deformation tensor) B^s for the solid-constituent are defined as:

$$C^s = F^{sT} F^s \quad (\text{A-7})$$

$$B^s = F^s F^{sT} \quad (\text{A-8})$$

The first Piola-Kirchhoff (or nominal) stress tensor P^s defined as:

$$P^s = J^s \sigma^s F^{-T} \tag{A-9}$$

Note that P^s is a mixed (or two-point) tensor that shifts the area element from its material configuration to its current configuration. Using push-forward and pull-back operations on the contravariant tensor field, the second Piola-Kirchhoff stress S^s can be determined from Cauchy stress or the reverse of this relation. For a detailed explanation of pull-back and push-forward operations, the reader is referred to Ogden (1984), Spencer (1984), Holzapfel (2000).

$$S^s = J^s F^{s-1} \sigma^s F^{s-T} \tag{A-10}$$

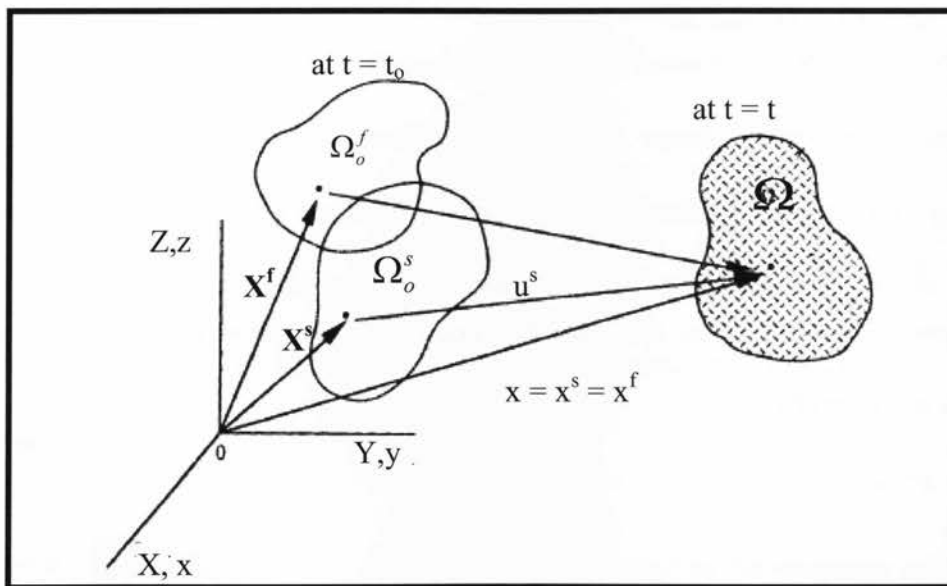


Figure A-1: The kinematics relationship between the solid and fluid reference configurations and the current configuration (Adopted from Suh et al., 1991).

The name biphasic mixture designates a binary mixture composed of a porous solid matrix saturated with fluid. The phases are assumed to be immiscible, intrinsically incompressible and chemically inert. It is further assumed that the mixture is isothermal and has a constant temperature.

The balance of mass for the constituents and for the mixture can be represented by the equations:

$$\phi^s + \phi^f = 1 \quad (\text{A-11})$$

$$\nabla \cdot (\phi^s v^s + \phi^f v^f) = 0 \quad (\text{A-12})$$

The first equation indicates that the mixture is saturated; the second equation is the continuity equation for a biphasic mixture; ∇ is the gradient operator with respect to the current configuration, v^α is the velocity of the α phase, the volume fraction ϕ^s and ϕ^f are called the solidity and porosity of the mixture, respectively. The volume fraction ϕ^α and void ratio e are defined as:

$$\phi^\alpha = \frac{V^\alpha}{V} \quad (\text{A-13})$$

$$e^\alpha = \frac{\phi^\alpha}{(1 - \phi^\alpha)} \quad (\text{A-14})$$

Under quasi-static conditions, the momentum equations for the solid and fluid phases of the tissue are given by:

$$\nabla \cdot \sigma^\alpha + \pi^\alpha = 0 \quad (\text{A-15})$$

Constitutive equations are as follows:

$$\sigma^s = -\phi^s p \mathbf{I} + \sigma_E^s \quad (\text{A-16})$$

$$\sigma^f = -\phi^f p \mathbf{I} \quad (\text{A-17})$$

$$\pi^s = -\pi^f = \mathbf{K}(v^f - v^s) - p \nabla \phi^f \quad (\text{A-18})$$

Here, σ^α is the Cauchy stress tensor for the α phase, π^α is the diffusive momentum exchange between the two phase, p is the apparent pressure, I is the identity tensor, σ_E^s is the elastic Cauchy stress tensor of the solid phase and K is the scalar diffusive drag coefficient, related to the tissue permeability k through:

$$K = \frac{(\phi^f)^2}{k} \quad (\text{A-19})$$

As seen in (A-16) and (A-17) the superposed continua approach leads to the fact that pressure is shared between the two phases. Physically, what the solid phase experiences is the sum of the elastic stress and the pressure, i.e. the total stress. Since hydrostatic pressure does not contribute to the failure of an elastic material, elastic stress stands out as the most important quantity in cartilage mechanics, which is completely determined from the deformation, and a hydrostatic stress that depends on the pressure p . In fact, elastic stress is attributed a special importance also in soil mechanics known as effective stress σ_E^s , Ogden (1984) . For a general nonlinear model, σ_E^s (soil effective stress) is defined as:

$$\sigma_E^s = 2\rho^s F^s \cdot \frac{\partial \psi^s}{\partial C^s} \cdot F^{sT} \quad (\text{A-20})$$

where ψ^s is the Helmholtz free energy function of the solid phase, ρ^s is the apparent density of the solid phase, F^s is the deformation gradient of the solid phase, C^s is the right Cauchy-Green tensor of the solid phase.

From the expressions for σ^s and S^s in equation (A-20) and (A-10):

$$S_E^s = 2\rho_0^s \frac{\partial \Psi^s}{\partial C^s} \quad \text{and} \quad \sigma_E^s = \frac{1}{J^s} F^s S_E^s \cdot F^{sT} \quad (\text{A-21})$$

The choice of the free energy function is not unique. Based upon experiments on bovine or human cartilage and considering certain constitutive requirements in multi-dimensional stress states, many version of the free energy and the permeability functions are reported in the literature studies, such as Holmes et al. (1986) and Suh et al. (1991):

$$\Psi^s = \gamma \frac{e^{[\alpha_1(I_1-3)+\alpha_2(I_2-3)]}}{I_3^n} \quad (\text{A-22})$$

$$k = k_0 \left(\frac{J^s}{J^f} \right) e^{M(I_3-1)/2} \quad (\text{A-23})$$

where I_1, I_2 and I_3 are the principal strain invariant; $\alpha_1, \alpha_2, \gamma, n, k_0$ and M are material parameters find through regression analysis; and J^s and J^f are the volume changes of each phase. From the intrinsic incompressibility of each phase, it can be shown that:

$$\phi_0^\alpha = J^\alpha \phi^\alpha, \alpha = s, f \quad (\text{A-24})$$

and

$$\frac{1}{J^f} = \frac{1}{J^s} + \frac{1}{\phi_0^f} \left(1 - \frac{1}{J^s} \right) \quad (\text{A-25})$$

where the subscript $()_0$ is used to denote a quantity at the reference configuration.

The permeability, k in equation (A-26), can be reduced to either of the following;

$$\text{Linear model:} \quad k = k_0 \quad (\text{A-27})$$

$$\text{Nonlinear model:} \quad k = k_0 \exp[M\varepsilon_{ii}] \quad (\text{A-28})$$

where ε_{ii} is the dilatation and M is a constant used to match measurements.

A.2 Proelastic Background Mathematical formulation

In soil mechanics, it is convenient to decompose the total stress σ into a pore pressure component and the deviatoric or effective stress σ_E .

$$\sigma = -pI + \sigma_E \quad (\text{A-29})$$

Note the sign convention used; a positive pore pressure results in a compressive stress.

The momentum balance (equilibrium) equations are with respect to the total stresses in the system.

$$\nabla \sigma + f = \rho \ddot{u} \quad (\text{A-30})$$

where ρ is the density, and f , \ddot{u} are the body force and the acceleration. The equilibrium equation can then be expressed as:

$$\nabla \sigma_E - \nabla p + f = \rho \ddot{u} \quad (\text{A-31})$$

The fluid flow behavior can be modeled using D'Arcy's law, which states that the fluid's velocity, relative to the soil's skeleton, is proportional to the total pressure gradient.

$$\dot{u}_f = \frac{-K}{\mu} (\nabla p + \rho_f g) \quad (\text{A-32})$$

where \dot{u}_f is the fluid's bulk velocity; K is the soil permeability; μ is the fluid viscosity;

ρ is the fluid density and g is the gravity vector.

The fluid is assumed to be slightly compressible.

$$p = K_f \frac{\dot{\rho}_f}{\rho_f} \quad (\text{A-33})$$

where K_f is the bulk modulus of the fluid.

However, the compressibility is assumed small enough such that the following holds:

$$\nabla \cdot \left[\rho_f \frac{K}{\mu} (\nabla p + \rho_f g) \right] \approx \rho_f \nabla \cdot \left[\frac{K}{\mu} (\nabla p + \rho_f g) \right] \quad (\text{A-34})$$

It is also assumed that the bulk modulus of the fluid is constant, introducing the fluid's compressibility β_f .

$$\beta_f = 1/K_f \quad (\text{A-35})$$

The solid grains are assumed to be incompressible. Under these assumptions, the governing equations for fluid flow is

$$\nabla \cdot \left[\frac{K}{\mu} (\nabla p + \rho_f g) \right] = \phi \beta_f \dot{p} + \nabla \cdot \dot{u} \quad (\text{A-36})$$

Where ϕ is the medium's porosity.

It is important to note that the medium's porosity is only dependent upon the original porosity and the total strains. Letting V_f and V_s stand for the fluid and solid's volume

$$\phi = dV_f / (dV_f + dV_s) = 1 - J^{-1}(1 - \phi_0) \quad (\text{A-37})$$

Where J is the determinant of the deformation gradient and ϕ_0 is the original porosity, both with respect to the reference configuration.

Appendix B

Compression with spinal cord:

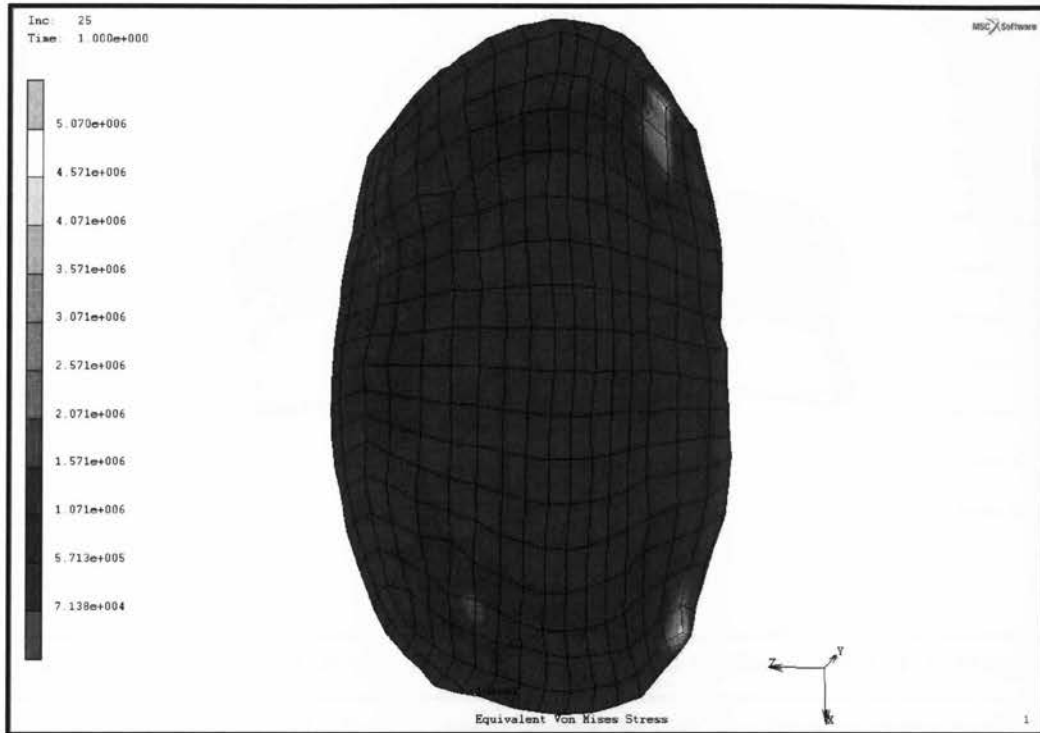


Figure B-2: C4-C5 disc stress under compression with spinal cord.

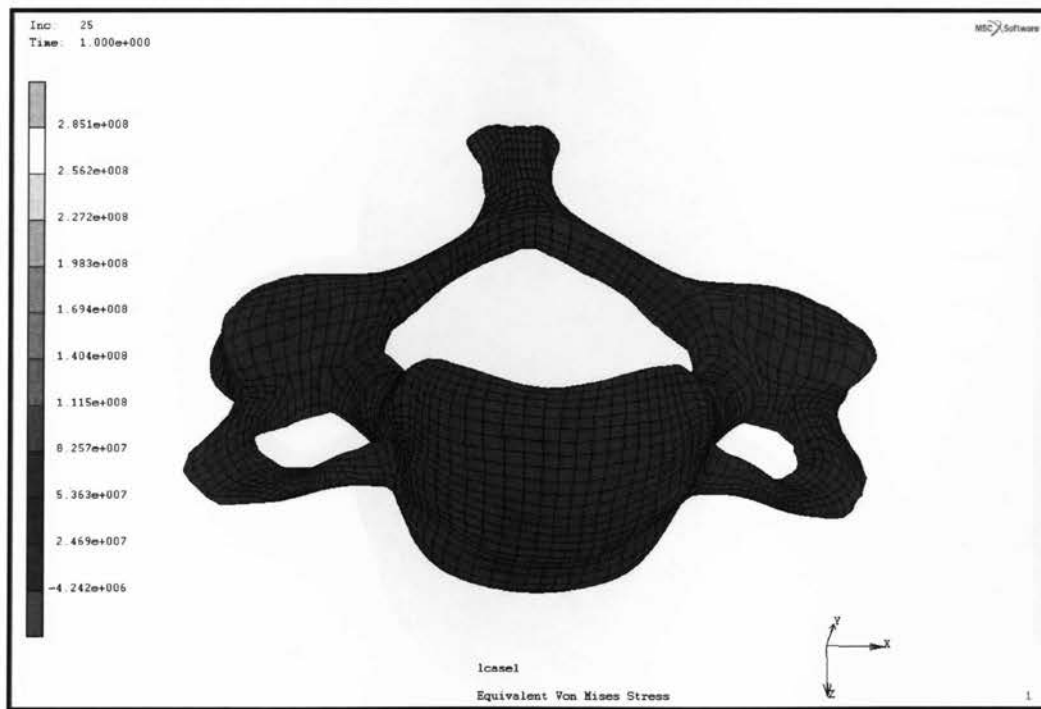


Figure B-3: C4 cortical stress under compression with spinal cord.

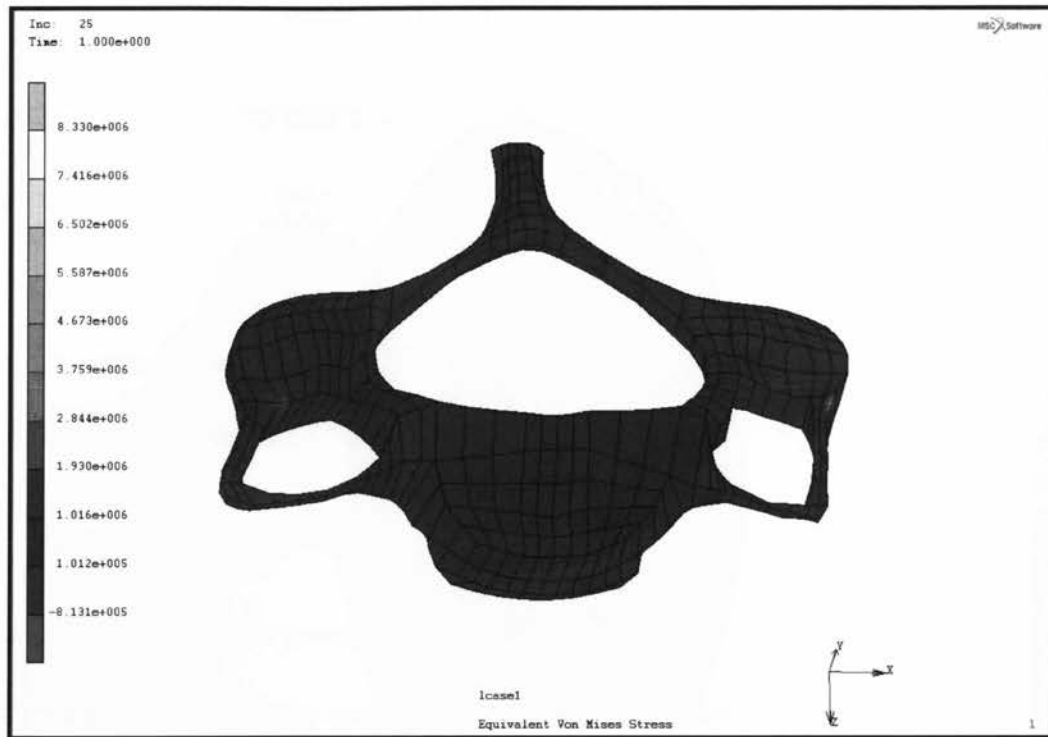


Figure B-4: C4 cancellous bone stress under compression with spinal cord.

Extension with spinal cord:

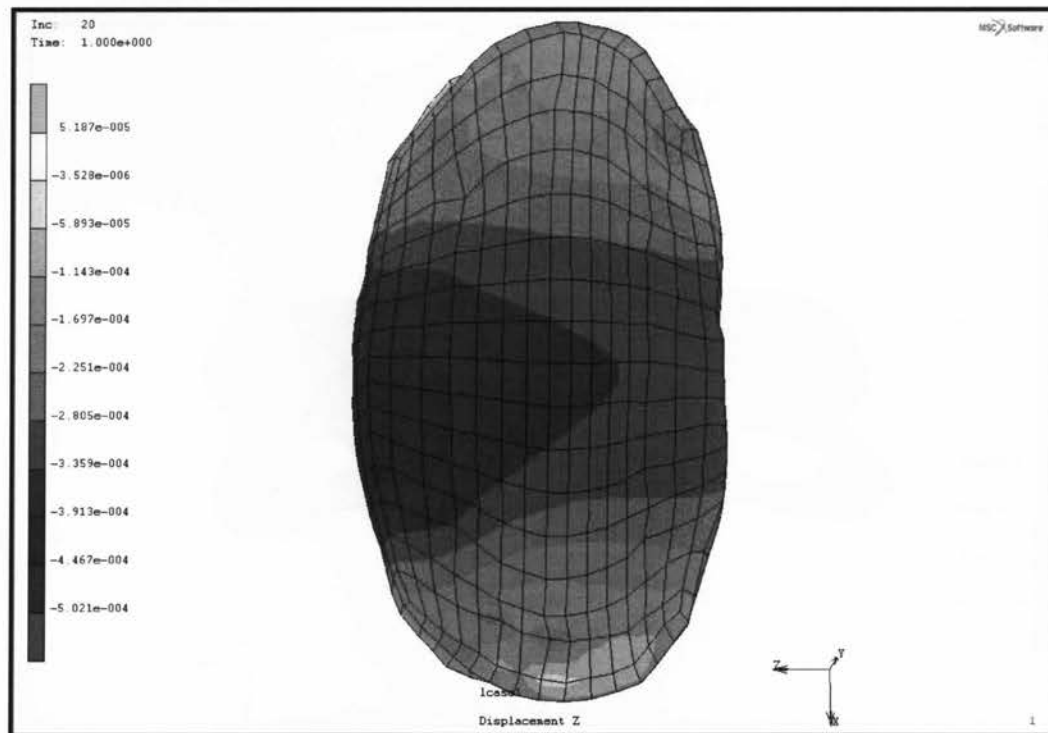


Figure B-5: C4-C5 disc z displacement under extension with spinal cord.

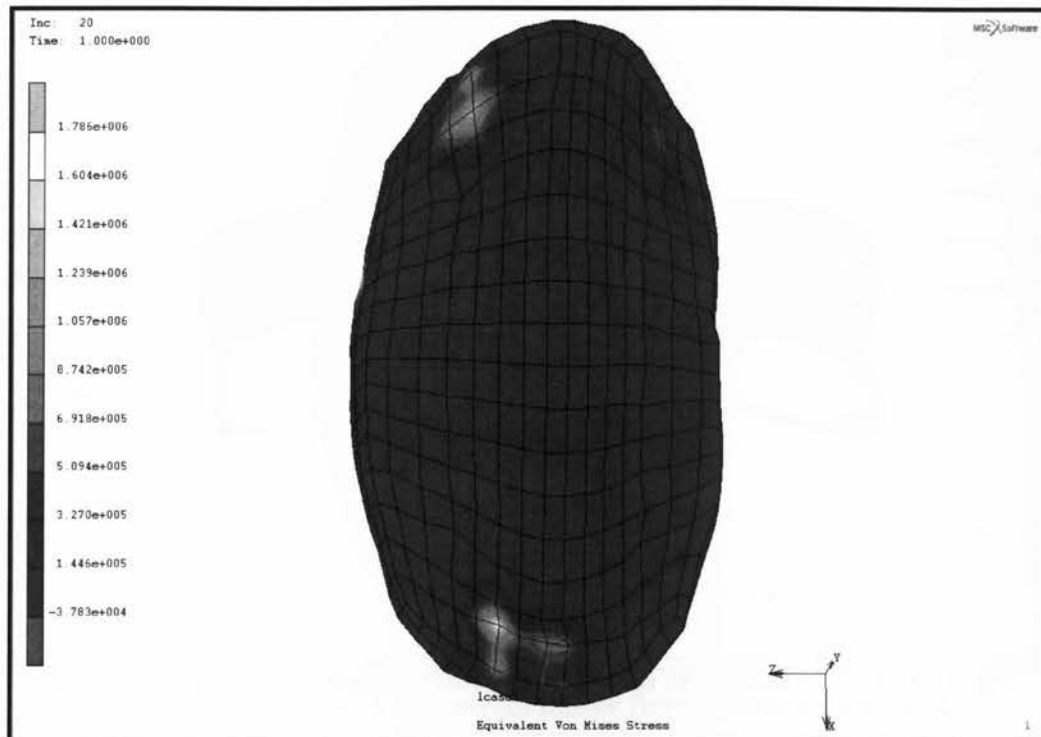


Figure B-6: C4-C5 disc stress under extension with spinal cord.



Figure B-7: C4 cortical bone stress under extension with spinal cord.

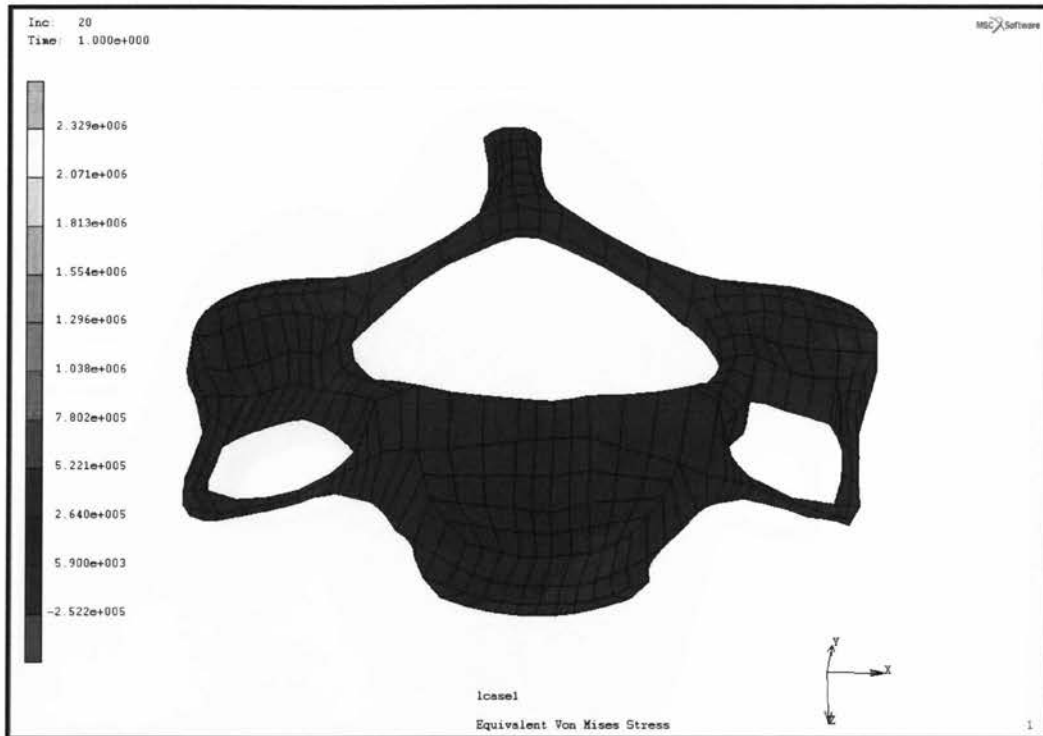


Figure B-8: C4 cancellous bone stress under extension with spinal cord.

Flexion with Spinal cord:

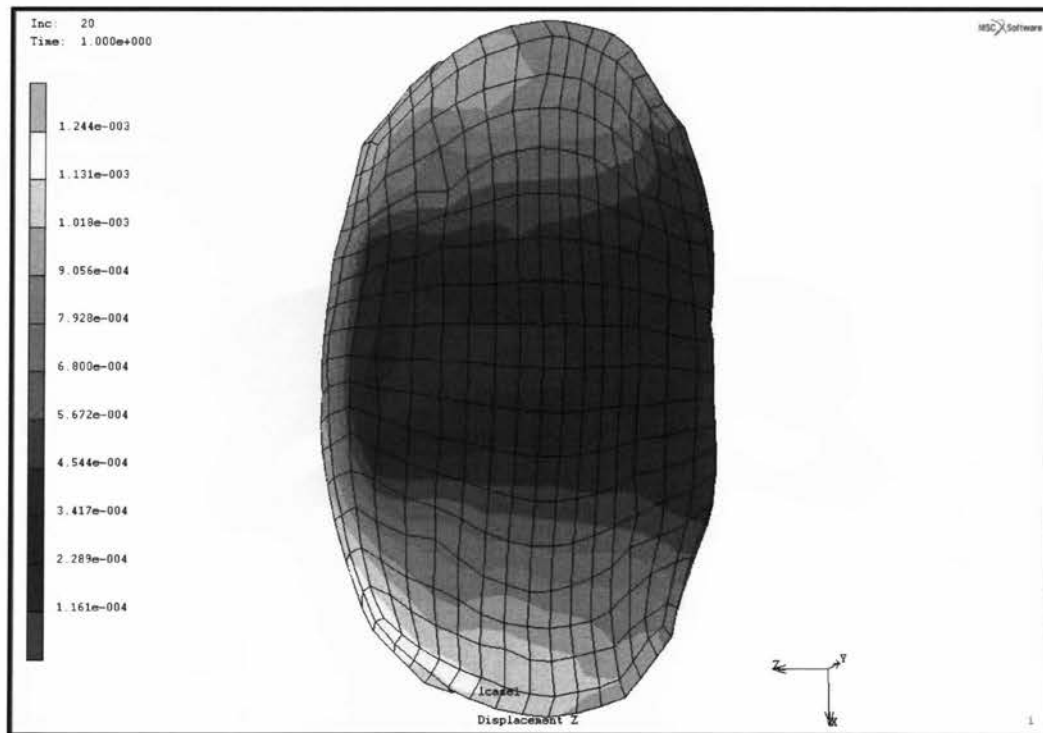


Figure B-9: C4-C5 disc z displacement under flexion with spinal cord.

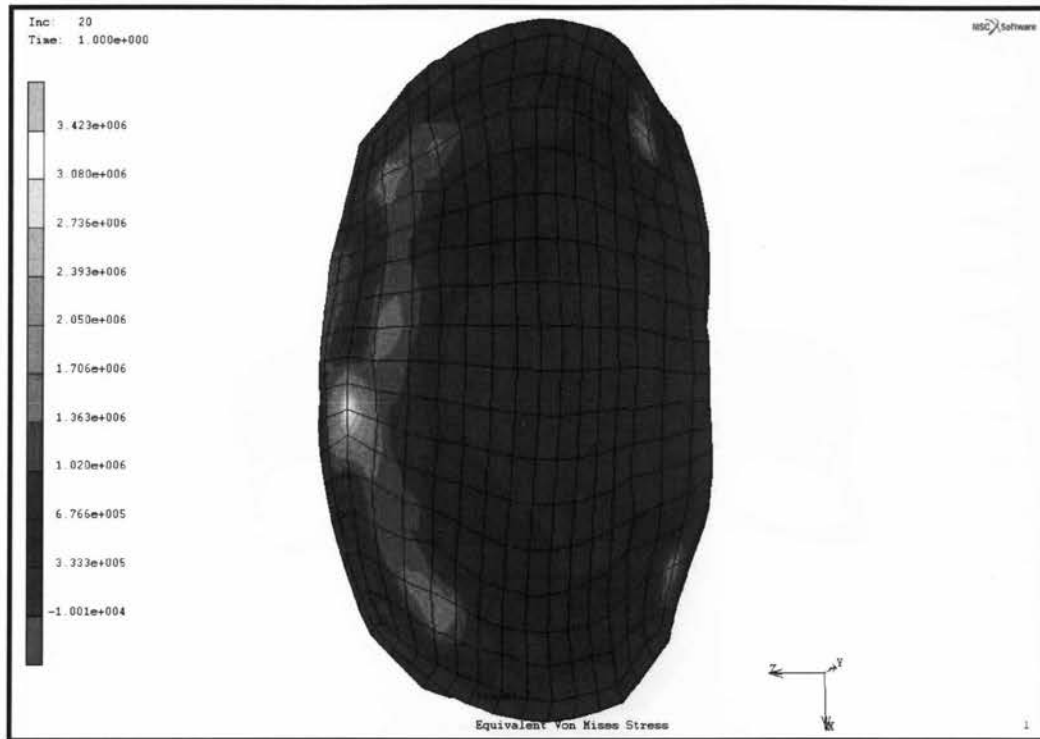


Figure B-10: C4-C5 disc stress under flexion with spinal cord.



Figure B-11: C4 cortical bone stress under flexion with spinal cord.

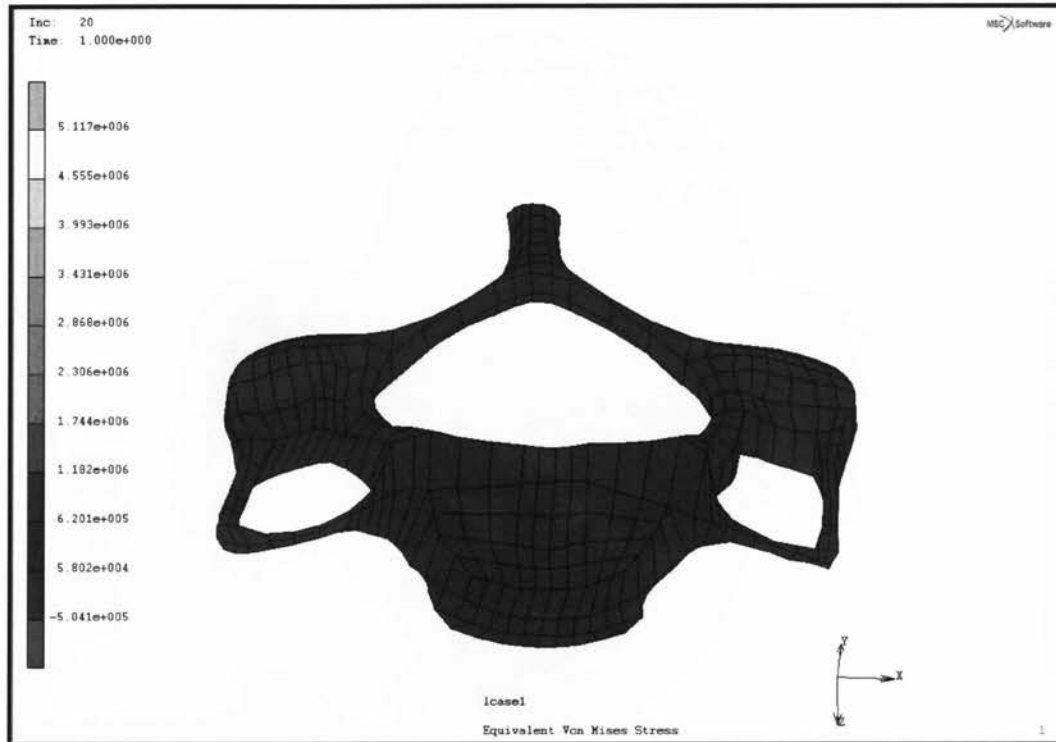


Figure B-12: C4 Cancellous bone stress under flexion with spinal cord.

Right Lateral with Spinal Cord:

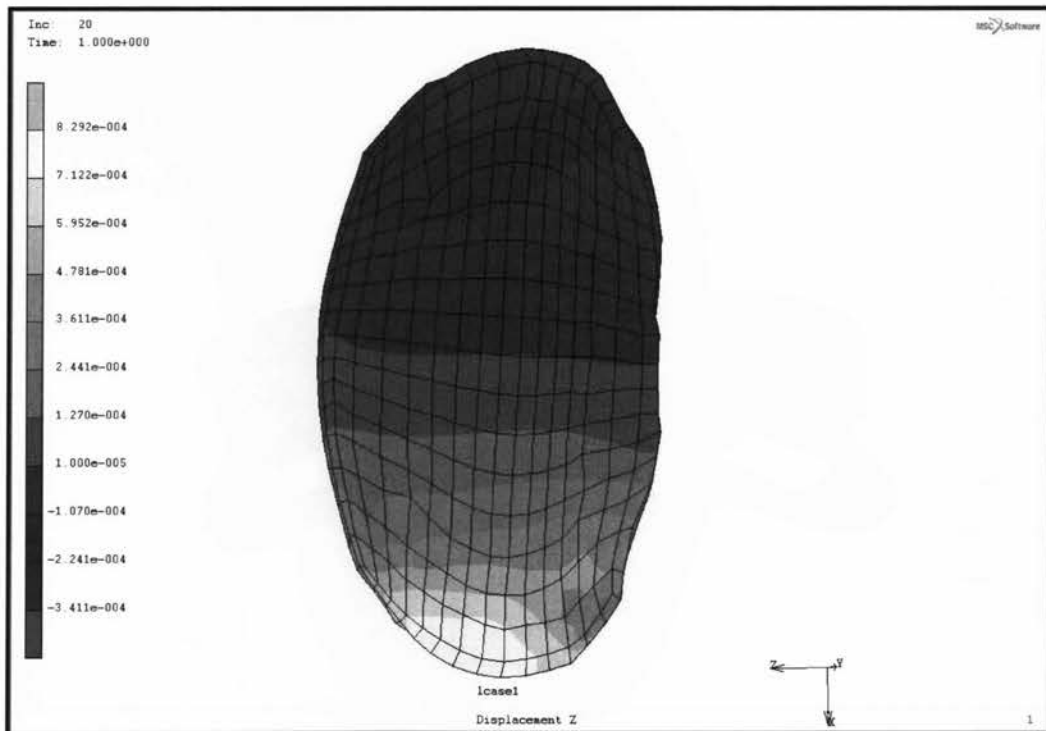


Figure B-13: C4-C5 disc z displacement under right lateral with spinal cord.

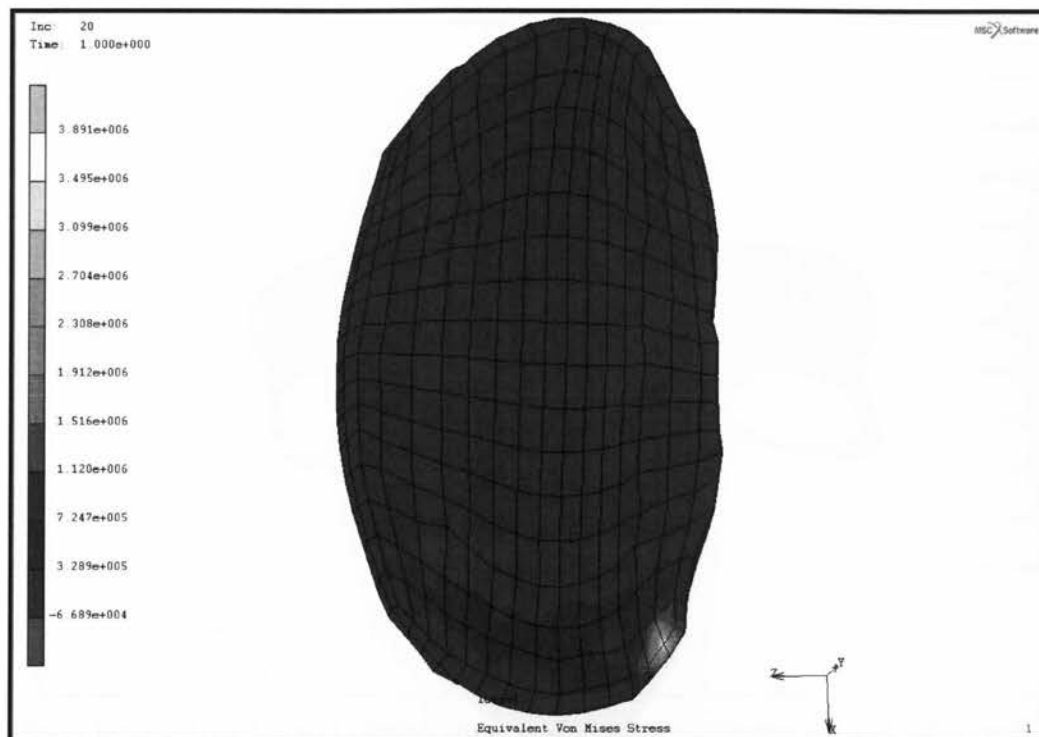


Figure B-14: C4-C5 disc stress under right lateral with spinal cord.

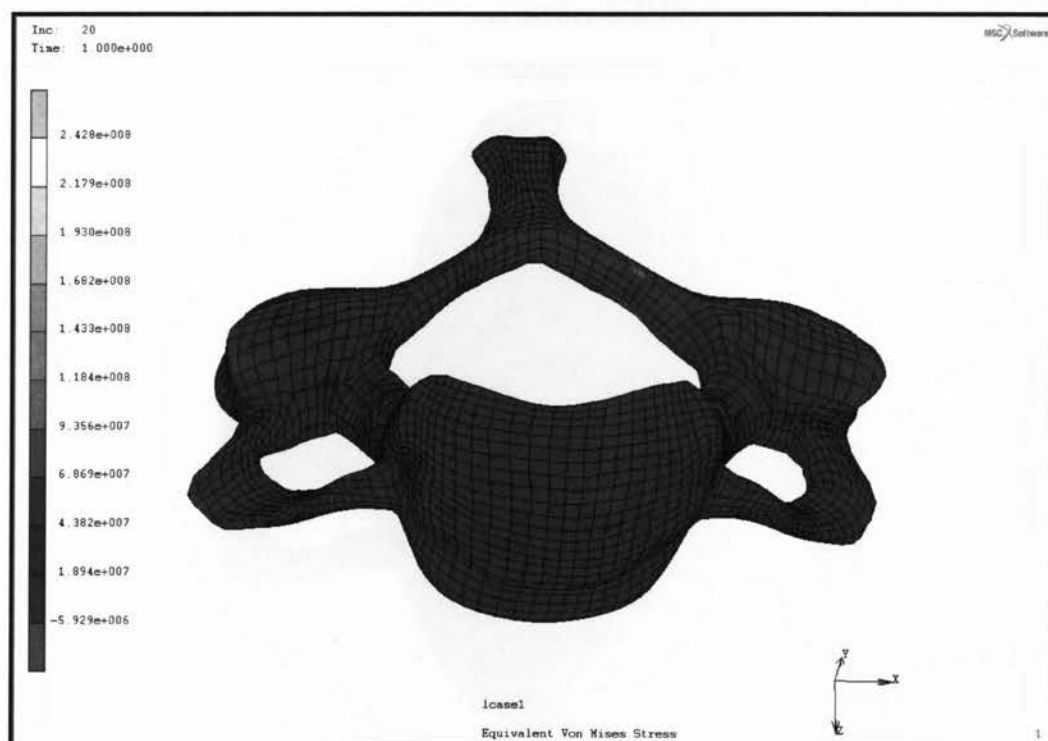


Figure B-15: C4 cortical bone stress under right lateral with spinal cord.

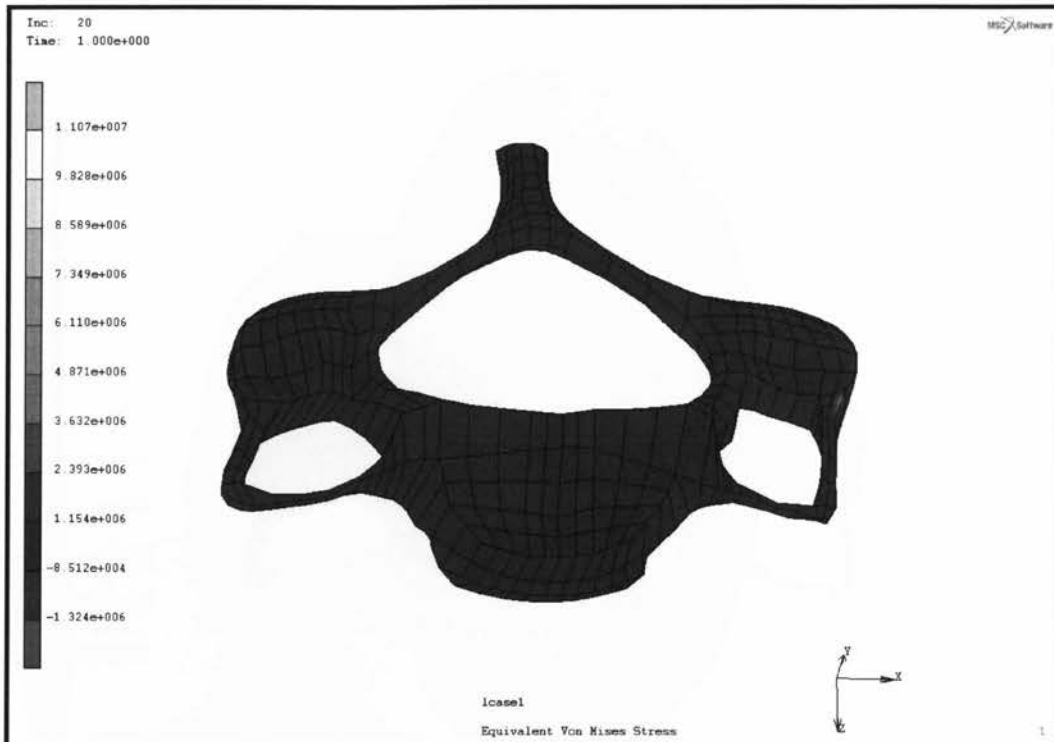


Figure B-16: C4 cancellous bone stress under right lateral with spinal cord.

Left Lateral with Spinal Cord:

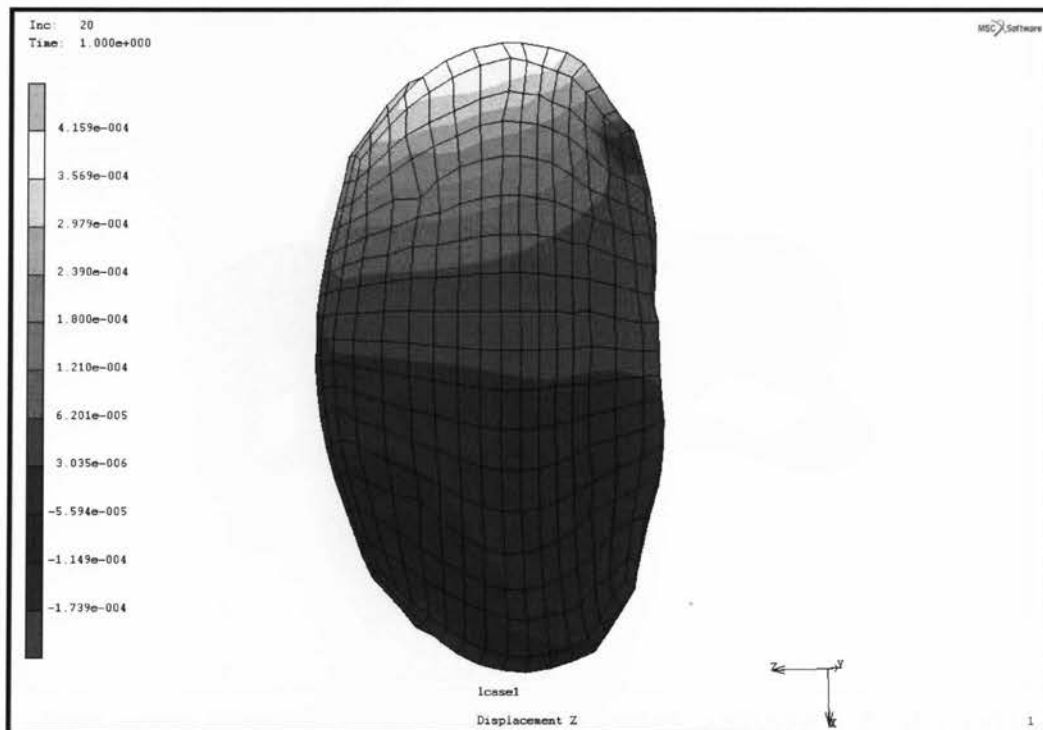


Figure B-17: C4-C5 disc z displacement under left lateral with spinal cord.

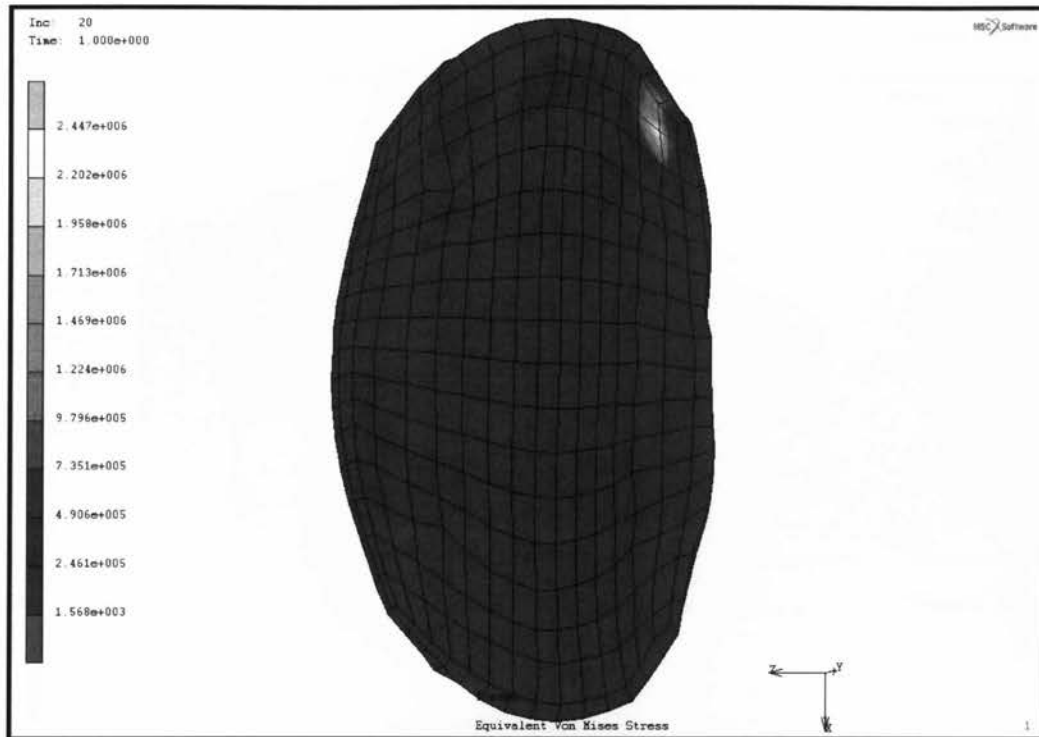


Figure B-18: C4-C5 disc stress under left lateral with spinal cord.



Figure B-19: C4 cortical bone stress under left lateral with spinal cord.

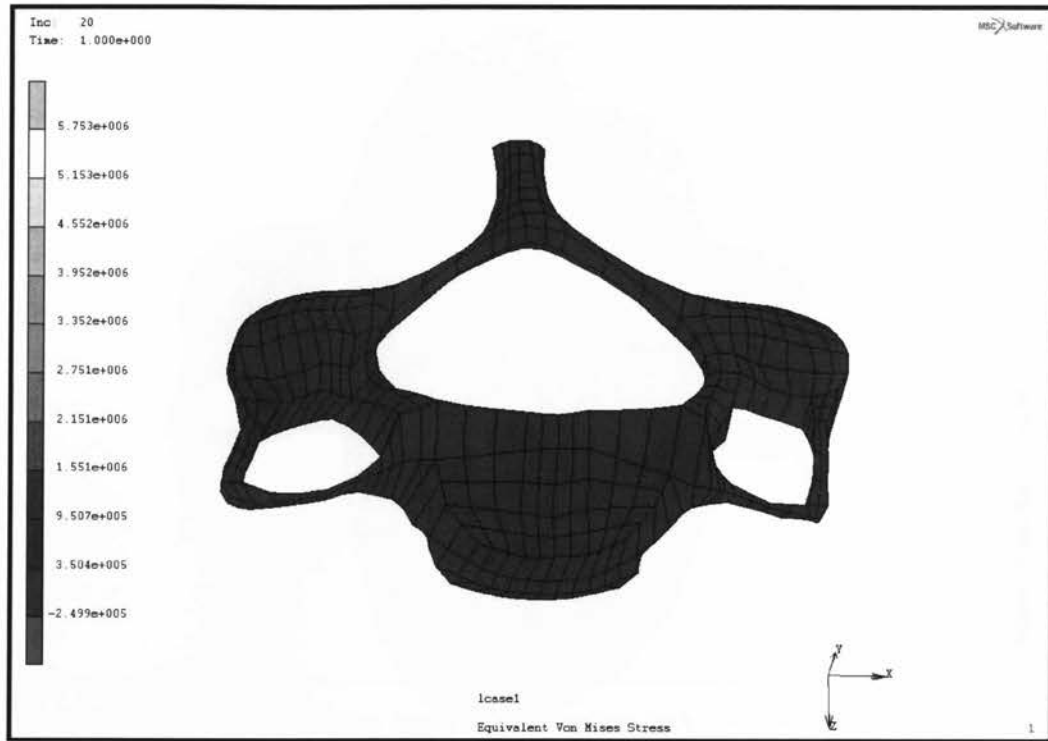


Figure B-20: C4 cancellous bone stress under left lateral with spinal cord.

Spinal Cord under Compression:

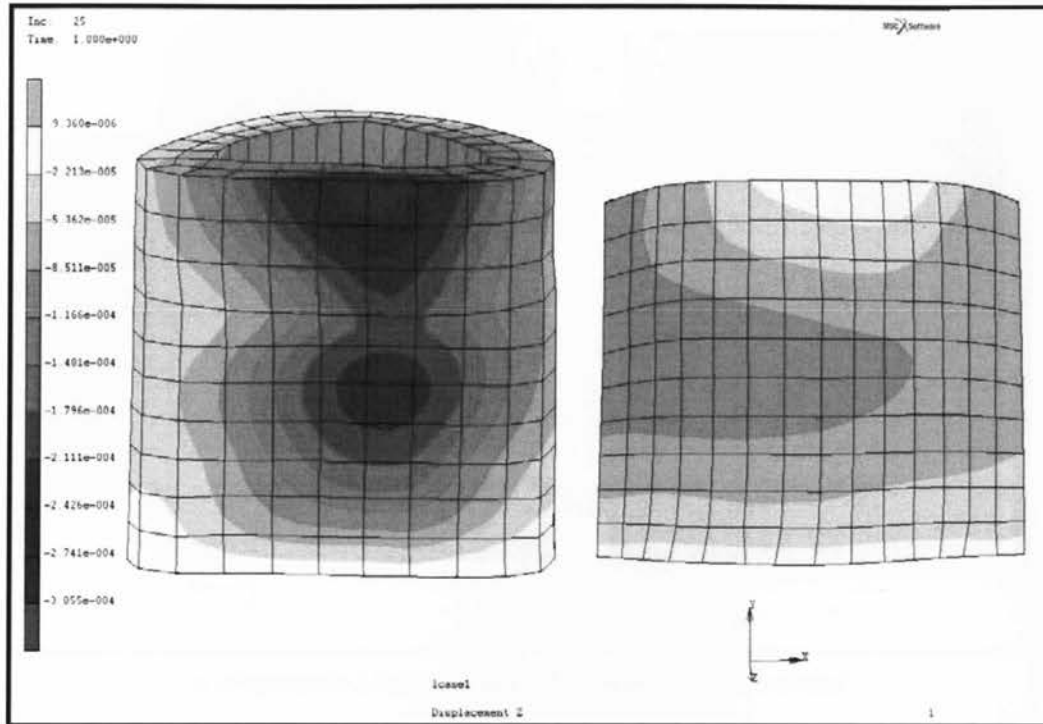


Figure B-21: CSF z displacement under compression.

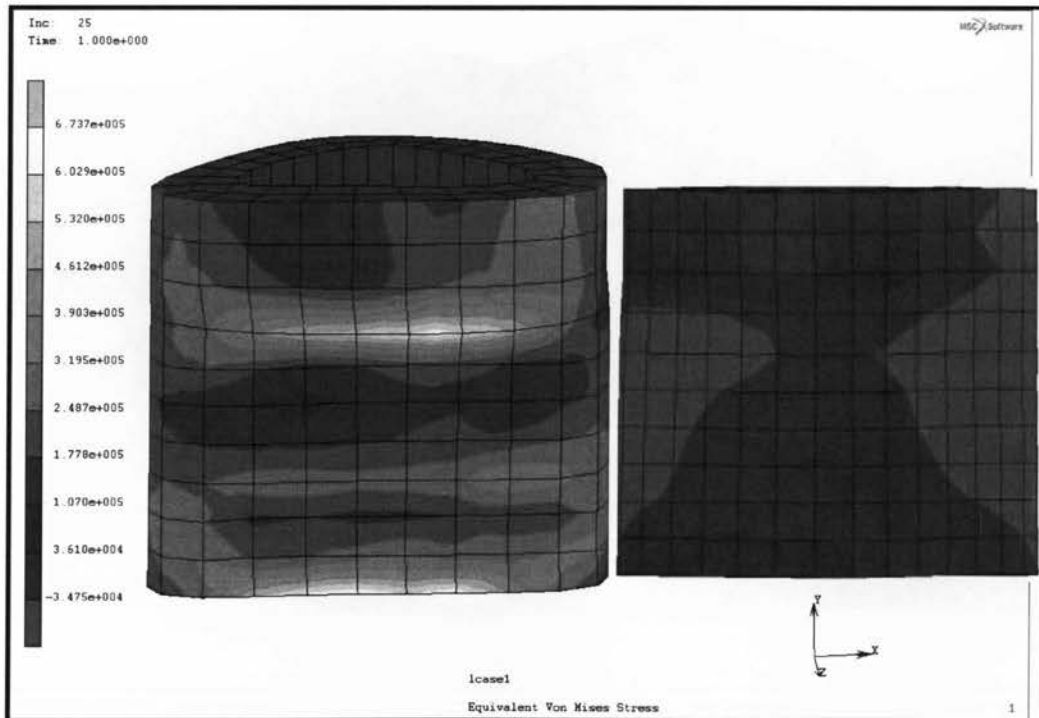


Figure B-22: CSF stress under compression.

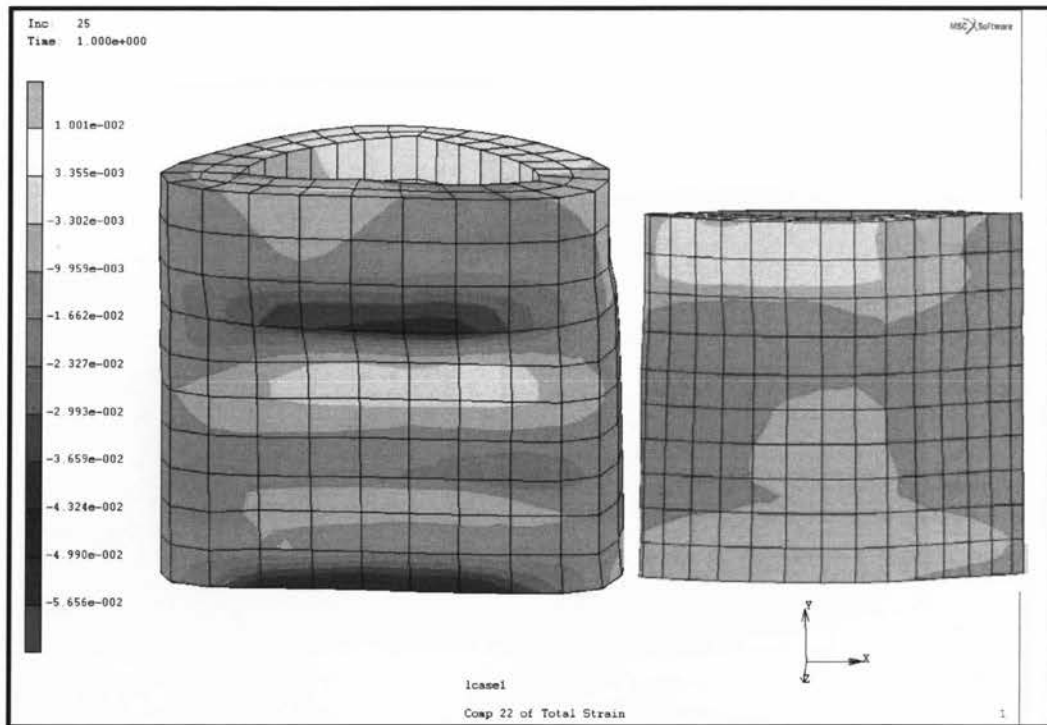


Figure B-23: CSF axial strain under compression.

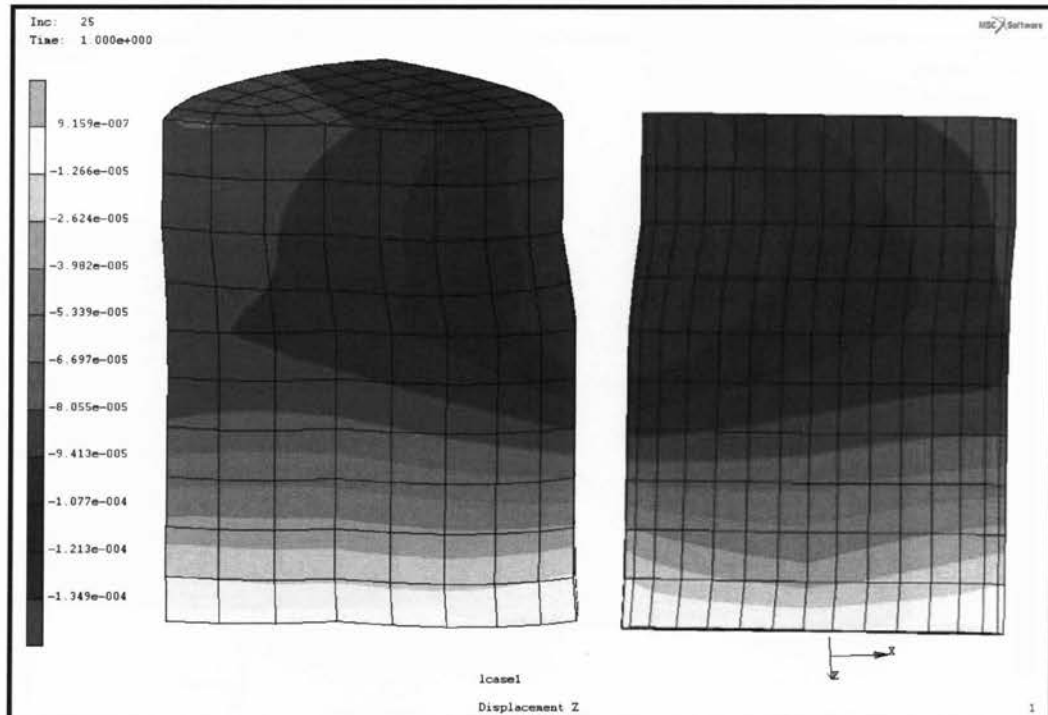


Figure B-24: Cord z displacement under compression.

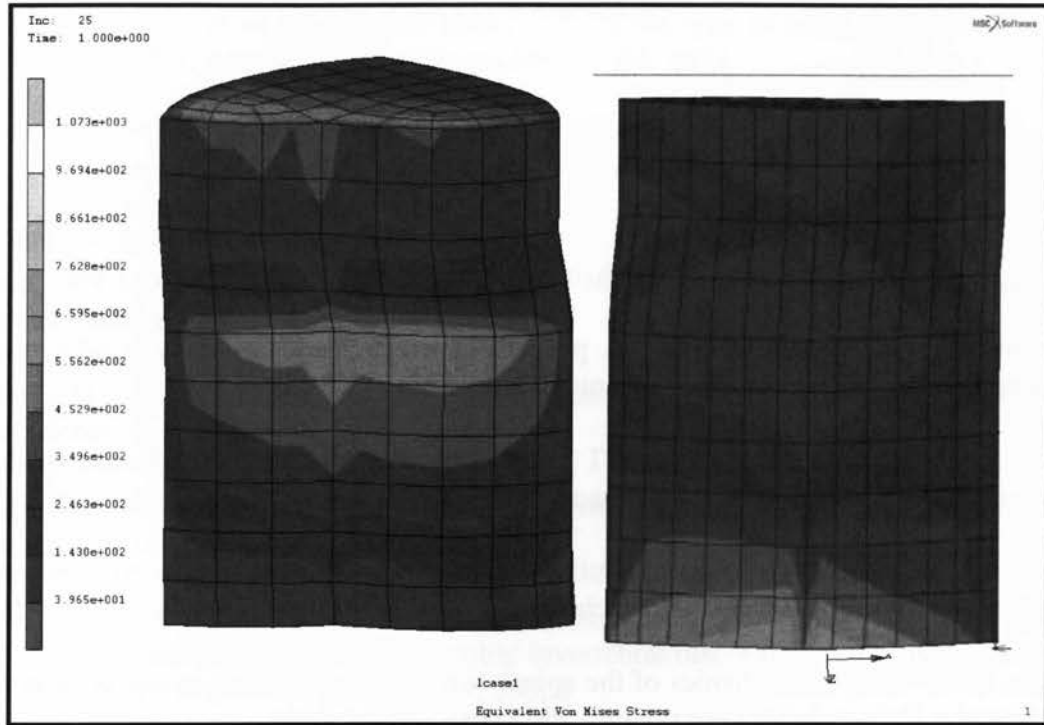


Figure B-25: Cord stress under compression.

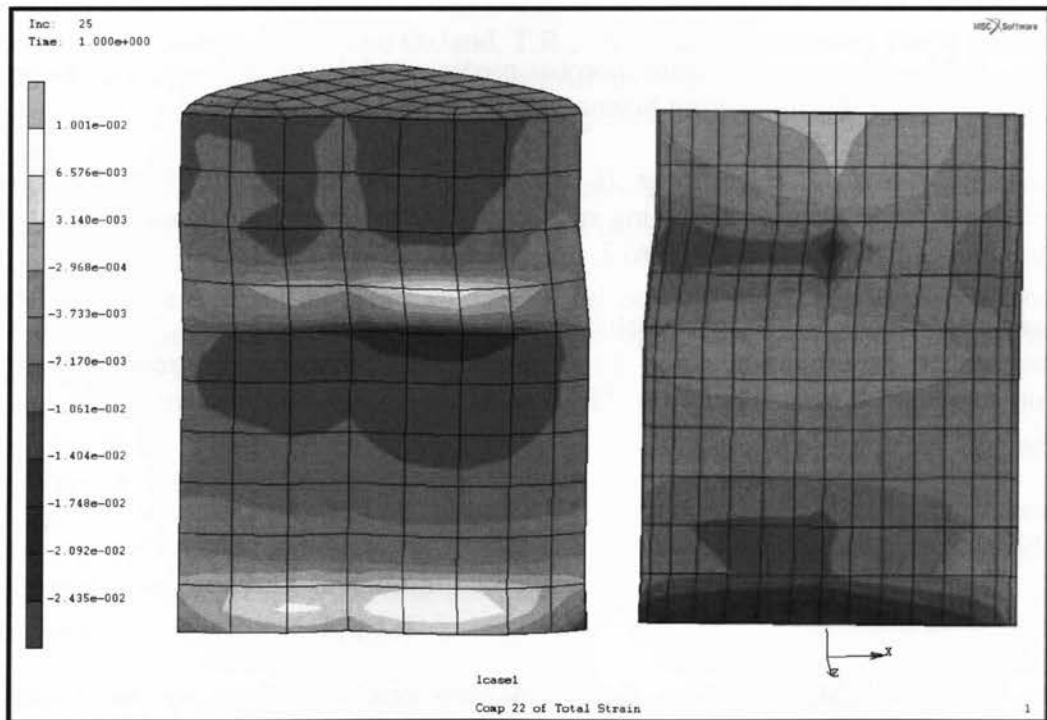


Figure B-26: Cord axial strain under compression.

References

- Afifi, A.K., and Bergman, R.A., "Functional neuroanatomy: text and atlas", 2nd edition, McGraw-Hill Professional, pp. 40-60, 2005
- Amstrong, C.G., Lai, W.M., and Mow, V.C., "An analysis of the unconfined compression of articular cartilage", *Journal Biomechanics Engineering* 106, pp.165-173, 1984
- Argoubi, M. and Shirazi-Adl, A., "A poroelastic creep response analysis of a motion segment on compression", *J. Biomechanics* 29, pp.1331-1339, 1996
- Basa, S., and Balasubramanian, v., "CT based three dimensional finite element model of cervical spine", *Biomedical and Pharmaceutical Engineering* 11, pp. 217-220, 2006
- Belytschko, T., Kulak, R.F., and Schutlz, A.B., "Finite Element Stress Analysis of an Intervertebral Disc", *Journal of Biomechanics* 7, pp. 277 – 285, 1974
- Bilston, L.E., "The biomechanics of the spinal cord during traumatic spinal cord injury", Philadelphia: University of Pennsylvania, PhD Dissertation, 1994
- Biot, M.A., "General theory of three-dimensional consolidation", *Journal of Applied Physics* 12, pp. 155-164, 1941
- Bowen, R.M., "Incomprehensible porous media models by use of the theory of mixtures", *Journal of Engineering Science* 18, pp.1129-1148, 1980
- Bozic, K. J., Keyak, J. H., Skinner, H. B., Bueff, H. U. and Bradford D. S., "Three – Dimensional finite element modeling of a cervical vertebra: An investigation of burst fracture mechanism", *J. Spine Disord.* 7, pp. 102-110, 1994
- Clausen, J., Goel, V. K., Traynelis V. C., and Wilder, D. G., "Cervical spine Biomechanical investigation using an experimentally validated FE model of C5-C6 motion segment", *Trans. 42nd Ann. Meeting, Orthop. Res. Soc., Atlanta , GA*, pp.657, 1996
- Clausen, J.D., Goel, V.K., Traynelis, V.C., and Scifert, J., "Unicinate Process and Luschka Joints Influence the Biomechanics of the Cervical Spine: Quantification Using a Finite Element Model of the C5-C6 Segment", *Journal of Orthopaedic Research* 15, pp.342 – 347, 1997
- Cohen, B., Lai, W.M., and Mow, V.C., " A transversely isotropic biphasic model for unconfined compression of growth plate and chondroepiphysis", *Journal of Biomechanics Engineering*, 1997

Dall, D. M. "Injuries of the cervical spine. I. Does the type of bony injury affect spinal cord recovery?" *S. Afr. Med. J.*46 (30), pp.1048–1056, 1972

Edgard, S.A., Spilker, R.L., "Finite element formulations for hyperelastic transversely isotropic biphasic soft tissues", *Computer Methods in Applied Mechanics and Engineering* 151(4), 1998

Drake, R.L., Vogl, W., and Mitchell A.W.M. "Gray's anatomy for students", Elsevier/Churchill Livingstone, c2005

Dutton, M., "Orthopaedic Examination, Evaluation, and Intervention", McGraw-Hill Professional, pp. 1037-1038, 2004

Fagan, M.J., Julian, S., and Mohsen., A.M., "Finite element analysis in spine research", *Proc Instn Mech Engrs* 216, pp. 281-298, 2002a

Fagan, M.J., Julian, S., Siddall, D.J., and Mohsen., A.M., "Patient-specific spine models. Part 1: finite element analysis of the lumbar intervertebral disc-a material sensitivity study", *Proc Instn Mech Engrs* 216, pp. 299-314, 2002b

Gilad, I., and Nissan, M., "A Study of Vertebra and Disc Geometric Relations of the Human Cervical and Lumbar Spine", *Spine* 11(2), pp.154 – 157, 1986

Greaves, C.Y., Gadala, M.S., and Oxland, T.R., "A Three-Dimensional Finite Element Model of the Cervical Spine with Spinal Cord: An Investigation of Three Injury Mechanisms", *Annals of Biomedical Engineering* 36(3), pp. 396–405, 2008.

Guerin H.A.L., "A nonlinear anisotropic continuum model of human Annulus Fibrosus mechanical behavior", PhD Thesis, Pennsylvania University, 2005

Ha, S.K., "Finite element modeling of multi-level cervical spinal segments (C3-C6) and biomechanical analysis of an elastomer-type prosthetic disc", *Medical Engineering & Physics* 28, pp.534-541, 2006

Holzappel, G.A., "Nonlinear Solid Mechanics - A Continuum Approach for Engineers", John Wiley & Sons, Chichester, 2000

Homles, M.H., Lai, W.M., Mow, V.C., "Singular perturbation analysis the nonlinear, flow dependent compressive stress relation behavior of articular cartilage", *Biomechanics Engineering* 107, pp. 206-218, 1985

Homles, M.H., "Finite deformation of soft tissue: Analysis of a mixture model in uniaxial compression", *Journal of Biomechanics Engineering* 108, pp.372-381, 1986

Homles, M.H., and Mow, V.C., "The non-linear characteristics of soft gels and hydrated connective tissues in ultrafiltration", *Journal of Biomechanics* 23, 1145-1156, 1990

Hosey, R. R., and Liu, Y. K., "A homeomorphic finite element model of the human head and neck", In *Finite Elements in Biomechanics*, pp. 379-401. Ed. R. H. Gallagher, 1982

Iatridis J.C, "Biomechanics of the Annulus Fibrosus and Nucleus Pulposus of the Human Lumbar Invertebral Disc and the Effects of Degeneration", PhD Thesis, Columbia University, 1996

Ishikawa, M., Matsumoto, M., Fujimura, Y., Chiba, K., and Toyama, Y., "Changes of cervical spinal cord and cervical spinal canal with age in asymptomatic subjects", *Spinal Cord* 41, pp. 159-163, 2003

Jost R, Nurick GN., "Development of a finite element model of the human neck subjected to high g-level deceleration", *Int. J. Crashworthiness* 5, pp. 259-267, 2000

Kleinberger, M., "Application of Finite Element Techniques to the Study of Cervical Spine Mechanics", *Proceedings from the 37th Stapp Car Crash Conference*, pp.261 – 272, 1993

Kulak, R.F., Belytschko, T.B., Schultz, A.B., and Galante, J.O., "Nonlinear Behavior of the Human intervertebral Disc under Axial Load", *Journal of Biomechanics* 9, pp.377 – 386, 1976

Kumaresan, S., Yoganandan, N., Pintar, F, Voo, L., Cusick, J., and Larson, S., "Finite element modeling of cervical laminectomy with graded facetectomy", *Spinal Disord* 10, pp. 40-70, 1997

Kumaresan S., Yoganandan, N., and Pintar, F.A., "Finite Element Modeling Approaches of Human Cervical Spine Facet Joint Capsule", *Journal of Biomechanics* 31, pp.371 – 376, 1998

Kumaresan, S., Yoganandan, N. and Pintar, F. A., "Finite element analysis of the cervical spine: a material property sensitivity analysis", *Clin. Biomechanics* 14, pp.41–53, 1999

Kumaresan, S., Yoganandan, N., Pintar, F. A., Maiman, D.J., and Goel, V.K., "Contribution of disc degeneration to osteophyte formation in the cervical spine: a biomechanical investigation", *J. Orthopaedic* 19, pp.977–984, 2001

Kurtz, S.M., and Edidin A.A., "Spine technology handbook", Academic Press, 2006

Lai, W.M., and Mow, V.C., "Drag-induced compression of articular cartilage during a permeation experiment", *Biorheol.* 17: pp. 111-123., 1980

- Laible, J.P., P#aster, D.S., Krag, M.H., Simon, B.R., Haugh, L.D., "A poroelastic-swelling finite element model with application to the intervertebral disc", *Spine* 18, pp. 659-670, 1993
- Lee, C.K., Kim, Y.E., Lee, C.S., Hong, Y.M., Jung, J.M., and Goel, V.K., "Impact response of the intervertebral disc in a finite element model", *Spine* 25(19), pp. 2431-2439, 2000
- Levenston, M.E., Frank, E.H., and Grodzinsky, A.J., "Variationally derived 3-field element formulations for quasistatic poroelastic analysis of hydrated biological tissues", *Comput. Methods Appl. Mech. Engrg.* 156, pp. 231-246, 1998
- Liu, Y., and G. Ray, "A Finite Element Analysis of Wave Propagation in the Human Spine", Technical Report F33615-72-C-1212. Wright Patterson A.F.B. Fairborn, OH, 1973
- Lodygowski, T., Kakol, W., and Wierszycki, M., "Three-dimensional nonlinear finite element model of the human lumbar spine segment", *Acta of Bioengineering and Biomechanics* 7(2), pp. 17-27, 2005
- Loret, B., and Simoes, F.M.F., "Articular cartilage with intra- and extrafibrillar waters: a chemo-mechanical model", *Mechanics of Materials* 36(6), 2004
- Malanga, A.G., Kim, D. "Cervical spine sprain/strain injuries", www.E-medicine.com, 2002
- Marchand, F., and Ahmed, A.M., "Investigation of the laminate structure of lumbar disc annulus fibrosus", *Spine* 15, pp. 402 – 410, 1990
- Maurel, N., Lavaste, F., Skalli, W., "A Three-Dimensional Parameterized Finite Element Model of the Lower Cervical Spine. Study of the Influence of the Posterior Articular Facets", *J. Biomech.*, 30, pp.921-931, 1997
- Meyer, P., Cybulski, G. and Rusin, J., "Spinal Cord Injury", *Neurol Clin* 9, pp. 625-661, 1991
- Moroney, S.P., Schultz, A.B., Miller, J.A.A., and Andersson, G.B.J., "Load-Displacement Properties of Lower Cervical Spine Motion Segments", *Journal of Biomechanics* 21(9), pp.769 – 779, 1988
- Mow, V.C., Kuei, S.C, Lai, W.M., and Armstrong, C.G., "Biphasic creep and stress relaxation of articular cartilage in compression: theory and experiments", *Journal of Biomechanics* 102, pp.73-83, 1980

Ng, H. W., and Teo, E. C., "Nonlinear finite-element analysis of the lower cervical spine (C4-C6) under axial loading", *Journal of spinal* 14(3), pp. 201-210, 2001

Ng, H.W., and Teo, E.C., "Probabilistic design analysis on the influence of material property on the human cervical spine", *J Spinal Disorders and Techniques* 17(2), pp. 123-133, 2004

Ng, H.W., and Teo, E.C., "The influence of preload amagnitude and orientation angles on the cervical biomechanics: A FE study", *J Spinal Disorders and Techniques* 18(1), pp. 72-79, 2005.

Ng, H.W., and Teo, E.C., Lee, K.K., and Qiu, T.X., "Finite element analysis of cervical spinal instability under physiological loading", *J Spinal Disorders and Techniques* 16(1), pp. 55-65, 2003

Ng, H.W., and Teo, E.C., and Lee, P.V.S., "Statistical factorial analysis on the material property sensitivity of the mechanical responses of the C4-C6 under compression, anterior and posterior shear", *J Biomechanics* 37(5), pp. 771-777, 2004

Ng, H.W., and Teo, E.C., and Zhang, Q.H., "Influence of cervical disc degeneration after posterior surgical techniques in combined flexion-extension – A Non-linear Study", *Transactions of ASME Biomechanical Engineering* 127(1), pp.186-192, 2005

Nightingale, R.W., Winkelstein, B.A., Knaub, K.E., Richardson, W.J., Luck, J.F., and Myers, B.S., "Comparative Strengths and Structural Properties of the Upper and Lower Cervical Spine in Flexion and Extension", *Journal of Biomechanics* 35, pp.725 – 732, 2002

Nightingale, R.W., Chancey, V.C., Ottaviano, D., Luck, J.F., Tran, L., Prange, M., and Myers, B.S., "Flexion and Extension Structural Properties and Strengths for Male Cervical Spine Segments", *Journal of Biomechanics* 40(3), pp. 535-542, 2007

Ogden, R. W., "Non-Linear Elastic Deformation", Dover Publication INC. Mineola, New York, 1984

Palomar, A.P.D., Calvo, B., and Doblare, M., "An accurate finite element model of the cervical spine under quasi-static loading", *J.Biomechanics* 41, pp. 523-531, 2008

Panjabi, M.M., Summers, D.J., Pelker, R.R., Videman, T., Friedlaender, G.E., and Southwick, W.O., "Three-Dimensional Load-Displacement Curves Due to Forces on the Cervical Spine", *Journal of Orthopaedic Research* 4, pp.152 – 161, 1986

Panjabi, M.M., Duranceau, J., Goel, V., Oxland, T., and Takata, K., "Cervical Human Vertebrae: Quantitative Three-Dimensional Anatomy of the Middle and Lower Regions", *Spine* 16(8), pp. 7 – 12. 1991a

Panjabi, M.M., Oxland, T.R., and Parks, E.H., "Quantitative Anatomy of Cervical Spine Ligaments Part I: Upper Cervical Spine", *Journal of Spinal Disorders* 4, 270 – 276, 1991b

Panjabi, M.M., Oxland, T., Takata, K., Goel, V., Duranceau, J., and Krag, M., "Articular Facets of the Human Spine: Quantitative Three-Dimensional Anatomy", *Spine* 18(10), pp. 1298 – 1310, 1993.

Panjabi, M.M., Crisco, J.J., Vasavada, A., Grob, D., Crisco, J., Dvorak, J., "On the understanding of clinical instability", *Spine* 19(23), pp.2642-2650, 1994

Panjabi, M.M., Chen, N.C., Shin, E.K., and Wang, J-L., "The Cortical Shell Architecture of Human Cervical Vertebral Bodies", *Spine* 26(22), pp. 2478 – 2484, 2001

Pooni, J.S., Hukins, D.W.L., Harris, P.F., Hilton, R.C., Davies, K.E., "Comparison of the structure of human intervertebral discs in the cervical, thoracic and lumbar regions of the spine", *Surgical and Radiologic Anatomy* 8, pp. 175–182, 1986

Prendergast, P.J, Driel, W.D., and Kuiper, J.H., "A comparison of finite element codes for the solution of biphasic proelastic problems", *Proc. Instn Mechanical Engineers* 210, 1996

Roberts, S., Menage, J., Urban, J.P.G., "Biochemical and structural properties of the cartilaginous endplate and its relation to the Invertebral disc", *Spine* 14, pp. 166 – 174, 1989

Scifert, J., Totoribe K., Goel, V., and Huntzinger, J., "Spinal cord mechanics during flexion and extension of the cervical spine : A finite element study", *Pain Physician* 5, pp. 394-400, 2002

Shea, M., Edwards, W.T., White, A.A., and Hayes, W.C., "Variations of stiffness and strength along the human cervical spine", *Journal of Biomechanics* 24(2), pp. 95-107, 1991

Shirazi-Adl, S. A., Shrivastava, S. C., and Ahmed, A. M., "Stress analysis of the lumbar disc-body unit in compression. A three-dimensional nonlinear finite element study", *Spine* 9, pp. 120 – 134, 1984

Shirazi-Adl, A., Ahmed, A. M. and Shrivastava, S. C., "A finite element study of a lumbar motion segment subjected to pure sagittal plane moments" *J. Biomechanics* 19, pp. 331–350, 1986

Shirazi-Adl, A., " On the fiber composite material models of disc annulus comparison of predicted stresses *J. Biomechanics* 22, pp. 357–365, 1989

Shirazi-Adl, A., "Finite element evaluation of contact loads on facets of an L2–L3 lumbar segment in complex loads", *Spine*16, pp.533–541, 1991

Shirazi-Adl, A. and Drouin, G., "Finite element simulation of changes in the fluid content of human lumbar discs: mechanical and clinical implications", *Spine* 17, pp.206–212, 1992

Shirazi-Adl, A., "Analysis of role of bone compliance on mechanics of a lumbar motion segment", *J. Biomech. Engng*16, pp.408–412, 1994

Simon, B.R., Wu, J.S.S., Carlton, M.W., Evans, J.H., and Kazarian, L.E., "Structural models for human spinal motion segments based on a poroelastic view of the intervertebral disk", *Journal of biomechanical engineering* 107, pp.327-335, 1985

Simon, B.R., "Multiphase poroelastic finite element models for soft tissue structures", *Applied Mechanics Reviews* 45, pp.191-218, 1992

Spencer, A. J.M., "Continuum Mechanics", Longman Scientific & technical, Longman group limited, UK, 1984

Spilker, R.L., Suh, J.K, and Mow, V.C.A., " A finite element formulation of the nonlinear biphasic model for articular cartilage and hydrated soft tissues including strain-dependent permeability ", In *Computational methods in bioengineering*, pp. 81-92, 1988

Spilker, R.L., Suh, J.K, "Formulation and evaluation of a finite element model for the biphasic model of hydrated soft tissues", *Computers and structures* 35(4), pp.425-439, 1990

Suh, J.K., Spilker, R.L., and Holmes, M.H., "A penalty finite element analysis for non-linear mechanics of biphasic hydrated soft tissue under large deformation", *Numerical Methods in Engineering* 32, pp. 1411-1439, 1991

Teo, E. C., and H. W. Ng, "Evaluation of the Role of Ligaments, Facets and Disc Nucleus in Lower Cervical Spine under Compression and Sagittal Moments Using Finite Element Method," *Med. Eng. Phys.* 23, pp.155–164, 2001

Teo, E. C., K. K. Lee, et al., "The Biomechanics of Lumbar Graded Facetectomy Under Anterior-shear Load," *IEEE Trans. Biomed. Eng.* 51:443–449, 2004

Teo, E. C., K. Yang, et al., "Effects of Cervical Cages on Load Distribution of Cancellous Core: A Finite Element Analysis," *J. Spinal Disord. Tech.* 17, pp.226–231, 2004

Truesdell, C., and Toupin, R.A., "The Classical field theories, handbuch der physik III/1", Springer, 1960

Wheeldon, J.A., Pintar, F.A., Knowles, S., Yoganandan, N., "Experimental flexion/extension data corridors for validation of finite element models of the young, normal cervical spine", *Journal of biomechanics* 39, pp. 375-380, 2006

Wheeldon, J.A., Stemper, B.D, Yoganandan, N., and Pintar, F.A., "Validation of a finite element model of the young normal lower cervical spine", *Biomechanical Engineering* 36, pp. 1458-1469, 2008

White, A.A., and Panjabi, M.M., "Clinical Biomechanics of the Spine". 2nd Edition, J.B. Lippincott Co., Philadelphia, 1990

Wilke, H. J., Neef, P., Caimi, M., Hoogland, T., and Claes, L. E., "New in vivo measurements of pressures in the intervertebral disc in daily life", *Spine* 24, pp. 755 – 762, 1999

Wu, J.S.S., and Chen, J.H., "Clarification of the mechanical behavior of spinal motion segments through a three-dimensional poroelastic mixed finite element model", *Med. Engineering physics* 18(3), pp. 215-224, 1996

Yoganandan, N., Kumaresan, S. C., Voo L., "Finite element applications in human cervical spine modeling", *Spine* 21 (15), pp.1824-1834, 1996a

Yoganandan, N., Kumaresan, S.C., Voo, L., Pintar, F. A., and Larson, S. J., "FE modeling of the C4-C6 cervical spine unit", *Med Eng Phys* 18(7), pp. 569-574, 1996b

Yoganandan, N., Kumaresan, S., and Pintar, F.A., "Geometric and mechanical properties of human cervical spine ligaments", *Biomechanical engineering* 122, pp. 623 – 629, 2000

Yu, Y. L., Boulay, G. H. D., Stevens, J. M., and Kendall, B. E., "measurements of the cervical spinal cord in computer-assisted myelography", *Springer-Vedag* 27, pp. 399-402, 1985

Yuan, Q., Dougherty, L., Margulies, S., "In Vivo Human Cervical Spinal Cord Deformation and Displacement in Flexion.", *Journal of Spine* (23), pp.1677-1683, 1998

Glossary of Acronyms

AF	Annulus Fibrosus
ALL	Anterior Longitudinal Ligament
CEP	Cartilage End Plate
CL	Capsular Ligaments
CSF	Cerebrospinal Fluid
CT	Computer Tomography
FE	Finite Element
FEA	Finite Element Analysis
FEM	Finite Element Method
ISL	Inter-Spinous Ligaments
IVD	Intervertebral Disc
LF	Ligamentum Flavum
MRI	Magnetic Resonance Imaging
NP	Nucleus Pulposus
PLL	Posterior Longitudinal Ligament
SPAMM	Spatial Modulation of Magnetization
SSL	Super-Spinous Ligaments
3D	Three-Dimensional

④
BL60-15